POLITECNICO DI MILANO

Facoltà di Ingegneria Industriale

Corso di Laurea Magistrale in Ingegneria Aeronautica

Investigation of the flow past an open three-dimensional cavity

Relatore: Prof. Franco AUTERI

Tesi di laurea di:
Matteo RIGHI
Matr. 783323

Anno Accademico 2012 - 2013

ad Elisa, mia costante

Il primo ringraziamento va al professor Franco Auteri, mio relatore in questo lavoro di Tesi. La sua disponibilità smisurata e la sua passione per quello che insegna mi hanno permesso di capire come poter affrontare i problemi che si possono incontrare in un lavoro come questo e di crescere dal punto di vista professionale. A lui tutta la mia stima.
Ringrazio anche Vincenzo Citro, i cui consigli nell'ultima parte del lavoro sono stati fondamentali sia per il calcolo che l'interpretazione dei risultati.
Un ringraziamento va ai miei compagni di tesi. Il grande supporto e l'amicizia che ci lega hanno reso davvero tutto più facile.
Infine, il più grande ringraziamento va a mia mamma: senza di te nulla sarebbe stato possibile.

Abstract

The aim of the present work is to describe the behaviour of an incompressible boundary layer flow over three-dimensional, open cavities with different aspect ratios. The principal interest of the work concerns the global stability analysis of the flow.

The numerical simulations are carried out with the open source solver NEK5000, which is based on a SEM method for the spatial discretization and on a BDFk-EXTk scheme for the time discretization. For the two-dimensional problems of the flow around a cylinder and the boundary layer flow over an open cavity, results are obtained in good agreement with those available in the literature for both the base flow and the eigensolution calculation.

A detailed analysis of the flow morphology for the cavity with three aspect ratios is provided and the present results are compared with experimental results available in literature. The calculation of the eigenvalues of the linearised Navier–Stokes problem is carried out for the flow in the cavity with aspect ratio one for $Re = 7000$. The results must be considered as preliminary and further work is necessary for their validation. However, the good agreement with the stability results for the two-dimensional open cavity and the three-dimensional lid-driven cavity allows to conclude that the computed modes are sound from a physical viewpoint.

Keywords: three-dimensional open cavity, linear stability, Görtler vortices, unsteady instability, NEK5000.

Sommario

In questa tesi viene decritto il comportamento di un flusso incomprimibile all'interno di una cavità tridimensionale caratterizzata da diversi allungamenti. L'interesse principale di questo lavoro riguarda l'analisi di stabilità globale.

Le simulazioni numeriche sono state eseguite mediante il solutore open source NEK5000, che si basa sul metodo agli elementi spettrali per la discretizzazione spaziale e sullo schema BDFk-EXTk per la discretizzazione temporale. Per i problemi bidimensionali del flusso attorno ad un cilindro e all'interno di una cavità aperta sono stati ottenuti risultati in buon accordo con quelli presenti in letteratura sia per il flusso base sia per il calcolo delle autosoluzioni.

È stata eseguita inoltre un'analisi dettagliata della morfologia del flusso in cavità con tre diversi allungamenti, ottenendo un buon accordo con i risultati sperimentali disponibili in letteratura. Gli autovalori sono stati calcolati per il flusso base in una cavità con allungamento unitario e per un numero di Reynolds pari a 7000. Questi ultimi risultati devono essere considerati preliminari e ulteriori analisi sono necessarie per la loro validazione. Tuttavia, il buon accordo con i risultati di stabilità riguardanti la cavità aperta bidimensionale e la cavità chiusa tridimensionale permette di concludere che i modi calcolati sono fisicamente plausibili.

Parole chiave: cavità aperta tridimensionale, stabilità lineare, vortici di Görtler, instabilità instazionaria, NEK5000.

Contents

Introduction

One of the most important aspects that influences the economic performances of the global airline industry is the fuel costs. The 2014 IATA fuel fact sheet highlights that the fuel bill of the global airline industry is forecast to total $214 billion in 2013, which is an increase of $4 billion over 2012 and is 5 times 2003's fuel bill ($44 billion). At the same time, the net industry profits show an increase in the two past years starting from the $7.4 billion in 2012 and arriving to the $12.7 billion expected in 2013. In order to maintain the positive trend registered from 2010 and forecast also for the 2014, the introduction of new technologies reducing the fuel consumption and, as a consequence, the fuel bill is necessary. An important contribution to the fuel cost could come from reduction of the aerodynamic drag, which is the most important responsible of the fuel consumption, since the 50% of the consumption is due to skin friction drag, compared to the 30% coming from

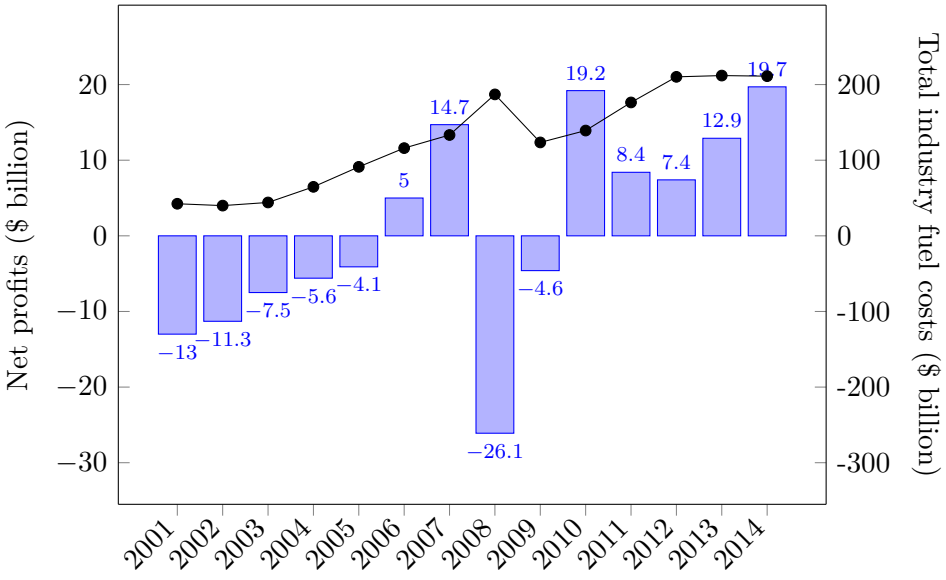

IATA: industry fuel costs (—●—) and net profits ( ).

lift-induced drag.

Therefore, the study of flow within and over an open cavity, which as all the large scale roughness elements promote instability and transition to turbulence with a consequent increase of drag, is very interesting because it represents a prototypical fluid dynamic problem. Examples of cavity flow can be the flow over a small hole in the surface of a wing or the flow over joints, bays, and so on. Investigating this kind of flows is extremely important since it can be a source of noise and of unsteady loads and vibrations and they can promote instability and transition to turbulence. If we consider just the aeronautical applications, it can be observed that several devices both in the external and internal aerodynamic surfaces of an aircraft, from the aerodynamic view point, behaves as cavity flows. For instance, we can cite the holes for screws and rivets, the cavity which is formed between the flaps and ailerons and the rest of the wing when these devices are activated, the wheel wells and holes for the pressure probes.

While the aeronautical applications often involve transonic Mach numbers, in this work we will assume the incompressibility of the flow. There are two main reasons that support this simplification. First, while the Mach number of the flow out of the cavity could be quite large, the Mach number within the cavity itself is by far lower, since the cavity flow is driven by the shear stress near to the wall and not directly by the external flow. Second, some of the phenomena that can be observed in cavity flows for quite high Mach numbers can be observed also for low Mach numbers, where the incompressible hypotheses is valid. Therefore, it is interesting to investigate this regime.

In this work, the attention is concentrated on a three-dimensional cavity of fixed square section and variable span. While the study of the cavity flow has been the subject of several investigations in the past, the literature is mainly concerned with closed cavities or two-dimensional flows. To the author's best knowledge, the stability of the flow in and over a three-dimensional cavity has never been investigated before by numerical techniques.

Cavity flow

The behaviour of a two-dimensional and compressible cavity flow is well described by Yamouni, Sipp and Jacquin [34] and Colonius [12] as the sum of two physical mechanisms which are responsible of the instability.

The first one, described by Rossiter [28], is the feedback aeroacoustic mechanism or flow acoustic resonance due to the small flow disturbances which arise before the cavity and that are amplified in the shear layer across the cavity mouth through the Kelvin-Helmholtz instability. These disturbances are convected downstream and the successive interaction with the trailing

edge of the cavity implies the formation of an irrotational and unsteady field, which can be seen as an acoustic wave system, that propagates upstream in the flow and that further excites the disturbances at the leading edge and in the shear layer. If these acoustic waves are able to increment the strength of the disturbances, and this is possible if the frequencies of the disturbances and the acoustic waves are integer multiples, then a resonance condition can occur at a determined frequency. So, this first mechanism can be seen as a feedback loop that causes the instability of the flow and it was denoted by Rowley, Colonius and Basu [29] as *shear-layer mode*. Several semi-empirical formulas can be found in the literature to calculate the resonance frequency which depends on parameters like the Mach number, the boundary layer momentum thickness and the dimensions of the cavity. In an incompressible regime the propagation speed of the acoustic waves tends to infinity and so the feedback to the leading edge is essentially instantaneous and purely hydrodynamic (it is sometimes termed "pseudosound mechanis"). In this regime some experiments realized confirm this instability mechanism. Chatellier, Laumonier and Gervais [9] observed at very low Mach number that the oscillations are driven by convective waves and they confirmed the presence of a feedback mechanism at the cavity mouth. More recently, Basely *et al.* [3] obtained the same results by a PIV measurements.

The second mechanism is the *wake mode*, identified for the first time by Gharib and Roshko [18] during some experiments in the incompressible regime for the axisimmetric cavity. As the length to depth ratio or the Reynolds number increase, they found that the oscillating flow over the cavity is more similar to the wake behind a bluff body, like a cylinder, than a free shear layer and that this mode is associated to an important increase in drag, due to the difference in pressure between the upstream and downstream walls of the cavity. Rowley, Colonius and Basu [29] observed that this mode is characterized by a large scale vortex that departs from the leading edge causing a flow separation. A second separation occurs at the cavity trailing edge where the vortex is ejected. During the evolution of this vortex a strong back-flow is present in the cavity and this is probabily the feedback mechanism that causes the instability of the flow, that is reached when the oscillation amplitude of the wake mode is such that the recirculating flow is sufficiently strong. The mode frequency is independent on the Mach number of the flow, therefore, this is a non-acoustic or hydrodynamic instability. Experiments for the rectangular cavity do not give good results about this mode because three-dimensional effects and turbulent boundary layer, which are often present in an experimental set-up, induce a decrease in the oscillation amplitude so that the instability condition is not reached. Further observations about this mode can be found in the works by Shieh and Morris [30] and Cain *et al.* [6].

Rowley, Colonius and Basu [29] showed that a transition between the shear-layer mode and the wake mode is possible and it can occur when the length of the cavity becomes large compared with the upstream boundary layer thickness, or when the Mach or Reynolds numbers are increased. This transition may be related to an absolute instability mechanism and, in particular, to the fact that the region of reverse flow in the wake mode is larger compared to that of the shear-layer mode.

These two physical mechanisms play a role in both the two-dimensional and the three-dimensional flow. In the 3D case, a third mechanism that depends on the strength of the recirculation flow near the cavity walls and that involves centrifugal forces has to be considered. Bres and Colonius [5] performed a stability analysis to three-dimensional perturbations of a two-dimensional flow field exploiting the Rayleigh discriminant criterion to provide a sufficient condition for the instability. Good agreement with these numerical results was obtained by Faure *et al.* [16] during some experiments about the development of the flow in a rectangular cuboid cavity for different Reynolds numbers and cavity shapes. Finally, Zhang and Naguib [35] studied experimentally the effects of the finite cavity width on the self-sustained oscillations in a low Mach number flow comparing the results obtained with an axisymmetric cavity. The experiments show that the walls cause a strong amplification of the pressure oscillations measured on the cavity floor at a distance of one depth from the side walls.

As in the cylinder case, the results of the stability analysis are exploited to perform passive or active control and suppression of the oscillations of the flow in the open cavity. An overview of the proposed methods can be found in the article by Cattafesta *et al.* [8].

Stability review

The dynamics of a cavity flow can be described by the Navier–Stokes equations and the behaviour of the system can be seen as a global oscillator characterized by a spatial distribution of fluctuating structures called global modes. Starting from the studies of Chomaz [10], a system with these characteristics can be analysed at local level determining an internal and self-sustained resonance condition at a precise frequency that arises when a region of absolute instability of sufficient size develops [19]. These local properties can be connected to the behaviour of the global system through the WKBJ approach, which is valid for slowly evolving flows and which allows to identify a specific position in the instability region that acts as a *wavemaker*, i.e. a region in the flow field where the physical mechanisms that cause the resonance and the instability of the system are localised. However, for the cavity problem studied in this work,

this theory does not give good results because the hypotheses of the WKBJ approach are not verified, in particular since there are important non-parallel effects.

Hence, to examine the stability characteristics of the flow in an open cavity a global approach based on the structural sensitivity analysis can be used, as proposed by Giannetti and Luchini [19] for the investigation of the flow past a two-dimensional circular cylinder. A similar analysis concerning the sensitivity to perturbations in the base flow was used by Marquet, Sipp and Jacquin [24] to perform a passive control of the cylinder wake by the introduction of a steady force acting on the base flow. Starting from a DNS (direct numerical simulation) this method employs a numerical modal analysis with a linearized theory. In particular, it consists of a linearization of the Navier–Stokes equations and the subsequent resolution of a generalized eigenvalue problem imposing homogeneous Dirichlet conditions on the domain boundary and a random perturbation superimposed to the steady flow as initial condition. The resulting spectra permits to understand if the flow is stable or not, while the eigenvectors corresponding to the most unstable eigenvalues are useful to localize the regions responsible of the instability.

An important tool necessary for the aforementioned analysis is the adjoint eigenvalue problem. In fact, the structural sensitivity analysis requires both the least stable eigenfunctions of the direct Navier–Stokes operator, which describe the flow oscillations, and the eigenfunctions of the adjoint operator. In fact, Chomaz [10] asserts that the *wavemaker* can be identified as the overlapping area between the direct and the adjoint eigenvectors and this is confirmed by the results published by Giannetti and Luchini [19].

Aim of the study and work structure

The principal objective of this work of thesis is to understand the behaviour of the flow over an open, three-dimensional cavity, and, in particular, to investigate the principal stability characteristics, examining the shape of the unstable global modes.

The work is structured as follow:

- The first chapter introduces the principal tools applied for the stability analysis. The theoretical constructs of structural sensitivity and receptivity, which are the basis of the global stability analysis, are illustrated in detail;

- The second chapter briefly describes NEK5000, the open source solver utilised for the computation of the base flow and the eigensolutions of the system. In particular, both the spatial and the temporal discretization

strategies will be explained as well for the eigenvalues computation. In the last part of this chapter the validation of the code is done by the comparison of the results about the two-dimensional cylinder and the two-dimensional open cavity with those present in the papers by Giannetti and Luchini [19] and by Sipp and Lebedev [32];

- The third chapter delineates the morphology of the flow over the cavity with aspect ratios $AR = 2$ and $AR = 3$. After a short description of the mesh, of the boundary and initial conditions and of the incoming boundary layer, the principal vortical structures that characterize the flow are introduced. The final section of this chapter is dedicated to the explanation of the principal properties of the flow in unsteady conditions;

- The last chapter presents the stability results obtained for the cavity with $AR = 1$ for $Re = 7000$. In particular, since the absence of references about eigensolutions relative to three-dimensional cavity in literature, the obtained results are compared with those about to the two-dimensional open cavity an the lid-driven cavity, confirming that the spectrum and the eigenvectors computed have a physical sense.

1 | Mathematical model

The motion of a viscous newtonian fluid in an open cavity can be represented by the velocity and pressure fields $\mathbf{b} = (\mathbf{u}, p)$, whose behaviours are described by the three-dimensional, unsteady, incompressible Navier–Stokes equations [26]:

$$\begin{cases} \dfrac{\partial \mathbf{u}}{\partial t} + (\mathbf{u} \cdot \nabla)\mathbf{u} - \dfrac{1}{Re}\nabla^2 \mathbf{u} + \nabla p = \mathbf{0} \\ \nabla \cdot \mathbf{u} = 0, \end{cases} \tag{1.1}$$

which can be written in compact form

$$\frac{\partial \mathbf{b}}{\partial t} = \mathbf{F}(\mathbf{b}). \tag{1.2}$$

In these equations Re denotes the Reynolds number, $\mathbf{u}$ denotes the velocity field, whose components are u in the stream-wise x direction, v in the cross-stream y direction and w in the wall-normal z direction and p denotes the reduced pressure. The Reynolds number is defined as:

$$Re = \frac{L\, U_\infty}{\nu} \tag{1.3}$$

where L is the reference length corresponding to the dimension of cavity in x direction, U_∞ is the modulus of the free-stream velocity and ν is the kinematic viscosity of the flow. In order to find a solution to the equations, it is necessary to introduce appropriate initial and boundary conditions. On the surface of the cavity, a no-slip and no-penetration condition is imposed

$$\mathbf{u} = 0 \quad \text{on } \Gamma_c \quad \forall t, \tag{1.4}$$

while on the inflow boundary and as initial condition, the Blasius boundary layer velocity distribution is assigned. The Blasius profile is the two-dimensional solution of the Prandtl boundary layer equations over a semi-infinite plate for a uniform free-stream velocity. Finally, to remove the

indeterminacy of the of the pressure field , a value for p has to be imposed in one point of the domain.

For the non-linear system (1.2), different equilibrium solutions may exist whose stability properties have to be investigated separately. In this thesis, after a linearization of the Navier–Stokes equations, the Lyapounov indirect method will be applied for which it will be necessary to calculate the eigenvalue of the system in the equilibrium point.

1.1 Linearization of Navier–Stokes equations

To investigate the linear stability properties of a steady solution, the Navier–Stokes equations must be linearized. Assuming the existence of a steady solution $\mathbf{B} = (\mathbf{U}, P)$ of the system, called base flow, such that $\mathbf{F}(\mathbf{B}) = \mathbf{0}$, the generic solution of the Navier–Stokes equations can be expressed as the sum of a steady part given by the base flow and a small unsteady perturbation as

$$\mathbf{u}(x, y, z, t) \to \mathbf{U}(x, y, z) + \mathbf{u}(x, y, z, t), \tag{1.5a}$$

$$p(x, y, z, t) \to P(x, y, z) + p(x, y, z, t), \tag{1.5b}$$

where $\mathbf{u}$ and p, in these formulae, represent the unsteady perturbation fields. Now, substituting the generic solution $\mathbf{b}(x, y, z, t) \to \mathbf{B}(x, y, z) + \mathbf{b}(x, y, z, t)$, given by the (1.5), in the Navier–Stokes equations (1.1) and neglecting all the quadratic terms, the following linearized system is obtained

$$\begin{cases} \dfrac{\partial \mathbf{u}}{\partial t} + (\mathbf{U} \cdot \nabla)\mathbf{u} + (\mathbf{u} \cdot \nabla)\mathbf{U} - \dfrac{1}{Re}\nabla^2 \mathbf{u} + \nabla p = \mathbf{0} \\ \nabla \cdot \mathbf{u} = 0, \end{cases} \tag{1.6}$$

which describes the evolution of the perturbed flow field $\mathbf{b}(x, y, z, t)$.

To complete this system the appropriate initial and boundary conditions are introduced

$$\mathbf{u}(\mathbf{r}, 0) = \mathbf{u}_0(\mathbf{r}) \qquad \text{for } t = 0 \tag{1.7a}$$

$$\mathbf{u}(\mathbf{r}, t) = \mathbf{u}_w(\mathbf{s}, t) \qquad \text{on } \Gamma_c \quad \forall t \tag{1.7b}$$

$$\mathbf{b}(\mathbf{r}, t) \to \mathbf{0} \qquad \text{as } \mathbf{r} \to \infty \quad \forall t, \tag{1.7c}$$

where $\mathbf{r}$ and $\mathbf{s}$ are two generic vectors which represent the position inside the domain and along the border, while $\mathbf{u}_0$ is the initial condition and $\mathbf{u}_w$ is the value of the velocity perturbation on the cavity surface Γ_c. The condition (1.7c), which asserts that the perturbation field has to vanish as $\mathbf{r} \to \infty$, is strictly related to the fact that the initial condition $\mathbf{u}_0$ has a compact support.

As in eq. (1.1), the indeterminacy of the perturbed pressure field can be eliminated specifying the value of the the pressure in a generic point of the domain.

The linearized Navier–Stokes equations (1.6) (LNSE in the following) can be rewritten in an equivalent but more compact form as

$$\begin{cases} \dfrac{\partial \mathbf{u}}{\partial t} + \mathscr{L}(\mathbf{U}, Re)\mathbf{u} + \nabla p = \mathbf{f}(\mathbf{r}, t) \\ \nabla \cdot \mathbf{u} = Q(\mathbf{r}, t), \end{cases} \tag{1.8}$$

where $\mathscr{L}(\mathbf{U}, Re)$ represents the linearized Navier–Stokes operator

$$\mathscr{L}(\mathbf{U}, Re) = (\mathbf{U} \cdot \nabla)\dots + (\dots \cdot \nabla)\mathbf{U} - \frac{1}{Re}\nabla^2 \dots . \tag{1.9}$$

Finally, in the right-hand side of the LNSE (1.8), two new terms are introduced and, in particular, $\mathbf{f}(\mathbf{r}, t)$ represents the effects of an external force and $Q(\mathbf{r}, t)$ takes into account a possible volume source in the flow field. Like the initial condition, both $\mathbf{f}$ and Q have a compact support in accordance with the far-field radiation condition (1.7c).

1.2 Adjoint Navier–Stokes equations

A useful tool in the analysis of the stability of a flow is the adjoint operator [23]. For instance the eigenmode of the adjoint operator are useful to locate the wavemaker region of the flow by investigating the structural sensitivity and to study the receptivity of the system. The adjoint operator is, in fact, an operator whose eigenfunctions are orthogonal to all but one eigenfunctions of the direct operator and it plays an important role in many applications, like optimization and control. It can be defined as follow:

Definition 1 (Adjoint operator) *Consider the linear operator $\mathscr{M}$ such that $\mathscr{M} : D(\mathscr{M}) \subseteq X \to Y$, where X and Y are Hilbert spaces and $D(\mathscr{M})$ is the operator domain. A necessary and sufficient condition for the existence of the adjoint operator $\mathscr{M}^+$ of $\mathscr{M}$ is that the closure of $D(\mathscr{M})$ is coincident with X. It can be defined in this way: $\boldsymbol{v} \in X$ is in the domain $D(\mathscr{M})$ of $\mathscr{M}$ if and only if there exists $\boldsymbol{v}^+ \in X$ such that, for all $\boldsymbol{u} \in D(\mathscr{M})$, $(\mathscr{M}\,\boldsymbol{u}, \boldsymbol{v}) = (\boldsymbol{u}, \boldsymbol{v}^+)$, where $(\boldsymbol{u}, \boldsymbol{v})$ denotes the L^2 inner product between $\boldsymbol{u}$ and $\boldsymbol{v}$. Then $\mathscr{M}^+\boldsymbol{v} = \boldsymbol{v}^+$ and so:*

$$(\mathscr{M}\,\boldsymbol{u}, \boldsymbol{v}) = (\boldsymbol{u}, \mathscr{M}^+\boldsymbol{v}). \tag{1.10}$$

In the case of a finite-dimensional linear operator, that can be described as a matrix, the adjoint operator is the Hermitian matrix (conjugated and transposed matrix). For more information about the adjoint operator and its applications one can refer to [14]. A simple and useful example to understand the procedure to get the adjoint operator is the following. Let us consider the second order linear and differential operator

$$\mathscr{M} = f\frac{d^2\ldots}{dx^2} + g\frac{d\ldots}{dx} + h\ldots \tag{1.11}$$

defined for $x \in (a, b)$, where f, g and h are constant coefficients. Applying the operator to a function $u \in \mathcal{H}^1$ and employing the $L^2(a, b)$ inner product with another continuous function v, it results:

$$\begin{aligned}(\mathscr{M}u, v) = \int_a^b v\,\mathscr{M}u\,dx = \int_a^b \left(v\,f\,\frac{d^2u}{dlx^2} + v\,g\,\frac{du}{dx} + v\,h\,u\right)dx = \\ = \left[f\,v\,\frac{du}{dx} - f\,u\,\frac{dv}{dx} + g\,u\,v\right]_a^b + \int_a^b \left(f\,\frac{d^2v}{dx^2} - g\,\frac{dv}{dx} + h\,v\right)u\,dx.\end{aligned} \tag{1.12}$$

In the right-hand side the term in the square brackets is called bilinear concomitant, while the integral contains the adjoint operator applied to the function v, that is

$$\mathscr{M}^+ = \frac{d^2(f\ \ldots)}{dx^2} - \frac{d(g\ \ldots)}{dx} + h\ \ldots. \tag{1.13}$$

Since the construction of $\mathscr{M}^+$ starting from $\mathscr{M}$ is based on (1.10), the bilinear concomitant evaluated on the endpoints of the domain must vanish. This represent a compatibility condition that relates the boundary conditions of the direct and the adjoint problem in order to define the adjoint operator of the system.

In the case of the linearized Navier–Stokes equations, the adjoint operator is defined starting from the generalized Lagrange identities, described for example by Ince [21], which are obtained applying differential identities to the product of functions and operators. An example can be given considering the ∇ operator and the functions $\mathbf{v}$ (vector) and q (scalar):

$$\nabla \cdot (q\mathbf{v}) = q\nabla \cdot \mathbf{v} + \mathbf{v} \cdot \nabla q. \tag{1.14}$$

In order to apply the generalized Lagrange identities, the first of the Navier–Stokes equations in homogeneous form (1.6) is multiplied by a vector field $\mathbf{v}$, while the second equation by a scalar field q, that form the generic field $\mathbf{c} = (\mathbf{v}, q)$. The mathematical steps necessary to treat each term are reported hereafter.

- Unsteady term

$$\mathbf{v} \cdot \frac{\partial \mathbf{u}}{\partial t} = \frac{\partial (\mathbf{v} \cdot \mathbf{u})}{\partial t} - \mathbf{u} \cdot \frac{\partial \mathbf{v}}{\partial t} \tag{1.15}$$

- First advection term

$$\begin{aligned} \mathbf{v} \cdot [(\mathbf{U} \cdot \nabla)\mathbf{u}] &= v_r U_s \frac{\partial u_r}{\partial x_s} = \\ &= \frac{\partial (v_r U_s u_r)}{\partial x_s} - u_r v_r \frac{\partial U_s}{\partial x_s} - u_r U_s \frac{\partial v_r}{\partial x_s} = \\ &= \nabla \cdot [\mathbf{U}(\mathbf{u} \cdot \mathbf{v})] - \mathbf{u} \cdot [(\mathbf{U} \cdot \nabla)\mathbf{v}] \end{aligned} \tag{1.16}$$

- Second advection term

$$\begin{aligned} \mathbf{v} \cdot [(\mathbf{u} \cdot \nabla)\mathbf{U}] &= v_r u_s \frac{\partial U_r}{\partial x_s} = \\ &= u_s \frac{\partial U_r}{\partial x_s} v_r = \mathbf{u} \cdot [(\nabla \mathbf{U}) \cdot \mathbf{v}] \end{aligned} \tag{1.17}$$

- Viscous term

$$\begin{aligned} \mathbf{v} \cdot \nabla^2 \mathbf{u} &= v_r \frac{\partial^2 u_r}{\partial x_s \partial x_s} = v_r \frac{\partial}{\partial x_s}\left(\frac{\partial u_r}{\partial x_s}\right) = \\ &= \frac{\partial}{\partial x_s}\left(v_r \frac{\partial u_r}{\partial x_s}\right) - \frac{\partial u_r}{\partial x_s}\frac{\partial v_r}{\partial x_s} = \\ &= \frac{\partial}{\partial x_s}\left(v_r \frac{\partial u_r}{\partial x_s}\right) - \frac{\partial}{\partial x_s}\left(u_r \frac{\partial v_r}{\partial x_s}\right) + u_r \frac{\partial^2 v_r}{\partial x_s \partial x_s} = \\ &= \nabla \cdot [(\nabla \mathbf{u}) \cdot \mathbf{v}] - \nabla \cdot [(\nabla \mathbf{v}) \cdot \mathbf{u}] + \mathbf{u} \cdot \nabla^2 \mathbf{v} \end{aligned} \tag{1.18}$$

- Pressure term

$$\mathbf{v} \cdot \nabla p = \nabla \cdot (p\mathbf{v}) - p \nabla \cdot \mathbf{v} \tag{1.19}$$

- Incompressibility term

$$q \nabla \cdot \mathbf{u} = \nabla \cdot (q\mathbf{u}) - \mathbf{u} \cdot \nabla q \tag{1.20}$$

Assembling all these terms, the following identity is obtained:

$$\begin{aligned}
&\mathbf{v}\cdot\left[\frac{\partial\mathbf{u}}{\partial t}+(\mathbf{U}\cdot\nabla)\mathbf{u}+(\mathbf{u}\cdot\nabla)\mathbf{U}-\frac{1}{Re}\nabla^2\mathbf{u}+\nabla p\right]+q\nabla\cdot\mathbf{u}+\\
&+\mathbf{u}\cdot\left[\frac{\partial\mathbf{v}}{\partial t}+(\mathbf{U}\cdot\nabla)\mathbf{v}-(\nabla\mathbf{U})\cdot\mathbf{v}+\frac{1}{Re}\nabla^2\mathbf{v}+\nabla q\right]+p\nabla\cdot\mathbf{v}= \qquad (1.21)\\
&=\frac{\partial(\mathbf{u}\cdot\mathbf{v})}{\partial t}+\nabla\cdot\left[\mathbf{U}(\mathbf{u}\cdot\mathbf{v})+\frac{1}{Re}(\nabla\mathbf{v})\cdot\mathbf{u}-\frac{1}{Re}(\nabla\mathbf{u})\cdot\mathbf{v}+p\mathbf{v}+q\mathbf{u}\right].
\end{aligned}$$

In order to compute the $L^2(\Omega)$ product and to apply the adjoint definition (1.10), this identity is integrated over the domain $\mathbb{R}\times\Omega$, where $\mathbb{R}$ is the domain for the time variable t, while Ω is the domain for the position vector $\mathbf{r}$. Exploiting integration by parts and the divergence theorem, thanks to the imposed boundary conditions and supposing that the perturbation field decays for $t\to\pm\infty$, the right-hand side of the equations (1.21), which corresponds to the bilinear concomitant, is null, while the left-hand side becomes

$$\begin{aligned}
&\int_{\mathbb{R}\times\Omega}\left\{\mathbf{v}\cdot\left[\frac{\partial u}{\partial t}+(\mathbf{U}\cdot\nabla)\mathbf{u}+\mathbf{u}\cdot\nabla)\mathbf{U}\right]+\frac{1}{Re}\nabla\mathbf{v}\cdot\nabla\mathbf{u}+\right.\\
&\qquad\left.-p\,\nabla\cdot\mathbf{v}+q\,\nabla\cdot\mathbf{u}\right\}+\\
&+\int_{\mathbb{R}\times\Omega}\left\{\mathbf{u}\cdot\left[\frac{\partial v}{\partial t}+(\mathbf{U}\cdot\nabla)\mathbf{v}-(\nabla\mathbf{U})\cdot\mathbf{v}\right]-\frac{1}{Re}\nabla\mathbf{u}\cdot\nabla\mathbf{v}+\right. \qquad (1.22)\\
&\qquad\left.-q\,\nabla\cdot\mathbf{u}+p\,\nabla\cdot\mathbf{v}\right\}=0.
\end{aligned}$$

The first integral can be seen as the weak formulation of the LNSE, and, consequently, the second integral is the weak formulation of the adjoint equations from which it is possible to extract the strong formulation of the adjoint Navier–Stokes equations

$$\begin{cases}\dfrac{\partial\mathbf{v}}{\partial t}+(\mathbf{U}\cdot\nabla)\mathbf{v}-(\nabla\mathbf{U})\cdot\mathbf{v}+\dfrac{1}{Re}\nabla^2\mathbf{v}+\nabla q=\mathbf{0}\\ \nabla\cdot\mathbf{v}=0,\end{cases} \qquad (1.23)$$

and the adjoint of the linearized Navier–Stokes operator, which reads

$$\mathscr{L}^{+}(\mathbf{U},Re)=(\mathbf{U}\cdot\nabla)\ldots-(\nabla\mathbf{U})\cdot\ldots+\frac{1}{Re}\nabla^2\ldots. \qquad (1.24)$$

Also for the solution of the adjoint problem it is necessary to introduce the appropriate boundary conditions, which are very similar to the ones of the direct problem. They can be expressed as

$$\mathbf{v}(\mathbf{r},t) = \mathbf{0} \quad \text{on } \Gamma_c \quad \forall t \tag{1.25a}$$
$$\mathbf{c}(\mathbf{r},t) \to \mathbf{0} \quad \text{as } \mathbf{r} \to \infty \quad \forall t. \tag{1.25b}$$

where the first one is a homogeneous condition imposed on the cavity surface, while the second one implies that the adjoint field has to vanish for $\mathbf{r} \to \infty$.

1.3 Structural sensitivity

The first step necessary to investigate the stability of a base flow is the global linear stability analysis. This analysis starts writing the perturbations in the form of global modes as

$$\mathbf{u}(\mathbf{r},t) = \hat{\mathbf{u}}(\mathbf{r})\exp(\sigma t) \tag{1.26a}$$
$$p(\mathbf{r},t) = \hat{p}(\mathbf{r})\exp(\sigma t), \tag{1.26b}$$

where σ is the complex eigenvalue associated with the complex eigenfunction $\hat{\mathbf{b}} = (\hat{\mathbf{u}}, \hat{p})$. Now, substituting $\hat{\mathbf{u}}$ and $\hat{p}$ in the LNSE (1.8), the direct eigenvalue problem is obtained

$$\begin{cases} \sigma\hat{\mathbf{u}} + (\mathbf{U}\cdot\nabla)\hat{\mathbf{u}} + (\hat{\mathbf{u}}\cdot\nabla)\mathbf{U} - \dfrac{1}{Re}\nabla^2\hat{\mathbf{u}} + \nabla\hat{p} = \mathbf{0} \\ \nabla\cdot\hat{\mathbf{u}} = 0, \end{cases} \tag{1.27}$$

and, for its resolution, the following boundary conditions are imposed

$$\hat{\mathbf{u}}(\mathbf{r},t) = \mathbf{0} \quad \text{on } \Gamma_c \tag{1.28a}$$
$$\hat{\mathbf{b}}(\mathbf{r},t) \to \mathbf{0} \quad \text{as } \mathbf{r} \to \infty. \tag{1.28b}$$

The non-trivial solutions of this problem are the sets of direct global modes and, associated to each mode, the eigenvalue $\sigma = \lambda + i\omega$ gives information about the growth rate with its real part λ and about the oscillation frequency with its imaginary part ω. Since the problem is linearized, the stability of the system can be studied looking at the real part of the eigenvalue: if $\mathrm{Re}(\sigma) < 0$, the associated mode is stable, while if $\mathrm{Re}(\sigma) > 0$ the mode is unstable. In this last case the mode grows with an exponential trend until the non linear effects become important.

So, first of all, it is necessary to calculate the eigenvalue with the largest real part, termed σ_1, because it is the most unstable if $\mathrm{Re}(\sigma_1) > 0$ or the

least stable if $\mathrm{Re}(\sigma_1) < 0$, and, therefore, this is the eigenvalue which controls the behaviour of the system. At this point, it is interesting to analyse how the eigenvalue σ_1 is sensitive to a perturbation

$$\sigma_1 \to \sigma_1 + \sigma_1', \tag{1.29}$$

where σ_1' denotes the perturbation of the eigenvalue. By investigating the sensitivity of the least stable eigenvalue to a localized feedback will highlight the region of the flow where the instability mechanisms of the system acts.

The introduction of a disturbance in the flow field causes modification of the generic direct eigensolution

$$\sigma \to \sigma + \sigma', \tag{1.30a}$$
$$\hat{\mathbf{u}} \to \hat{\mathbf{u}} + \hat{\mathbf{u}}', \tag{1.30b}$$
$$\hat{p} \to \hat{p} + \hat{p}', \tag{1.30c}$$

where the perturbations are second order terms. Substituting the (1.30) in the direct eigenvalue problem (1.27) and neglecting the quadratic terms, this equation for σ' is obtained

$$\begin{cases} \sigma\hat{\mathbf{u}}' + \mathscr{L}(\mathbf{U}, Re)\hat{\mathbf{u}}' + \nabla\hat{p}' = -\sigma'\hat{\mathbf{u}} - \mathscr{L}'(\mathbf{U}')\hat{\mathbf{u}} \\ \nabla \cdot \hat{\mathbf{u}}' = 0, \end{cases} \tag{1.31}$$

where $\mathscr{L}$ is the linearized Navier–Stokes operator (1.9), while $\mathscr{L}'$ is the perturbed Navier–Stokes operator defined as

$$\mathscr{L}'(\mathbf{U}') = (\mathbf{U}' \cdot \nabla) \ldots + (\ldots \cdot \nabla)\mathbf{U}'. \tag{1.32}$$

In order to calculate the perturbation σ' of the eigenvalue it is necessary to introduce the adjoint eigenvalue problem, whose generic solution, called global adjoint mode, can be expressed as

$$\mathbf{v}(\mathbf{r}, t) = \hat{\mathbf{v}}(\mathbf{r}) \exp(-\sigma t) \tag{1.33a}$$
$$q(\mathbf{r}, t) = \hat{q}(\mathbf{r}) \exp(-\sigma t), \tag{1.33b}$$

where σ is the same eigenvalue of the corresponding direct global mode. The adjoint eigenvalue problem is obtained introducing the (1.33) in the adjoint Navier–Stokes equations (1.23) and can be written in this form

$$\begin{cases} -\sigma\hat{\mathbf{v}} + \mathscr{L}^+(\mathbf{U}, Re)\hat{\mathbf{v}} + \nabla\hat{q} = \mathbf{0} \\ \nabla \cdot \hat{\mathbf{v}} = 0. \end{cases} \tag{1.34}$$

Now, the generalized Lagrange identities are applied to the direct eigenvalue problem obtaining an equation very similar to (1.21), where $\mathbf{u}$ and p are replaced with the direct eigenfunctions $\hat{\mathbf{u}}$ and $\hat{p}$, while $\mathbf{v}$ and q are replaced by the adjoint eigenfunctions $\hat{\mathbf{v}}$ and $\hat{q}$

$$\begin{aligned}
&\hat{\mathbf{v}}^*\cdot\left[\sigma\hat{\mathbf{u}}+\mathscr{L}(\mathbf{U},Re)\hat{\mathbf{u}}+\nabla\hat{p}\right]+\hat{q}^*\nabla\cdot\hat{\mathbf{u}}+\\
&+\hat{\mathbf{u}}\cdot\left[-\sigma\hat{\mathbf{v}}^*+\mathscr{L}^+(\mathbf{U},Re)\hat{\mathbf{v}}^*+\nabla\hat{q}^*\right]+\hat{p}\nabla\cdot\hat{\mathbf{v}}^*= \\
&=\nabla\cdot\left[\mathbf{U}(\hat{\mathbf{u}}\cdot\hat{\mathbf{v}}^*)+\frac{1}{Re}(\nabla\hat{\mathbf{v}}^*)\cdot\hat{\mathbf{u}}-\frac{1}{Re}(\nabla\hat{\mathbf{u}})\cdot\hat{\mathbf{v}}^*+\hat{p}\hat{\mathbf{v}}^*+\hat{q}^*\hat{\mathbf{u}}\right].
\end{aligned} \tag{1.35}$$

In order to compute the $L^2(\Omega)$ inner product, in the previous equation the adjoint eigenfunctions are introduced as their complex conjugate according to the definition of the $L^2(\Omega)$ inner product because, in general, they are complex functions. The integration over the domain Ω leads to this new equation

$$\begin{aligned}
&\int_\Omega\left\{\hat{\mathbf{v}}^*\cdot\left[\sigma\hat{\mathbf{u}}+\mathscr{L}(\mathbf{U},Re)\hat{\mathbf{u}}+\nabla\hat{p}\right]+\hat{q}^*\nabla\cdot\hat{\mathbf{u}}\right\}= \\
&=\oint_{\partial\Omega}\hat{\mathbf{n}}\cdot\left[\mathbf{U}(\hat{\mathbf{u}}\cdot\hat{\mathbf{v}}^*)+\frac{1}{Re}(\nabla\hat{\mathbf{v}}^*)\cdot\hat{\mathbf{u}}-\frac{1}{Re}(\nabla\hat{\mathbf{u}})\cdot\hat{\mathbf{v}}^*+\hat{p}\hat{\mathbf{v}}^*+\hat{q}^*\hat{\mathbf{u}}\right],
\end{aligned} \tag{1.36}$$

where the right-hand side is obtained applying the divergence theorem. Since homogeneous boundary conditions are imposed for direct and adjoint eigenfunctions, the right-hand side is null and the previous equation becomes

$$\int_\Omega\left\{\hat{\mathbf{v}}^*\cdot\left[\sigma\hat{\mathbf{u}}+\mathscr{L}(\mathbf{U},Re)\hat{\mathbf{u}}+\nabla\hat{p}\right]+\hat{q}^*\nabla\cdot\hat{\mathbf{u}}\right\}=0. \tag{1.37}$$

This last result is now substituted in the perturbed direct eigenvalue problem such that the equation (1.31) results

$$\int_\Omega\hat{\mathbf{v}}^*\cdot\left[-\sigma'\hat{\mathbf{u}}-\mathscr{L}'(\mathbf{U})\hat{\mathbf{u}}\right]=0 \tag{1.38}$$

and inverting this relation it is possible to calculate the modulus of σ'

$$|\sigma'|=\frac{\left|\int_\Omega\hat{\mathbf{v}}^*\cdot\mathscr{L}'(\mathbf{U})\hat{\mathbf{u}}\right|}{\left|\int_\Omega\hat{\mathbf{v}}^*\cdot\hat{\mathbf{u}}\right|}. \tag{1.39}$$

If the perturbation is localised in a point of the flow field, it can be expressed in the form of a Dirac delta function δ and, thus, the perturbed operator becomes

$$\mathscr{L}' = \delta(x - x_0, y - y_0, z - z_0)\mathbf{L} \tag{1.40}$$

where x_0, y_0 and z_0 are the coordinates of the perturbation point and $\mathbf{L}$ is a tensor whose dimension is equal to the number of space dimensions. Thanks to the Dirac delta function properties, the modulus of the perturbation (1.39) can be written as

$$|\sigma'| = \frac{|\hat{\mathbf{v}}^*(x,y,z)\mathbf{L}\hat{\mathbf{u}}(x,y,z)|}{\left|\int_\Omega \hat{\mathbf{v}}^* \cdot \hat{\mathbf{u}}\right|} \tag{1.41}$$

and the application of the Cauchy-Schwarz inequality leads to the following relation

$$|\sigma'| \leq \|\mathbf{L}\| \frac{\|\hat{\mathbf{v}}^*(x,y,z)\|\|\hat{\mathbf{u}}(x,y,z)\|}{\left|\int_\Omega \hat{\mathbf{v}}^* \cdot \hat{\mathbf{u}}\right|}, \tag{1.42}$$

which permits to define the structural sensitivity parameter

$$s(x,y,z) = \frac{\|\hat{\mathbf{v}}^*(x,y,z)\|\|\hat{\mathbf{u}}(x,y,z)\|}{\left|\int_\Omega \hat{\mathbf{v}}^* \cdot \hat{\mathbf{u}}\right|}. \tag{1.43}$$

Where $s(x,y,z)$ is maximum, the system will be more sensitive to the perturbation and, consequently, in these points the wavemaker, i.e. the region where the instability mechanism acts, is localized. In particular, the variation of the eigenvalue with larger real part is proportional to the product between the direct and the adjoint eigenvector of the least stable mode.

Following the approach of Luchini and Bottaro [23], the structural sensitivity parameter can be computed even considering generalized, discrete direct and adjoint problems

$$\mathbf{A}\hat{\mathbf{b}} = \sigma\mathbf{M}\hat{\mathbf{b}} \quad \text{and} \quad \hat{\mathbf{c}}^*\mathbf{A} = \sigma\hat{\mathbf{c}}^*\mathbf{M}, \tag{1.44}$$

where $\mathbf{A}$ is the discrete matrix that describes the dynamics of the system while $\mathbf{M}$ is the discrete mass matrix.

The differentiation of the direct and the adjoint eigenvalue problems gives

$$|\sigma'| = \frac{\hat{\mathbf{c}}^*\delta\mathbf{A}\hat{\mathbf{b}}}{\hat{\mathbf{c}}^*\mathbf{M}\hat{\mathbf{b}}}, \tag{1.45}$$

and, if $\delta\mathbf{A}$ is a localized perturbation, the previous identity can be rewritten in the following form

$$|\sigma'| = \frac{\hat{c}_i^* \, \hat{b}_j}{\hat{\mathbf{c}}^* \mathbf{M} \hat{\mathbf{b}}} \delta A_{ij}. \tag{1.46}$$

The perturbation δA_{ij} represents the effect of a localised force in a point i which is held proportional to the velocity perturbation in a point j, for example thanks to a feedback mechanism. In this way, the previous equation can be seen as the discrete form of the equation (1.41), and, in addition to underline that the structural sensitivity is proportional to the product of the direct and adjoint eigenfunctions, it permits to evidence that the sensitivity parameter s quantifies the effect of the perturbation of the system, taking into account the influence of the perturbation of the matrix $\mathbf{A}$, which describes the dynamic of the system.

1.4 Receptivity

The structural sensitivity permits to investigate the effects of a localized velocity feedback on the linearized Navier–Stokes equations, but other types of disturbance can act on the system. Thanks to the receptivity it is possible to study the effects of external forcing and initial and boundary conditions on the asymptotic behaviour of the system. An interesting tool useful for the analysis of the response of a linear dynamic system is the Laplace transform, which, when it is applied to the linearized Navier–Stokes equations (1.8) with the initial and boundary conditions (1.7), gives

$$\begin{cases} \sigma\hat{\mathbf{u}} + (\mathbf{U}\cdot\nabla)\hat{\mathbf{u}} + (\hat{\mathbf{u}}\cdot\nabla)\mathbf{U} + \dfrac{1}{Re}\nabla^2\hat{\mathbf{u}} + \nabla\hat{p} = \hat{\mathbf{f}} + \mathbf{u}_0 \\ \nabla\cdot\hat{\mathbf{u}} = \hat{Q} \\ \hat{\mathbf{u}}(\mathbf{r},\sigma) = \hat{\mathbf{u}}_w(\mathbf{s},\sigma) \quad \text{on } \Gamma_c \quad \forall\sigma \\ \hat{\mathbf{b}}(\mathbf{r},\sigma) \to \mathbf{0} \quad \text{as } \mathbf{r}\to\infty \quad \forall\sigma, \end{cases} \tag{1.47}$$

where " ˆ " indicates the generic transformed quantity while σ is the Laplace variable. The system can also be rewritten in this matrix form

$$\begin{bmatrix} \sigma + \mathscr{L}(\mathbf{U}, Re) & \nabla \\ \nabla\cdot & 0 \end{bmatrix} \begin{bmatrix} \hat{\mathbf{u}} \\ \hat{p} \end{bmatrix} = \begin{bmatrix} \hat{\mathbf{f}} + \mathbf{u}_0 \\ \hat{Q} \end{bmatrix}, \tag{1.48}$$

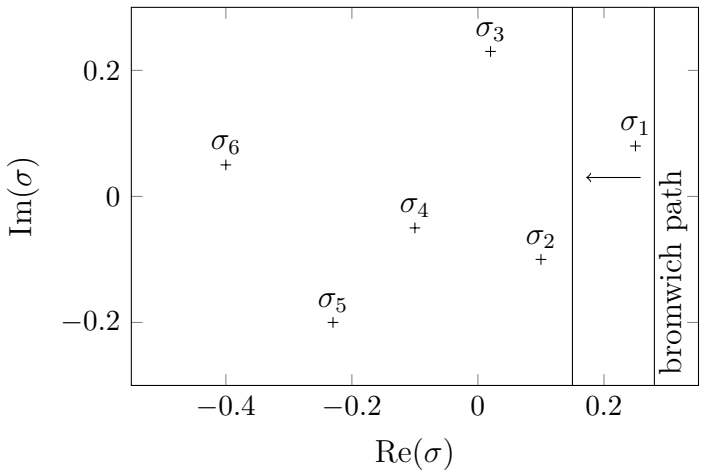

FIGURE 1.1. Bromwich integration path.

and thanks to the Mellin transform the response of the system in the time domain is

$$\begin{bmatrix} \hat{\mathbf{u}} \\ \hat{p} \end{bmatrix} = \frac{1}{2\pi i} \int_{\gamma - i\infty}^{\gamma + i\infty} e^{\sigma t} \begin{bmatrix} \sigma + \mathscr{L}(\mathbf{U}, Re) & \nabla \\ \nabla \cdot & 0 \end{bmatrix}^{-1} \begin{bmatrix} \hat{\mathbf{f}} + \mathbf{u}_0 \\ \hat{Q} \end{bmatrix} d\sigma, \tag{1.49}$$

where γ is a real number such that all the singularities of the system are on the left of the integration path, which is also called Bromwich path, as is shown in figure 1.1. In particular, γ has to be larger than the real part of σ_1 which is the singularity associated to least stable mode that dominates the response of the system for large time. In fact, if $\mathrm{Re}(\sigma_1) > 0$ the response will diverge with an exponential trend, while if $\mathrm{Re}(\sigma_1) < 0$ the response will decay as $exp(\sigma_1 t)$ and, therefore, the long time behaviour of the flow is characterized by the nature of σ_1.

Thanks to the integration properties of the analytic functions, the Bromwich path can be modified and, in particular, it can be moved on the left such that the first singularity σ_1 is out of the path (see figure 1.1). In order to maintain the same value of the integral (1.49), it is necessary to consider the residual of σ_1 and the response of the system becomes

$$\begin{aligned} \begin{bmatrix} \mathbf{u} \\ p \end{bmatrix} =& Res\left(e^{\sigma t} \begin{bmatrix} \sigma + \mathscr{L}(\mathbf{U}, Re) & \nabla \\ \nabla \cdot & 0 \end{bmatrix}^{-1} \begin{bmatrix} \hat{\mathbf{f}} + \mathbf{u}_0 \\ \hat{Q} \end{bmatrix} \right) + \\ &+ \frac{1}{2\pi i} \int_{\gamma_1 - i\infty}^{\gamma_1 + i\infty} e^{\sigma t} \begin{bmatrix} \sigma + \mathscr{L}(\mathbf{U}, Re) & \nabla \\ \nabla \cdot & 0 \end{bmatrix}^{-1} \begin{bmatrix} \hat{\mathbf{f}} + \mathbf{u}_0 \\ \hat{Q} \end{bmatrix} d\sigma, \end{aligned} \tag{1.50}$$

where, for long time, the second term of the right-hand side is null while the

first term can be related to the most unstable eigenvalue σ_1 in this way

$$Res(\sigma_1) = \lim_{\sigma\to\sigma_1}(\sigma-\sigma_1)\left(e^{\sigma t}\begin{bmatrix}\sigma+\mathscr{L}(\mathbf{U},Re) & \nabla\\ \nabla\cdot & 0\end{bmatrix}^{-1}\begin{bmatrix}\hat{\mathbf{f}}+\mathbf{u}_0\\ \hat{Q}\end{bmatrix}\right). \quad (1.51)$$

This limit is calculated thanks to the adjoint operator. Starting from the generic adjoint eigenfunction $\{\mathbf{v}_i, q_i\}$ relative to the eigenvalue σ_i, the Laplace transform and the successive integration of the equation (1.21), which was obtained applying the generalised Lagrange identities to the Navier–Stokes equations, gives

$$\begin{aligned}\int_\Omega(\hat{\mathbf{v}}_i^*\cdot[\sigma\hat{\mathbf{u}}+(\mathbf{U}\cdot\nabla)\hat{\mathbf{u}}+(\hat{\mathbf{u}}\cdot\nabla)\mathbf{U}-\frac{1}{Re}\nabla^2\hat{\mathbf{u}}+\nabla\hat{p}]+\hat{q}_i^*\nabla\cdot\hat{\mathbf{u}})+\\ +\int_\Omega([-\sigma_i\hat{\mathbf{v}}_i^*+(\mathbf{U}\cdot\nabla)\hat{\mathbf{v}}_i^*-(\nabla\mathbf{U})\cdot\hat{\mathbf{v}}_i^*+\frac{1}{Re}\nabla^2\hat{\mathbf{v}}_i^*+\nabla\hat{q}_i^*]\cdot\hat{\mathbf{u}}+\nabla\cdot\hat{\mathbf{v}}_i^*\hat{p})=\\ =\int_\Omega((\sigma-\sigma_i)\hat{\mathbf{v}}_i^*\cdot\hat{\mathbf{u}}+\nabla\cdot[\hat{\mathbf{v}}_i^*\cdot\hat{\mathbf{u}}\mathbf{U}-\frac{1}{Re}(\nabla\hat{\mathbf{u}})\cdot\hat{\mathbf{v}}_i^*+\frac{1}{Re}(\nabla\hat{\mathbf{v}}_i^*)\cdot\hat{\mathbf{u}}+\hat{p}\hat{\mathbf{v}}_i^*+\hat{q}^i\hat{\mathbf{u}}]).\end{aligned} \quad (1.52)$$

The second line of the left-hand side corresponds to the adjoint eigenvalue problem and, consequently, is zero. Considering the linearized and transformed equations (1.47) the first line of the left-hand side can be rewritten in a different form such that the previous equation becomes

$$\begin{aligned}\int_\Omega\left[\hat{\mathbf{v}}_i^*\cdot(\mathbf{u}_0+\hat{f})+\hat{q}_i^*\hat{Q}\right]=\int_\Omega(\sigma-\sigma_i)\hat{\mathbf{v}}_i^*\cdot\hat{\mathbf{u}}+\\ +\int_\Omega\nabla\cdot\left[(\hat{\mathbf{v}}_i^*\cdot\hat{\mathbf{u}})\mathbf{U}+\frac{1}{Re}(\nabla\hat{\mathbf{v}}_i^*)\cdot\hat{\mathbf{u}}-\frac{1}{Re}(\nabla\hat{\mathbf{u}})\cdot\hat{\mathbf{v}}_i^*+\hat{p}\hat{\mathbf{v}}_i^*+\hat{q}_i^*\hat{\mathbf{u}}\right].\end{aligned} \quad (1.53)$$

Applying the divergence theorem to the second integral of the right-hand side and considering homogeneous conditions on the boundary for $\mathbf{v}_i$ and that the adjoint field has to decay for $r\to\infty$, an equation for $\hat{\mathbf{u}}$ is obtained

$$(\sigma-\sigma_i)\int_\Omega\hat{\mathbf{v}}_i^*\cdot\hat{\mathbf{u}}=\int_\Omega\mathcal{F}_i-\int_{\partial\Omega}\mathcal{B}_i, \quad (1.54)$$

where $\mathcal{F}_i=\hat{\mathbf{v}}_i^*\cdot(\mathbf{u}_0+\hat{f})+\hat{q}_i^*\hat{Q}$ and $\mathcal{B}_i=\hat{\mathbf{n}}\cdot\left[\frac{1}{Re}(\nabla\hat{\mathbf{v}}_i^*)\cdot\hat{\mathbf{u}}_w+\hat{q}_i^*\hat{\mathbf{u}}_w\right]$, which take into account the effects of the external forcing and the boundary conditions, respectively. If the problem is diagonalizable, i.e. the eigenfunctions form a complete orthogonal set, $\hat{\mathbf{u}}$ can be expressed as the linear combination of the direct eigenfunctions $\hat{\mathbf{u}}_j$ in this way

$$\hat{\mathbf{u}}(\mathbf{r},\sigma)=\sum_{j=1}^{\infty}\hat{A}_i(\sigma)\hat{\mathbf{u}}_j(\mathbf{r}) \quad (1.55)$$

where $\hat{A}_j$ are multiplicative coefficients. Considering that $\hat{\mathbf{v}}_i$ is the Laplace transform of the generic adjoint eigenfunction, the properties of orthogonality between the direct and adjoint eigenfunctions and the previous expansion permit to rewrite the left hand side of the equation (1.54) as

$$(\sigma - \sigma_i)\hat{A}_i(\sigma) \int_\Omega \hat{\mathbf{v}}_i^* \cdot \hat{\mathbf{u}}_i, \tag{1.56}$$

from which the i-th coefficient of the linear combination (1.55) is computed

$$\hat{A}_i(\sigma) = \frac{\int_\Omega \mathcal{F}_i - \int_{\partial\Omega} \mathcal{B}_i}{(\sigma - \sigma_i) \int_\Omega \hat{\mathbf{v}}_i^* \cdot \hat{\mathbf{u}}_i}. \tag{1.57}$$

For the study of the long time behaviour of the system, the application of the equation (1.51), where the only effect of the eigenvalue with the largest real part was considered through its residual, gives this form for the coefficients in time

$$A_i(t) = \lim_{\sigma \to \sigma_1} (\sigma - \sigma_1) e^{\sigma t} \frac{\int_\Omega \mathcal{F}_i - \int_{\partial\Omega} \mathcal{B}_i}{(\sigma - \sigma_i) \int_\Omega \hat{\mathbf{v}}_i^* \cdot \hat{\mathbf{u}}_i}, \tag{1.58}$$

and so

$$A_i(t) = \begin{cases} 0 & \text{if } \sigma_i \neq \sigma_1 \\ e^{\sigma_1 t} \dfrac{\int_\Omega \mathcal{F}_1 - \int_{\partial\Omega} \mathcal{B}_1}{\int_\Omega \hat{\mathbf{v}}_1^* \cdot \hat{\mathbf{u}}_1} & \text{if } \sigma_i = \sigma_1. \end{cases} \tag{1.59}$$

Since $A_1(t)$ depends linearly on the forcing, each term of the numerator can be studied separately from each other and, considering also in this case localized forcing, the amplitude of the coefficient will be determined by the local value of $\hat{\mathbf{v}}_1^*$ and $\hat{q}_1^*$. Considering, for example, the effect of an external force, it can be noticed how the projection of $\hat{\mathbf{f}}$ in the direction of the eigenfunction $\hat{\mathbf{v}}_1$ associated to the most unstable eigenvalue plays an important role. In fact if the system is forced by a force orthogonal to $\hat{\mathbf{v}}_1$, i.e $\hat{\mathbf{f}}$ has the shape of one of the other direct eigenfunctions, its effect on the long time behaviour is null. So, if $\mathbf{f}$, Q, $\mathbf{u}_0$ and $\mathbf{u}_w$ are taken such that they are orthogonal to the eigenfunction associated to σ_1, their effect for long time is null and, consequently, to understand how external forcing and initial and boundary conditions affect the system response, the integration path has to be further moved excluding also the eigenvalue σ_2.

A last important remark concerns the definition of long time. In fact, it is important to remember that the original Navier–Stokes system is non-linear and so a long time is such that the non-linear effects do not affect the system response when the system is unstable.

2 | Numerical model

For the simulation of the flow inside the open cavity the NEK5000 package has been used. NEK5000 is an open source computational fluid dynamic solver developed by Paul Fischer, Lee Ho, Einar Rønquist and others at the Mathematics and Computer Science Division of Argonne National Laboratory. This code, which is written in Fortran77/C with the MPI standard for parallelism, is based on the spectral element method (SEM) and it models incompressible, steady and unsteady flows, passive scalar transport, heat transfer problems and time-dependent geometries.

In this section the most important features of this code will be briefly described. For more information, the reader can refer to the NEK5000 manual and web site (`http://nek5000.mcs.anl.gov/index.php/Main_Page`).

2.1 Spatial discretization

In order to approximate the solution of the Navier–Stokes equations (1.1) by a spectral method, the spatial domain of the problem is divided into hexaedral elements generating an unstructured mesh. In particular, in NEK5000, a spectral element method (SEM) is implemented and the solution is approximated with high order polynomials. In this way, the method is characterized by the high accuracy typical of spectral methods, by a relative low computational cost and, at the same time, by a good geometric flexibility, which is instead typical of the methods that use meshes of tetrahedral elements, like FEM (finite element methods). In the following the spectral element method will be introduced (refer to [27] and [7] for a more complete and detailed review of these methods).

2.1.1 Spectral element method

Consider the mono-dimensional Poisson equation defined on the domain $\Omega = (-1, 1)$

$$\begin{cases} -\dfrac{d^2u}{dx^2} = f(x) \quad \text{in } \Omega \\ u(0) = u(1) = 0 \end{cases} \tag{2.1}$$

whose discrete formulation is: find $u \in X_0^N$ such that

$$\int_0^1 \frac{dv}{dx}\frac{du}{dx}dx = \int_0^1 vf dx \quad \forall v \in X_0^N \tag{2.2}$$

where $X_0^N = \{\phi_j(x), \phi(0) = \phi(1) = 0 \text{ for } j = 1, n\}$ is the finite-dimensional trial space. If the solution and the external forcing of the problem are approximated as

$$u(x) = \sum_{j=1}^{n} \phi_j(x)\hat{u}_j \quad \text{and} \quad f(x) = \sum_{j=1}^{n} \phi_j(x) f_j \tag{2.3}$$

where $\hat{u}_j$ and f_j are the expansion and forcing coefficients respectively, it is possible to rewrite the variational problem in the following matrix form

$$A\hat{\mathbf{u}} = M\mathbf{f} \tag{2.4}$$

where A and M are the stiffness and the mass matrices, whose coefficients are defined as

$$A_{ij} = \int_\Omega \phi_j'\phi_i' d\Omega \quad \text{and} \quad M_{ij} = \int_\Omega \phi_j\phi_i d\Omega \tag{2.5}$$

and $\hat{\mathbf{u}}$ and $\mathbf{f}$ are the vectors containing the unknown coefficients and of the external forcing.

For the implementation of the numerical scheme it is now important to select the approximation space and a basis. In particular, the mathematical space will influence the convergence of the discrete solution, while the basis functions influence the complexity and the performance of the method. For spectral element methods the space X^N of the approximate solution is the space of the piecewise polynomial functions of degree N defined on each element $\Omega_e,\ e = 1, ..., E$, of the discretization. Typically, the degree N of these polynomials is in the range $[5, 15]$. In this space, the classical choice for the approximation basis is represented by nodal Lagrangian polynomials $L(x)$ based on the Gauss–Legendre–Lobatto (GLL) or on the Gauss–Legendre (GL)

quadrature points, which are polynomials characterized by the orthogonality property with respect to the $L^2(\Omega)$ inner product

$$\int_{-1}^{1} L_i(x)L_j(x)dx = \delta_{ij} \tag{2.6}$$

where δ_{ij} stands for the Kronecker delta.

The GLL and GL quadrature points are very useful because they yield relatively well conditioned linear systems. Unfortunately, increasing the degree N of the Lagrangian polynomials the condition number suffers a slow increase. These points are selected also because they permit to approximate the integrals in the variational formulation with the Gauss quadrature rules. Considering a reference element $\hat{\Omega}$ in the range $x = (-1, 1)$ the quadrature points can be classified as follow:

- Gauss–Legendre points: they are calculated as the zeros of the N-degree Legendre polynomial. Since they are all inside the element, a Lagrangian basis built on them does not guarantee the continuity of the solution between two successive elements. Considering a generic M-degree polynomial $q(x)$, the integral of this function in the reference domain can be approximated as

  $$\int_{-1}^{1} q(x)dx = \sum_{k=0}^{N} \rho_k q(\xi_k) \tag{2.7}$$

  where ξ_k are the quadrature points, ρ_k are the quadrature weights and N is the degree of the approximation functions. With the Gauss–Legendre quadrature points it is possible to integrate exactly all the polynomials with a degree $M < 2N + 1$;

- Gauss–Legendre–Lobatto points: to guarantee the continuity of the basis functions between two successive elements, these quadrature points are calculated imposing that the first and the last points are in correspondence of the element extremes and, therefore, $\xi_1 = -1$ and $\xi_N = 1$. The other points are located in correspondence of the zeros of the first derivative of the N-degree Legendre polynomial. In this way the continuity of the solution can be automatically satisfied but, since the position of two of the quadrature points is fixed varying N, it is possible to integrate exactly all the polynomials with a degree $M < 2N - 1$. Since they are useful to impose the continuity of the approximation, the GLL points are commonly used to build the polynomial basis.

Looking at matrix coefficients defined in (2.5), it is apparent that a diagonal approximate mass matrix is obtained if a GLL quadrature formula is employed

to approximate the integrals and if the Lagrangian basis is defined on the same quadrature nodes. Furthermore, with GLL points, the stiffness matrix is obtained exactly since the function to be integrated is a polynomial of degree $2N - 2$. The stiffness matrix is however full.

2.1.2 Convergence

The indisputable advantage of the spectral element methods with respect to the finite element method is that the rate of convergence of the numerical solution depends only on the regularity of the exact solution and on the degree of the interpolant polynomials. In particular, if the degree N of the polynomials is varied, the higher is the solution regularity, the higher is the rate of convergence. Considering that the solution of the Navier–Stokes equations is smooth when the boundary is also smooth, the rate of h-convergence depends only on the polynomial degree, while the rate of p-convergence is exponential. So, in NEK5000, an increase of the elements number E permits to have an algebraic decrease of the numerical error, like E^{-N}, while, if the solution is smooth, an increase of the polynomial degree N induces an exponential decrease of the error, like $e^{-\alpha N}$.

2.2 Temporal discretization

Beside the spatial discretization obtained by the spectral element method, to obtain the fully discrete equations it is necessary to introduce a time discretization. Owing to the presence of the non-linear term the use of an implicit time integration scheme, like the Crank–Nicolson scheme or a BDF scheme (backward differentiation formula), which are not subject to instability problems, can be very expensive since it requires the solution of a non-linear and non-symmetric problem at each time step.

To fix this problem, in NEK5000 it is been chosen to use a BDF scheme of order k (with $k = 1$, 2 or 3) for the generalized Stokes operator, while, to avoid the solution of the non-linear system, the convective term is approximated with a Richardson extrapolation of order k. In this way, the scheme, which is named BDFk-EXTk, is explicit and formally k-order accurate in time.

2.2.1 Stability

The consequence of the Richardson extrapolation is that the numerical integration method is semi-implicit and, therefore, it suffers a limitation on the time step Δt to avoid numerical instabilities. In particular, it is important

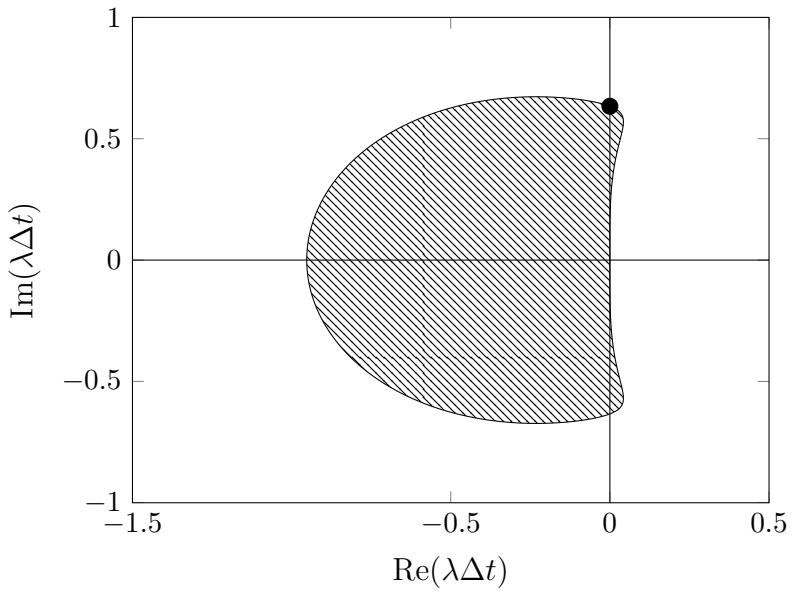

FIGURE 2.1. Absolute stability region for the BDF3-EXT3 time integration method.

to guarantee that the method is stable and that the numerical solutions are accurate also for Δt sufficiently large. To this aim, we consider the model problem given by

$$\begin{cases} \dfrac{\partial y}{\partial t} = \lambda y \\ y\left(0\right) = y_0 = 1 \end{cases} \tag{2.8}$$

whose exact solution is

$$y = y_0 e^{\lambda t} = e^{\lambda t} \tag{2.9}$$

which is null for $t \to \infty$ when $\lambda \in \mathbb{C}$ is a complex number with negative real part. Applying the numerical integration method to the modal problem, it is possible to identify the absolute stability region which is given by the set of values in the $\lambda\Delta t$ complex plane where the method is absolutely stable, i.e. the discretized solution goes to zero when the numerical integration time step goes to infinity. As it is shown in figure 2.1, since the BDF3-EXT3 scheme is explicit, the absolute stability region is given by a limited portion of the complex plane and this implies that this integration method is only conditionally absolutely stable. So, the only way to have a stable method is to impose a maximum limit on the value of the time step Δt, which, looking

at the figure 2.1, is

$$\Delta t < \frac{\tilde{z}}{\max|\lambda|} \tag{2.10}$$

where $\tilde{z}$ represent the critical value for $\lambda\Delta t$ given by the intersection of the absolute stability region with the imaginary axis (for BDF3-EXT3 it is indicated with the star in the figure and is equal to 0.6339) while $\max|\lambda|$ depends on the numerical method used for the spatial discretization. Considering, for example, a simple convection problem characterized by a convective velocity equal to $\mathbf{d}$ and discretized with a spectral element method, the maximum value for the module of λ is given by

$$\max|\lambda| = S\frac{|\mathbf{d}|}{\Delta x_{min}} \tag{2.11}$$

where S depends on the order N of the approximation polynomials and it ranges from 1.52 when $N = 3$ to 1.16 when $N = \infty$ while Δx_{min} is the minimum spatial discretization interval which scales with $O\left(N^{-2}\right)$ because of the clustering of the GLL points near the boundaries of the reference interval. Substituting these results in the previous equation we obtain

$$\Delta t < \frac{\tilde{z}\Delta x_{min}}{S\mathbf{d}} \;\Rightarrow\; \frac{\Delta t\ \mathbf{d}}{\Delta x_{min}} < C \tag{2.12}$$

which represent the CFL condition that imposes a limit on the maximum value of the time step. In the case of Navier–Stokes equations the limit on the time step is

$$\Delta t < C\ \min\left\{\frac{\Delta x}{|u|}, \frac{\Delta y}{|v|}, \frac{\Delta z}{|w|}\right\} \tag{2.13}$$

where C is the Courant number.

2.3 Application to the Navier–Stokes equations

The application of temporal discretization described in the previous section to the Navier–Stokes equations (1.1) leads the following system

$$\begin{cases} \mathcal{H}\mathbf{u}^n + \nabla p^n = \beta_1\tilde{\mathbf{u}}_1^n + \beta_2\tilde{\mathbf{u}}_2^n + \beta_3\tilde{\mathbf{u}}_3^n \\ \nabla\cdot\mathbf{u}^n = 0 \end{cases} \tag{2.14}$$

where $\mathbf{u}^n$ and p^n are the velocity and pressure fields at the time n, while $\mathcal{H}$ is the Helmholtz operator

$$\mathcal{H} = (-\frac{1}{Re}\nabla^2 + \frac{\beta_0}{\Delta t}) \tag{2.15}$$

and β_0, β_1, β_2 and β_3 are the four coefficients derived from the BDF3-EXT3 temporal scheme. The right-hand side of the first equation of the system (2.14) is composed by the inhomogeneous terms $\tilde{\mathbf{u}}_l^n$ deriving from temporal discretization which are computed as the solution of a pure convection problem with an explicit Runge–Kutta scheme

$$\begin{cases} \dfrac{\partial \tilde{\mathbf{u}}_l}{\partial t} + \mathbf{u} \cdot \nabla \tilde{\mathbf{u}}_l = 0 \\ \tilde{\mathbf{u}}_l(\mathbf{x}, t^{n-l}) = \mathbf{u}(\mathbf{x}, t^{n-l}) \end{cases} \tag{2.16}$$

In the following these three terms are rewritten in a compact form as $\mathbf{f}$.

Now, in order to find a discrete solution to the Navier–Stokes equations, it is necessary to introduce the SEM spatial discretization. The introduction of the Gauss quadrature rules for the approximation of the $L^2(\Omega)$ inner products in the weak formulation of the equations (2.14) leads to this new problem: find $\mathbf{u} \in X^N$ and $p \in Y^N$ such that

$$\begin{cases} \dfrac{1}{Re}(\nabla \mathbf{u}, \nabla \mathbf{v})_{GLL} + \dfrac{\beta_0}{\Delta t}(\mathbf{u}, \mathbf{v})_{GLL} + \\ \qquad\qquad -(p, \nabla \cdot \mathbf{v})_{GL} = (\mathbf{f}, \mathbf{v})_{GLL} \quad \forall \mathbf{v} \in X^N \\ -(q, \nabla \cdot \mathbf{u})_{GL} \quad \forall q \in Y^N \end{cases} \tag{2.17}$$

where $(\cdot, \cdot)_{GLL}$ and $(\cdot, \cdot)_{GL}$ denote the Gauss-Legendre-Lobatto and the Gauss-Legendre quadrature points, respectively.

When discretising the Navier–Stokes equations by the Galerkin method, an instability can arise which leads to spurious pressure oscillation. This instability can be avoided if the *inf-sup* condition, named LBB after Ladyzhenskaya, Babuska and Brezzi, is satisfied. Considering a polynomial approximation for the Navier–Stokes unknowns, this condition implies that the polynomial space used to approximate the velocity has to be sufficiently *reacher* with respect to the space employed to approximate the pressure. This can be achieved using different grids for the two discrete fields. In the case of NEK5000, where the spectral element method is implemented, if N-degree polynomials are used to approximate the velocity field, $(N-2)$-degree polynomials have to be used for the pressure.

2.4 Time splitting

As shown by Couzy [13], the previous discrete system can be rewritten in matrix formulation as

$$\begin{bmatrix} H & -HQD^T \\ -D & 0 \end{bmatrix} \begin{Bmatrix} \hat{\mathbf{u}}^n \\ \hat{p}^n - \hat{p}^{n-1} \end{Bmatrix} = \begin{Bmatrix} M\mathbf{f} + D^T\hat{p}^{n-1} \\ f_p \end{Bmatrix} + \begin{Bmatrix} \mathbf{r} \\ 0 \end{Bmatrix} \tag{2.18}$$

where D is the matrix associated to the gradient differential operator, H is the discrete Helmholtz operator, $\mathbf{r}$ is a residual term defined as

$$\mathbf{r} = (HQ - I)D^T(\hat{p}^{n-1} - \hat{p}^n) \tag{2.19}$$

and Q is an auxiliary matrix for which two choices are possible. The first one imposes $Q = H^{-1}$ in order to have a null residual, while the second one, which is more computational convenient, defines Q as

$$Q = \frac{\Delta t}{\beta_0} M^{-1} \tag{2.20}$$

and, consequently, the residual term becomes

$$\mathbf{r} = \frac{\delta t}{\beta_0 Re} A M^{-1} D^T(\hat{p}^n - \hat{p}^{n-1}) = O(\Delta t^2). \tag{2.21}$$

Since the discretized velocity field is multiplied by H which is dependent on Δt, the effective error due to the truncation of the residual term is proportional to $O(\Delta t^3)$, and so, also if a BDF3-EXT3 scheme is implemented, the method is globally second-order accurate in time. The application of the Gauss elimination leads to the last formulation of the Navier–Stokes system, which was proposed for the first time in the paper by Blair Perot [4]

$$\begin{bmatrix} H & -\dfrac{\Delta t}{\beta_0} H M^{-1} D^T \\ 0 & F \end{bmatrix} \begin{Bmatrix} \hat{\mathbf{u}}^n \\ \hat{p^n} - \hat{p}^{n-1} \end{Bmatrix} = \begin{Bmatrix} M\mathbf{f} + D^T\hat{p}^{n-1} \\ g \end{Bmatrix} \tag{2.22}$$

where

$$F = \frac{\Delta t}{\beta_0} D M^{-1} D^T \tag{2.23}$$

and g takes into account the inhomogeneous term for the pressure after the Gauss elimination. Once g computed, it is necessary to solve two systems to advance in time the Navier–Stokes equations: the first one involves the pressure and the operator F, while the second one involves the discrete velocity

field $\hat{\mathbf{u}}$ and the Helmholtz operator H. Both systems are solved with iterative techniques and, since H is a diagonally-dominant matrix, the second system is well conditioned and the solution is obtained by the Jacobi-preconditioned conjugate gradient method. For the pressure, the operator F, which can be seen as a Poisson operator, has a conditioning number independent on Δt and Re and the solution of this system is obtained by an overlapping additive Schwarz preconditioner which is well described by Fisher in [17].

2.5 Eigenvaule problem

In order to determine the onset of the instability of the flow over the open cavity, the indirect Lyapounov method is applied, which consists of computing the spectra and looking at the sign of the eigenvalue with maximum real part. Furthermore, the receptivity and the sensitivity analysis require the direct and adjoint eigenvectors of the system.

2.5.1 Direct modes

To obtain the direct eigenfunctions for the open cavity flow, it is necessary to solve the discretized eigenvalue problem (1.27), which, after the calculation of the base flow $\mathbf{W}$, can be rewritten as

$$\Big[\mathbf{A}(Re, \mathbf{W}) + \sigma\mathbf{M}\Big]\mathbf{w} = 0. \tag{2.24}$$

In the previous equation $\mathbf{w}$ represents the direct eigenvector and $\mathbf{A}$ is the matrix obtained from the linearization of the Navier–Stokes equations which describes the evolution of the linearised system. If a numerical quadrature formula with GLL points is adopted, $\mathbf{M}$, that is the lumped mass matrix, is diagonal and its elements assume a value different from zero and dependent on the quadrature formula if the corresponding row is relative to one of the velocity components.

Since the matrix $\mathbf{A}$ is very large, the solution of the previous problem requires iterative techniques such as those based on the Arnoldi algorithm. In particular, to compute the eigenfunctions for the open cavity flow, the ARPACK library is used (`http://www.caam.rice.edu/software/ARPACK/`). This library contains a collection of subroutines useful to solve large-scale eigenvalue problems which are based on a variant of the Arnoldi algorithm called Implicitly Restarted Arnoldi Method. One of the most important characteristics of the ARPACK package is that it implements an implicit restart in order to limit the memory requirement. In particular, since this problem is solved on

a multi-processor machine, the parallel version of ARPACK, called PARPACK, is used (`http://www.caam.rice.edu/~kristyn/parpack_home.html`).

2.5.2 Adjoint modes

As previously recalled, the receptivity and the sensitivity analysis require to compute also the adjont eigenfunctions of the system. A first possibility is to consider the discretized direct eigenvalue problem (2.24) and to calculate the adjoint eigenvectors as the left eigenvectors of this problem. In practice, this is equivalent to solve a direct eigenvalue problem for the transposed matrix of the (2.24) equation. A second possibility is to discretise the continuous adjoint problem (1.34) obtained in the first chapter and then apply the Arnoldi method to the new problem. These two approaches are equivalent at convergence, hence when discretization errors annihilate. In this thesis the second approach will be used and, in particular, the discretized adjoint problem can be written as

$$\hat{\mathbf{w}}^H \left[\mathbf{A}^+(Re, \mathbf{W}) + \sigma \mathbf{M} \right] = 0 \tag{2.25}$$

and it is solved again with the ARPACK package.

2.6 Code validation

Before computing the base flow and performing the stability analysis for the open cavity problem, it is useful to test the methods previously described for a well known problem, such as the flow around a 2D cylinder. The results obtained with NEK5000 will be compared with well established results available in the literature.

Author	C_D
Dennis & Chang (1970)	1.52
Fornberg(1980)	1.50
Ye *et al* (1999)	1.52
Kim *et al* (2001)	1.51
Giannetti & Luchini (2007)	1.54
Current	1.56

TABLE 2.1. Cylinder drag coefficient for Reynolds number 40.

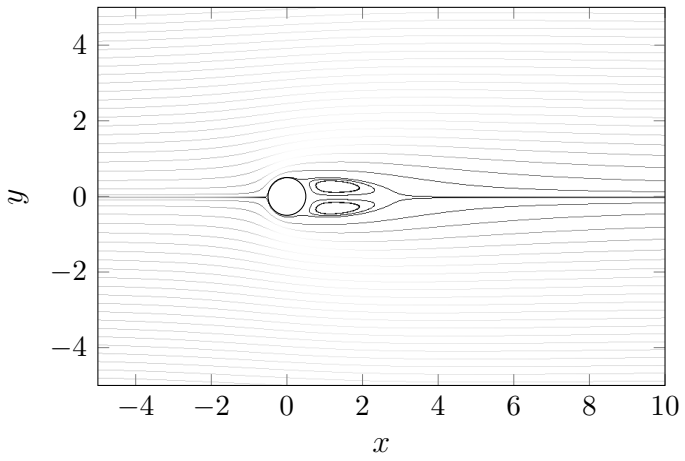

FIGURE 2.2. Cylinder flow: velocity streamlines at Reynolds number 40.

The cylinder problem is solved on a grid of size $[-15:15]\times[-15:35]$ with the cylinder centre placed in the origin of the reference frame. First, the base flow is solved in this domain for a Reynolds number equal to 40. The velocity streamlines are shown in figure 2.2 and can be successfully compared with the result obtained by Penza [25] whose calculations are performed with a finite element method and the numerical library Trilinos. Another important result confirming the validity of this code is obtained by comparing the predicted drag coefficient C_D with several results available in the literature, see table 2.1. In particular, it can be notice that the C_D calculated with NEK5000 is very similar to those obtained with other numerical techniques with small differences probably due to the domain size and boundary conditions.

It is also important to verify the solution of the eigenvalue problem performed combining NEK5000 and ARPACK. The flow spectrum obtained at $Re = 40$ is reported in figure 2.4. Also in this case the comparison with the results by Sipp and Lebedev [32] is very good. In particular the three most unstable eigenvalues, which are marked by circles in figure 2.4, are very close to those calculated by Penza. This result confirms the reliability of the method even if not all the eigenvalues are accurately reproduced, since, as a matter of fact, these three eigenvalues are numerically stable while the others are strongly dependent on the mesh refinement and on the discretization method. In the same figure the eigenvalues obtained solving the adjoint problem are also reported for comparison. Except for the two most unstable eigenvalues that match very well the ones computed solving the direct problem, the other eigenvalues are less accurate. This is caused by the poor conditioning of these eigenvalues due to non-normality of the operator and by the fact that the discretised continuous adjoint problem has been solved instead of the discrete

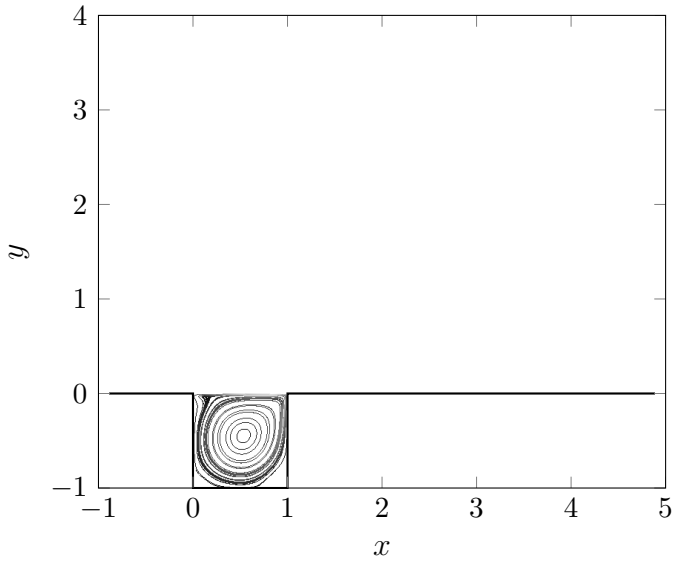

FIGURE 2.3. 2D cavity flow: velocity streamlines at Reynolds number 4135.

adjoint problem. Finally, figure 2.5 shows the horizontal component of the velocity for the most unstable direct and adjoint modes for the cylinder flow at $Re = 40$. The first result is well comparable with the direct eigenfunction calculated by Penza at $Re = 40$ while the second result is very similar to the one obtained by Sipp and Lebedev [32] at $Re = 46.6$, despite a large difference in the respective Reynolds numbers.

A second and most useful code validation is done comparing the results obtained for a two-dimensional cavity characterized by a unitary length and depth to the ones described in the paper of Sipp and Lebedev [32]. The actual computation is based on the domain illustrated in the figure 2.3 which differs from the one utilized by Sipp and Lebedev [32] by a shorter distance between the inflow boundary e upstream edge of the cavity and by a longer height of the domain. Furthermore, both in the present work and in the work of Sipp and Lebedev the incoming flow is characterized by a laminar boundary layer, which can be assimilated to a Blasius profile. In figure 2.3 the velocity streamlines inside the cavity are shown and the principal vortical structures can be recognised.

For a Reynolds number based on the cavity length of 4140, Sipp and Lebedev have obtained a spectra which exhibits a marginally stable eigenvalue characterized by $\mathrm{Im}(\sigma) = \pm 7.5$. For a validation of the code, a computation for $Re = 4135$ in the present geometry is done, that gives the spectra reported in figure 2.6. The result obtained is well comparable with the one of Sipp and Lebedev and, specifically, it is possible to notice the pres-

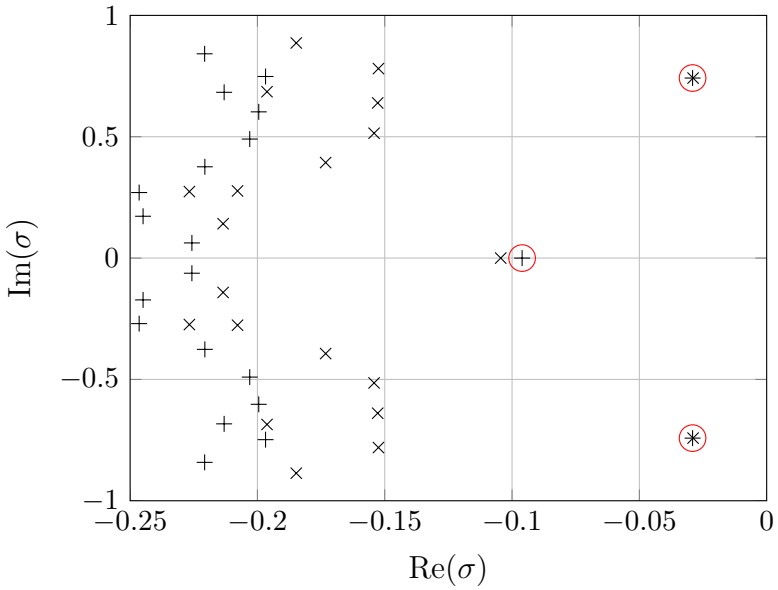

FIGURE 2.4. Cylinder flow: direct (+) and adjoint (×) eigenvalues at $Re = 40$.

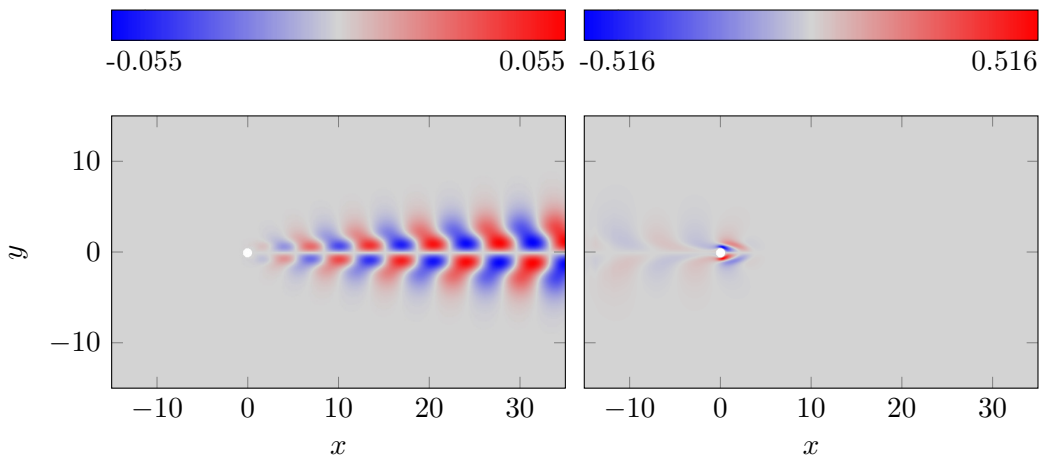

FIGURE 2.5. Cylinder flow: real part of the horizontal component of the velocity field for the most unstable direct eigenfunction (left) and real part of the horizontal component of the velocity field for the most unstable adjoint eigenfunction (right) at $Re = 40$.

ence of two complex-conjugate eigenvalues with a negative real part and with $\mathrm{Im}(\sigma) = \pm 5.3132$, which are probably the eigenvalues that becomes marginally stable for $Re = 4140$. This can be highlighted also looking at the corresponding eigenvectors (figure 2.7) that are very similar to those reported in the paper of Sipp and Lebedev. In the paper of Barbagallo, Sipp and

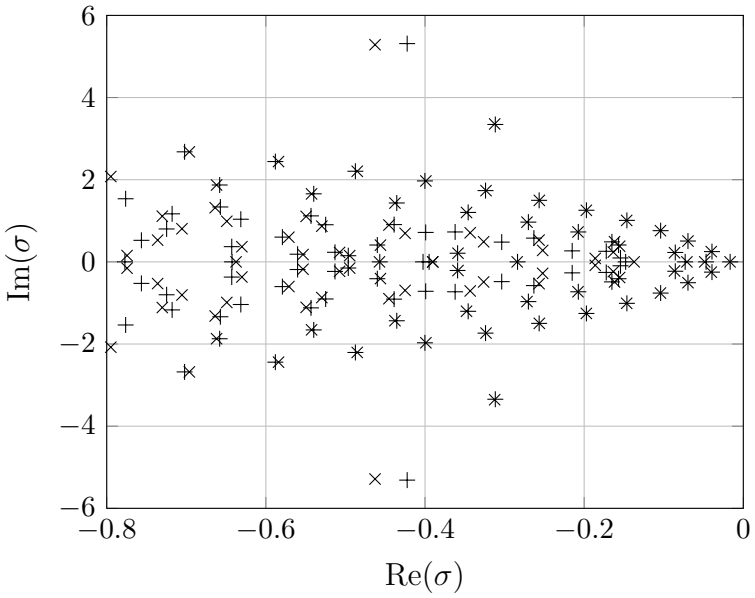

FIGURE 2.6. 2D cavity flow: direct (+) and adjoint (×) eigenvalues at $Re = 4135$.

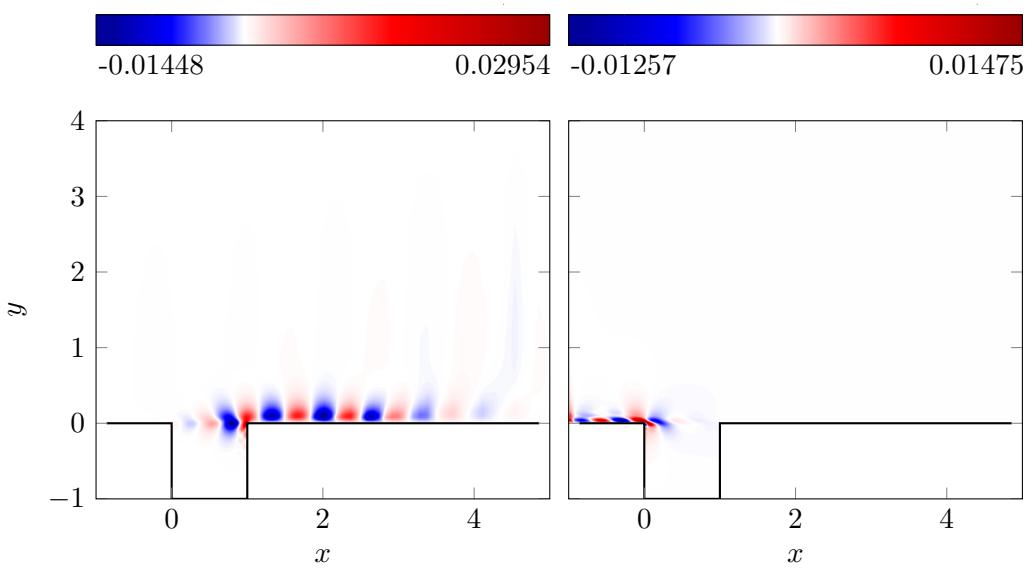

FIGURE 2.7. 2D cavity flow: real part of the vertical component of the velocity field for the most unstable direct eigenfunction (left) and real part of the vertical component of the velocity field for the most unstable adjoint eigenfunction (right) at $Re = 4135$.

Schmid [2] the eigenvalues of the cavity flow at $Re = 7500$ are shown for a geometry identical to the one utilized in the paper of Sipp and Lebedev. Also

in this case, the reported spectra and the one calculated in this thesis have approximately the same trend.

This positive comparison between the results of Sipp and Lebedev and those obtained with NEK5000 is very important for two reasons. First of all, since the results obtained are in accordance with other results already present in literature, the eigensolution computation performed with NEK5000 works fine. Second, since the mesh utilized for the three-dimensional computation is obtained thanks to a spanwise extension of the two-dimensional mesh with the introduction of the cavity lateral walls, it is plausible that the three-dimensional results will be correct.

3 | Flow morphology

This chapter focuses on the principal aspects of the flow morphology in the cavity with $AR = 2$ and $AR = 3$ varying the Reynolds number. After a briefly description of the geometry and the boundary conditions imposed, the main structures characterising the flow will be introduced. In particular, the formation of longitudinal vortices due to centrifugal forces and the behaviour of the flow in unsteady conditions will be analysed.

3.1 Mesh and boundary condition

In figure 3.1 a schematic, three-dimensional view of the open cavity is shown, illustrating the geometry of the problem in the case of cavity with aspect ratio equal to 2.

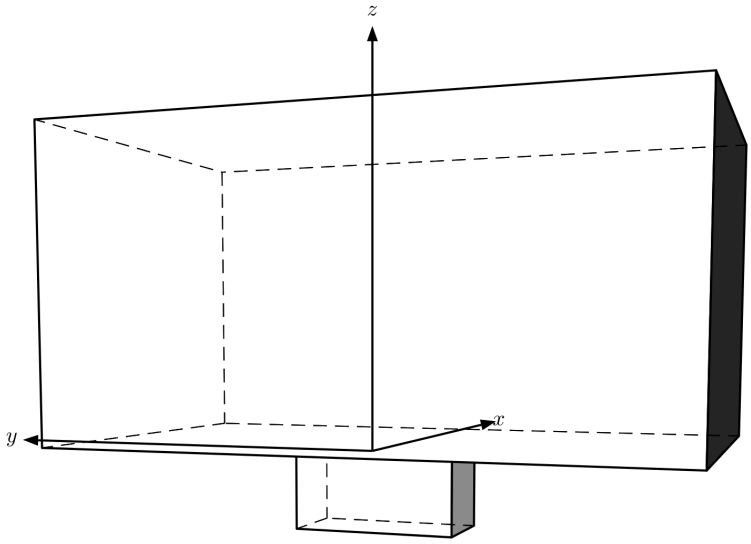

FIGURE 3.1. Three-dimensional view of the open cavity geometry with apesct ratio 2.

AR	domain dimensions	elements	cells	points
1	[-1.0, 5.0] × [-4.0, 4.0] × [-1.0, 4.0]	68320	8540000	14757120
2	[-1.0, 5.0] × [-4.5, 4.5] × [-1.0, 4.0]	99520	12440000	21496320
3	[-1.0, 5.0] × [-5.0, 5.0] × [-1.0, 4.0]	130720	16340000	28235520

TABLE 3.1. Domain dimension, number of elements, cells and points for the different aspect ratios.

In this thesis, the open cavity flow is solved for three different aspect ratios, defined as

$$AR = \frac{W}{L} = \frac{\text{dimension in } y \text{ (spanwise) direction}}{\text{dimension in } x \text{ (streamwise) direction}}. \tag{3.1}$$

In particular, the streamwise dimension L, which is the reference length for the calculation of the Reynolds number, is kept constant and equal to 1, while, to modify the aspect ratio, the spanwise dimension W is progressively increased. The depth of the cavity is kept equal to 1 for all the aspect ratios. The distance between the windward edge of the cavity and the inflow boundary is also 1, while the distance from the leeward edge of the cavity and the outflow boundary is set to 4. Finally, the distance from the cavity and the lateral planes delimiting the computational domain is 3.5 in all the computation and the height of the domain is equal to 4.

Since for the approximation of the Navier–Stokes equations (1.1) a spectral element method is used, the mesh necessary for the discretization of the open cavity domain is an unstructured mesh characterised by hexahedral elements. For a better distribution of the mesh elements, it is useful to introduce the Roberts stretching transformations, which cluster the elements near the cavity edges and increase the resolution near the singularities of the domain. There are three kinds of Roberts stretching transformations, whose implementation is described in detail in [33]. The preprocessor PRENEK of NEK5000 employs only the first one of these transformations and this is done introducing a ratio coefficient in the *ocavity.box* file as it is explained in the appendix A. After the mesh has been produced, the effective number of points used in computation depends on the degree of the polynomial bases. Since the distance between the lateral edges of the cavity and the boundary of the domain is kept constant irrespective of the aspect ratio of the cavity and since the resolution of the cavity is kept approximately unvaried, the number of the elements of the discretization grows with the aspect ratio. The number of elements, cells and points for the investigated aspect ratios is reported in table 3.1 considering spectral elements of the degree 6.

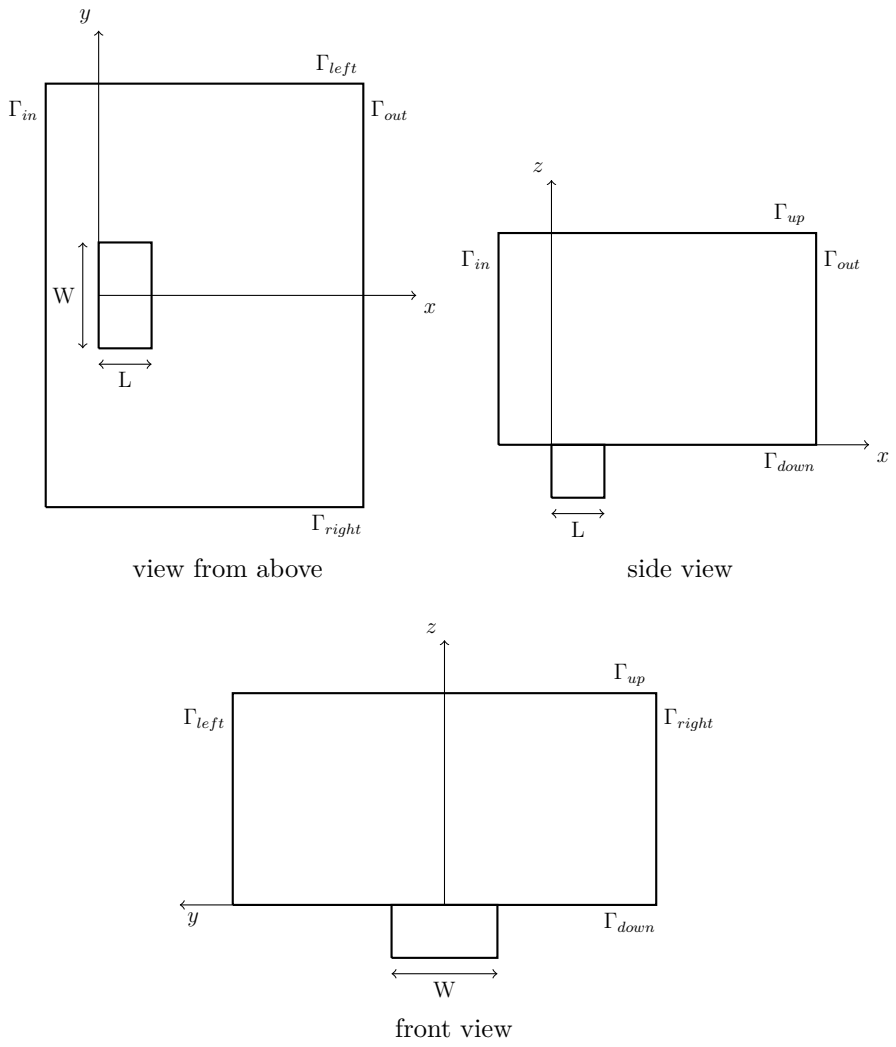

FIGURE 3.2. Orthographic projections of the open cavity domain.

Before the results are analysed, it is important to define the boundary conditions imposed to solve the base flow and the eigenvalue problem. Referring to figure 3.2 where the three orthogonal views of the open cavity are shown, the boundary conditions for each boundary surface are reported in the following.

- Γ_{in} (inflow boundary): for the base flow the inflow velocity is given by the Blasius profile, which is the solution of the boundary-layer Prandtl equations over a two-dimensional, semi-infinite plate held parallel to a uniform flow characterized by a velocity equal to U [26]. Since the plate is semi-infinite, the problem is not characterized by a reference

length and this suggests to assume that the x component of the velocity field is dependent on a unique and non-dimensional variable η called similarity variable and defined as

$$\eta = y\sqrt{\frac{U}{\nu x}} \tag{3.2}$$

which is, in its turn, dependent on the coordinate x and z. From this, it is possible to write the u component of the velocity field as

$$u = Uf'(\eta) \tag{3.3}$$

where $f(\eta)$ is an unknown function. The substitution into the Prandtl boundary-layer equation gives the Blasius equation

$$f'''(\eta) + \frac{1}{2}f(\eta)f''(\eta) = 0 \tag{3.4a}$$

$$f(0) = 0 \quad f'(0) = 0 \quad f'(\infty) = 1 \tag{3.4b}$$

where the boundary conditions are obtained from the ones imposed on $\mathbf{u}$, i.e. a no-slip condition on the plate and an asymptotic condition for $z \to \infty$. The solution to the Blasius equation is obtained numerically. Exploiting the definition of the similarity variable, the numerical solution is transformed as a function of x and z and is scaled on the cavity geometry through an interpolation on the grid nodes.

To compute the eigenvalues, a homogeneous Dirichlet condition is imposed. To summarize:

$$\mathbf{U} \Rightarrow \text{Blasius profile} \quad \text{for the base flow} \tag{3.5a}$$

$$\mathbf{u} = \mathbf{0} \quad \text{for the eigenvalue problem;} \tag{3.5b}$$

- Γ_{out} (outflow boundary): to compute the base flow the following outflow condition is imposed

$$\frac{\partial U}{\partial x} = 0 \quad \text{and} \quad P = 0 \tag{3.6}$$

while, for the eigenvalue problem, a homogeneous Dirichlet condition is imposed

$$\mathbf{u} = \mathbf{0}; \tag{3.7}$$

- on the lateral boundary Γ_{right} and Γ_{left} a symmetry condition is imposed

$$\frac{\partial U}{\partial y} = 0,\ V = 0,\ \frac{\partial W}{\partial z} = 0 \quad \text{for the base flow} \tag{3.8a}$$

$$\frac{\partial u}{\partial y} = 0,\ v = 0,\ \frac{\partial w}{\partial z} = 0 \quad \text{for the eigenvalue problem;} \tag{3.8b}$$

- Γ_{up} (upper boundary): outflow normal condition;
- Γ_{low} (lower boundary): this boundary represents the wall of the cavity and, therefore, a no-slip condition is imposed for both the base flow and the eigenvalue problem:

$$\mathbf{U} = \mathbf{0} \quad \text{for the base flow} \tag{3.9a}$$

$$\mathbf{u} = \mathbf{0} \quad \text{for the eigenvalue problem.} \tag{3.9b}$$

3.2 Aspect ratio 2 and 3

The base flow for both aspect ratios is computed for several Reynolds numbers in the range [2000, 7000] to investigate two types of instability that may characterize the dynamical system. The first kind of instability is a centrifugal instability which occurs at low Reynolds numbers and whose effects are particularly evident in the xy plane, where a series of counter-rotating vortices are observed. The appearance of the counter rotating vortices is surely related to an instability when a two dimensional flow is considered, while in the three dimensional case this is just a hypothesis. The second kind of instability is an unsteady instability which brakes the time invariance symmetry of the flow.

An indicator is needed to assess the convergence of the calculation of the base flow and, in this case, the $L^2(\Omega)$ norm of the velocity increment field normalized with respect to the time step dt is used. The iteration is stopped when the norm of the velocity increases between two successive steps falls below a predetermined value. By looking at this indicator, it is also possible to define if the solution has suffered an unsteady instability. In fact, the flow is stable if the oscillations of the indicator have the same order of magnitude of the precision adopted in NEK5000 to solve the system equations, while, if the oscillations are at least one order of magnitude greater than the machine epsilon, the flow is considered unstable. In particular, in this case, the period of the observed oscillations can be used to evaluate the frequency, and therefore the imaginary part, of the most unstable eigenvalue of the system.

3.2.1 Boundary layer

For open cavities flows it is important to characterise the boundary layer at the upstream edge of the cavity. As said in the first section of this chapter, the initial and boundary conditions for the velocity field imposed at the inflow boundary correspond to the velocity profile given by the Blasius solution to the Prandtl boundary-layer equations.

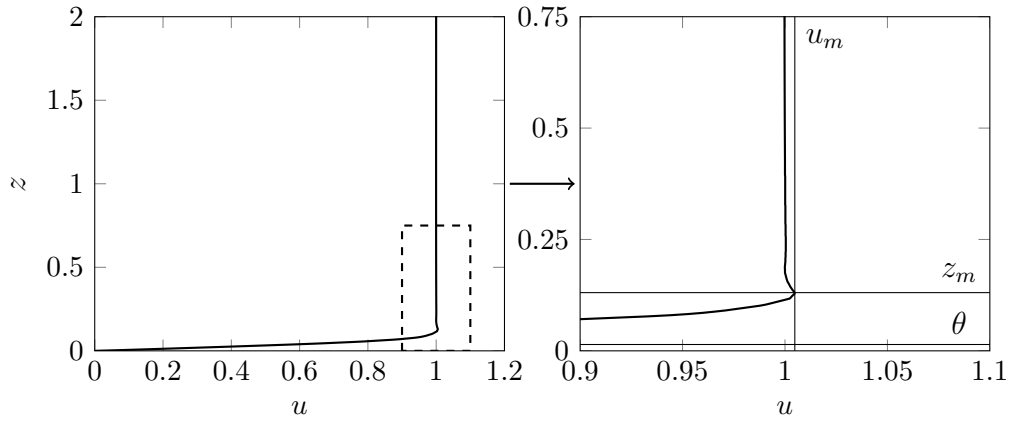

FIGURE 3.3. Velocity profile u plotted at the cavity upstream corner in the symmetry plane ($x = 0$, $y = 0$, $0 < z < 2$) for $Re = 6500$.

In figure 3.3, the x component of the velocity field is plotted versus z on the vertical line at the symmetry plane cavity upstream edge ($x = 0$, $y = 0$, $0 < z < 2$). The most important characteristic of the velocity profile is the slight velocity overshoot present at $z_m = 0.13067$, where $u = u_m = 1.0048$. This phenomenon can be explained considering that the slow downstream thickening of the boundary layer induces a velocity $w > 0$ in z direction. For example, in the case of Blasius boundary layer on a semi-infinite plate the induced transverse velocity is equal to $w = 0.86\sqrt{(\nu u/x)}$, which is a decreasing function of x. Considering that the external flow is irrotational, the out of plane vorticity, defined as

$$\omega_z = \frac{\partial w}{\partial x} - \frac{\partial u}{\partial z} \tag{3.10}$$

is null and, therefore, since the derivative of w in downstream direction is negative, the derivative of u in z direction has to be negative too, confirming in this way the maximum peak for the velocity.

For a more detailed characterization of the cavity boundary layer, the momentum thickness defined as

$$\theta = \int_0^\infty \frac{u(z)}{u_{ext}}\Big(1 - \frac{u(z)}{u_{ext}}\Big)dz, \tag{3.11}$$

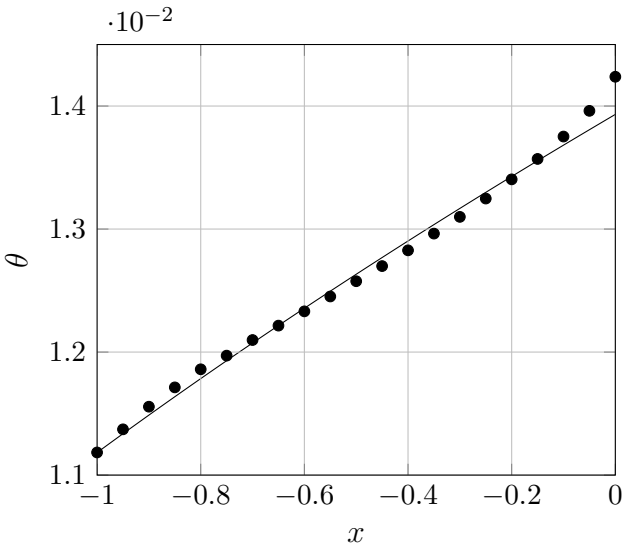

FIGURE 3.4. Boundary layer momentum thickness for $-1 < x < 0$ and $y = 0$ for $Re = 6500$ (•) and for the Blasius solution (——).

which is equal to 0.014238 at the upstream cavity corner (figure 3.3), is shown in figure 3.4 for $-1 < x < 1$ and $y = 0$ for the flow at $Re = 6500$. As a reference, the momentum thickness relative to the Blasius boundary layer solution is also plotted on the same figure. Since the Blasius solution is valid only for $Re \to \infty$, the numerical and the exact solutions does not correspond exactly, but since the two curves match reasonably well it is possible to conclude that the boundary layer in the numerical simulations has a behaviour similar to a Blasius boundary layer and, therefore, the inlet boundary condition is definitely reasonable and the incoming flow is laminar.

3.2.2 Flow morphology in the xz plane

Since most of the results available in the literature are about the two dimensional open cavity, it is natural to start the analysis of the base flow by looking at the xz symmetry plane. For all the Reynolds numbers studied in this thesis, the flow in this plane is characterized by a large scale vortex, which is usually called primary vortex (PV in figure 3.5). For both the cavities with $AR = 2$ and $AR = 3$, this vortex occupies the largest part of the xz symmetry plane and it is characterized by the higher velocity and the higher rotational kinetic energy respect to the other vortical structures observable in this plane inside the cavity. The presence of the primary vortex is in accordance with the numerical and the experimental results described in other works about the open cavity with a square cross-stream section, like the visualizations

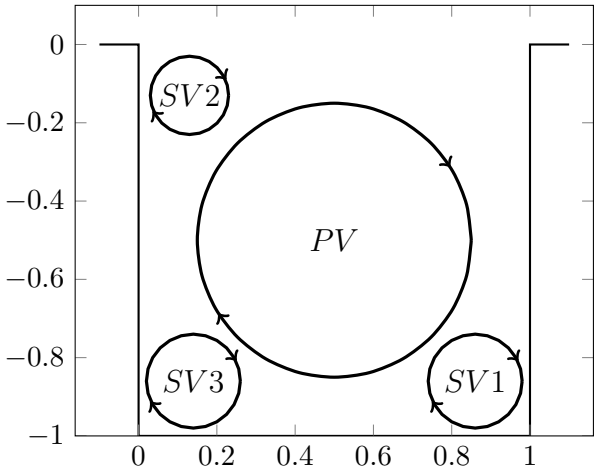

FIGURE 3.5. Schematic view of the vortical structures characterizing the symmetry plane of the cavity.

by Faure et al. [15] for the cavity with aspect ratio equal to 6, that are well comparable with the results obtained in this thesis.

It is interesting to note that the flow inside the primary vortex behaves like a rotating solid. This can be observed looking at the figure 3.6 where the velocity profiles along the centrelines of the cavity symmetry plane are shown for $Re = 3000$ and $Re = 6500$. On the horizontal centreline ($0 < x < 1$, $y = 0$, $z = -0.5$) the vertical component of the velocity field w is plotted versus x and two regions with different behaviours can be highlighted: the first one, which develops near the cavity walls, is a boundary layer region while in the second one w varies approximately linearly with x and, therefore, a solid body rotation is observed. On the vertical centreline ($x = 0.5$, $y = 0$, $-1 < z < 4$) the horizontal component u of the velocity field is plotted versus z. In this case, starting form the bottom of the cavity, it is possible to recognise a boundary layer region, a rigid body rotation in the central region, a shear layer characterized by a strong velocity gradient just at the top border of the cavity and, finally, a uniform flow outside the cavity.

Always looking at the symmetry plane, it is possible to identify three other rotational structures, usually called secondary vortices, whose presence is strongly dependent on the Reynolds number of the flow. The first one is the counter-rotating vortex SV1. As it is shown in figure 3.5, this vortex is placed in the downstream bottom angle of the cavity and, for both aspect ratios, its dimension in the x direction decreases when the Reynolds number is increased, while its extension in the z direction increases with the Reynolds number. The second counter-rotating vortex, denoted SV2, is a small scale secondary

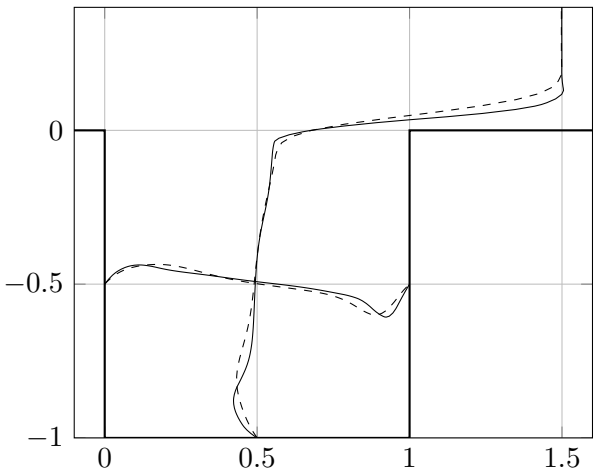

FIGURE 3.6. Streamwise and vertical velocity profiles in the cavity symmetry plane for $Re = 3000$ (- - -) and $Re = 6500$ (——)

vortex which appears for quite high Reynolds numbers. For example, for the case of $AR = 2$, the Reynolds number for which this structure first appears is approximately 6750. The presence of this vortex is probably due to the fact that an increase of the Reynolds number, namely a reduction of the the viscous effects, entails a decrease of the capability of the primary vortex to drag the fluid particles near the cavity walls. The weaker intense dragging effect leads to more extended separation and counter-rotating regions. Finally, another secondary structure can be observed in the symmetry plane: the counter-rotating vortex SV3 in the up-stream bottom angle of the cavity. This vortex is quite similar to SV1 but is usually characterized by lower velocities.

Figure 3.7 shows the possible morphological configurations which are identified in the xz symmetry plane for the different Reynolds numbers analysed. In particular, three different groups can be recognised :

- the first group is characterized by the primary vortex PV and by the two secondary vortices SV1 and SV3. For $AR = 2$ this configuration is found for Reynolds lower than 3100 while, for $AR = 3$ for Reynolds lower than 3000;

- the second group is characterized by the presence of the primary vortex VP and just one vortex, SV1. For $AR = 2$ this morphology is found for Reynolds number in the range between 3200 and 6500, while, for $AR = 3$, it is found for Reynolds between 4000 and 6375;

- the third group presents the secondary vortex SV2, in addition to the primary vortex VP. This configuration, for $AR = 2$, is observed for

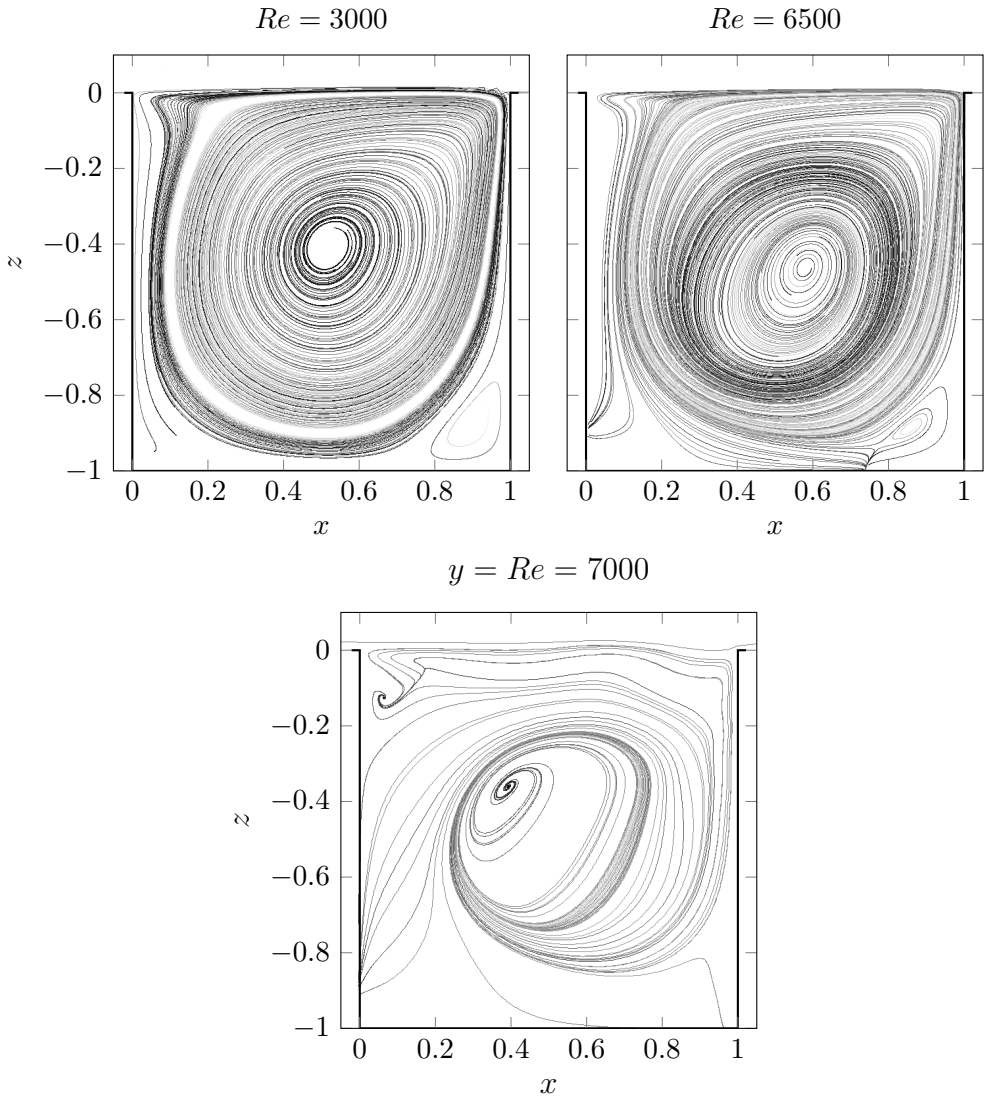

FIGURE 3.7. Flow behaviour in the $y = 0$ planes for $Re = 3000$, $Re = 6500$ and $Re = 7000$.

Reynolds numbers higher than 6750 and, for $AR = 3$, for Reynolds numbers higher than 6500, for which, as we will see, the flow is characterized by an unsteady instability. As observed for the vortex SV3 in the first group, also in this case the size of the secondary vortex SV2 increases as the Reynolds number is increased.

The presence of different morphological configurations of the vortical structures in the symmetry plane can be explained remembering that the studied geometry is three-dimensional owing to the important influence of

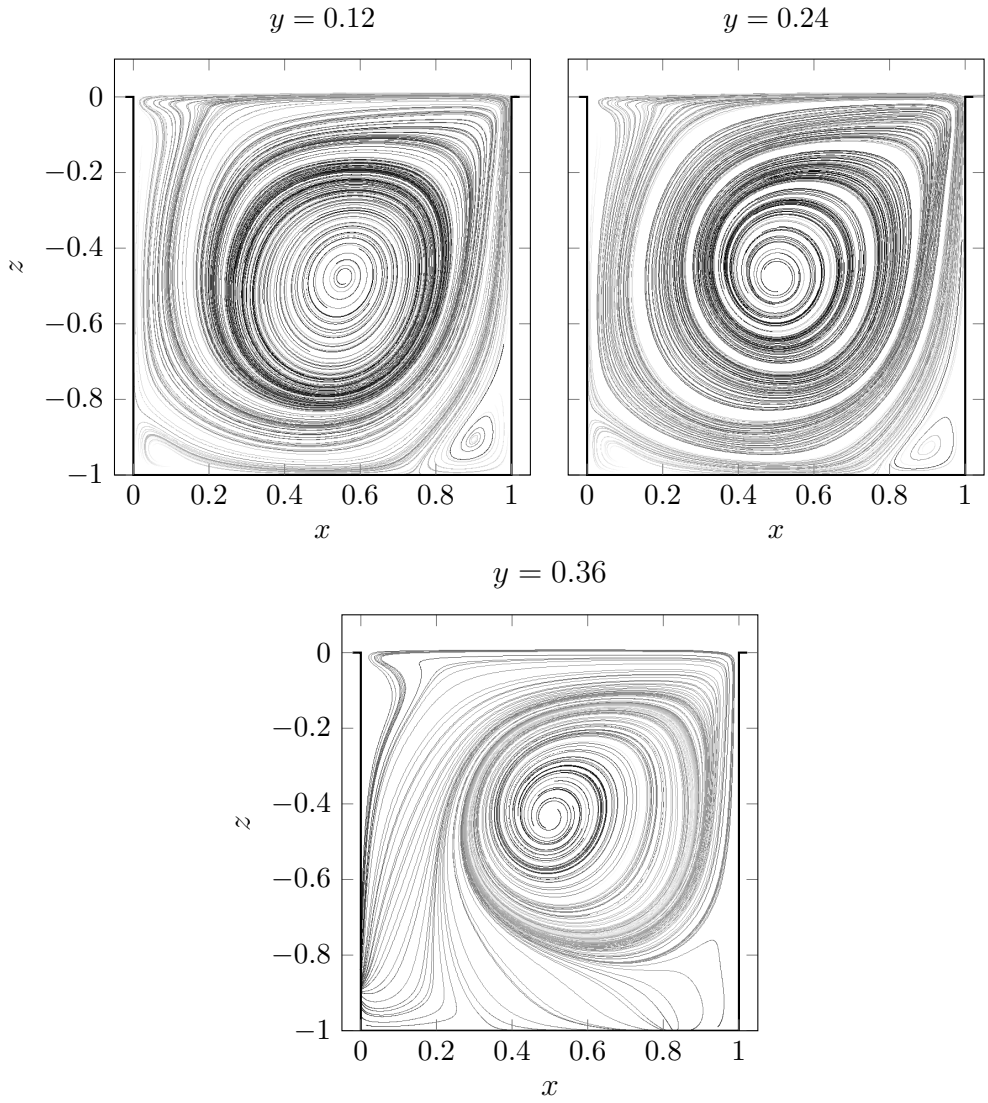

FIGURE 3.8. Flow behaviour in the $y = \text{const.}$ planes for $Re = 6500$ for different values of the y coordinate.

the lateral walls of the cavity, which modify the morphology of the flow. Moreover, the instabilities, if present, could have an important influence on the behaviour of the flow with respect to the two-dimensional case. In order to understand how the three-dimensionality of the domain influences the flow inside the cavity, it is useful to observe the flow field on the $y = \text{const.}$ planes for different values of the y coordinate.

In the case of $Re = 3000$, the flow morphology is the same in all the planes with a gradual decrease of the size of the two secondary vortices caused by the

effect of the no-slip condition imposed on the cavity lateral walls. Figure 3.8 shows the views of the $y = \text{const.}$ planes for y equal to 0.1, 0.35, 0.5 and 0.75 for $Re = 6500$. In this case it is possible to notice that the flow passes through different morphological conditions as the y coordinate is varied. In particular, between $y = 0$ and $y = 0.36$ two different morphologies are present, which can be found also for greater values of y. The reason for this behaviour is that the flow is characterized by the appearance of three-dimensional vortical structures visible in the xy and yz planes, which are not present for lower Reynolds numbers. The same behaviour can be observed also for $Re = 7000$.

3.2.3 The appearance of longitudinal vortices

In order to understand the variation of the flow morphology along the y axes, it is necessary to explore not only the $y = \text{const.}$ planes previously analysed, but also the $z = \text{const.}$ and $x = \text{const.}$ planes. Only in this way it is possible to understand the effects of the three-dimensionality of the domain and appreciate how the presence of vortical structures influences the behaviour of the flow.

Starting the analysis of the morphology of the flow in the xy plane, three different behaviours are observed as the Reynolds number is varied. For low Reynolds numbers, the flow is characterized by large three-dimensional vortical structures that are generated by the three-dimensionality of the geometry and which occupy all the cavity. In these conditions no longitudinal vortex structures are present. When the Reynolds number thresholds $Re = 3200$ for $AR = 2$ and $Re = 4000$ for $AR = 3$ are exceeded, it is possible to observe the appearance of spanwise rows of longitudinal vortices on both the upstream and the downstream walls of the cavity, which seem to imply the appearance of an instability for the flow. In particular, this seems to be a steady and three-dimensional centrifugal instability substantially independent on the Mach number, analogous to the one reported in the paper of Bres and Colonius [5]. In the last case, for a Reynolds number greater than 6750 for $AR = 2$ and 6500 for $AR = 3$ well defined patterns are no longer observable and the flow is characterized by one isolated pair of counter-rotating vortices departing from the cavity upstream wall.

The first behaviour previously described is observed, for the cavity with aspect ratio 2, for Reynolds numbers from 2000 to 3100. In figure 3.9 the velocity streamlines in the $z = -0.5$ plane for $Re = 3000$ are shown. Looking at the figure it is possible to notice the large scale vortical structures previously described, that are similar to those observed in the visualizations by Faure et al. [16]. These large scale vortices develop near the lateral edges of the cavity and are originated by the presence of the lateral walls where a no-slip

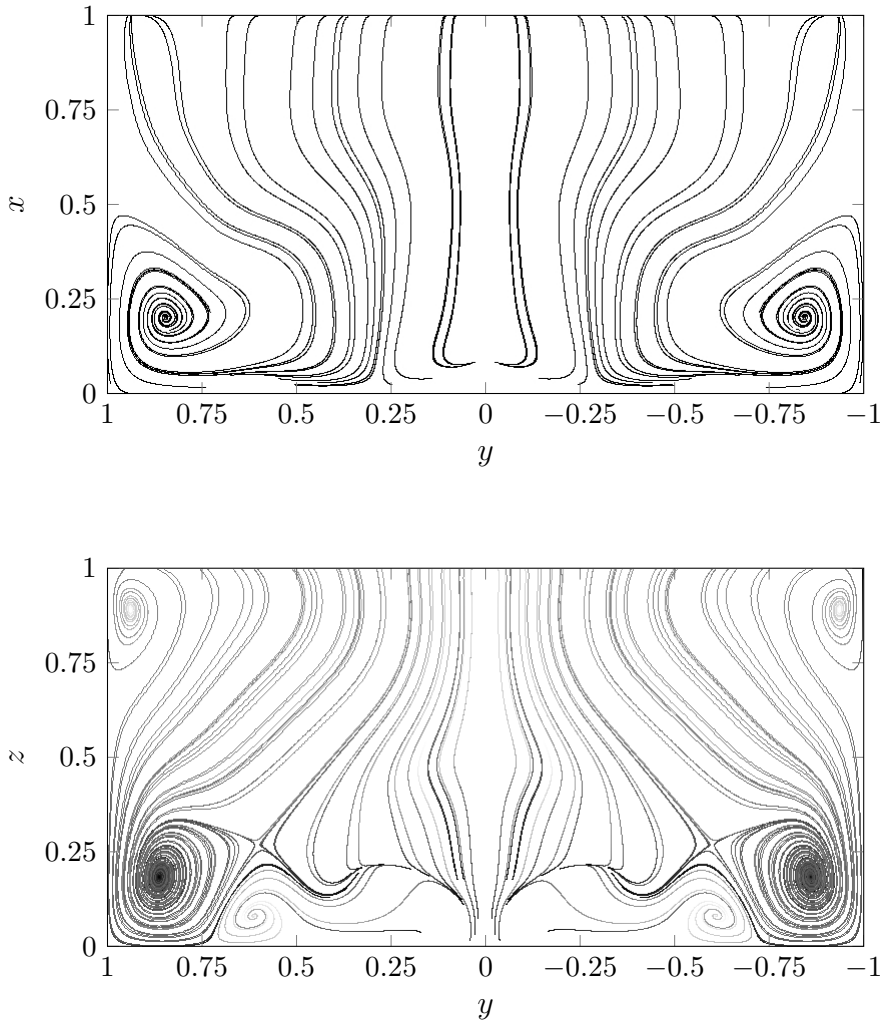

FIGURE 3.9. Representation of the streamlines of the velocity component in the plane at $z = -0.5$ (top) and in the plane at $x = 0.5$ (bottom) for $Re = 3000$.

condition is imposed. The direct consequence of this behaviour can be found remembering that the morphology of the flow remains approximately constant in the spanwise direction, but for a slight variation of the centre of the main vortex and of the the size of the secondary vortices. The streamlines of the velocity component in the yz plane for $Re = 3000$ (figure 3.9) show that, also in this case, the only vortical structures that characterize the flow in this plane are the corner vortices caused by the interaction between the flow and the lateral boundary of the domain where a no-slip condition is imposed. In

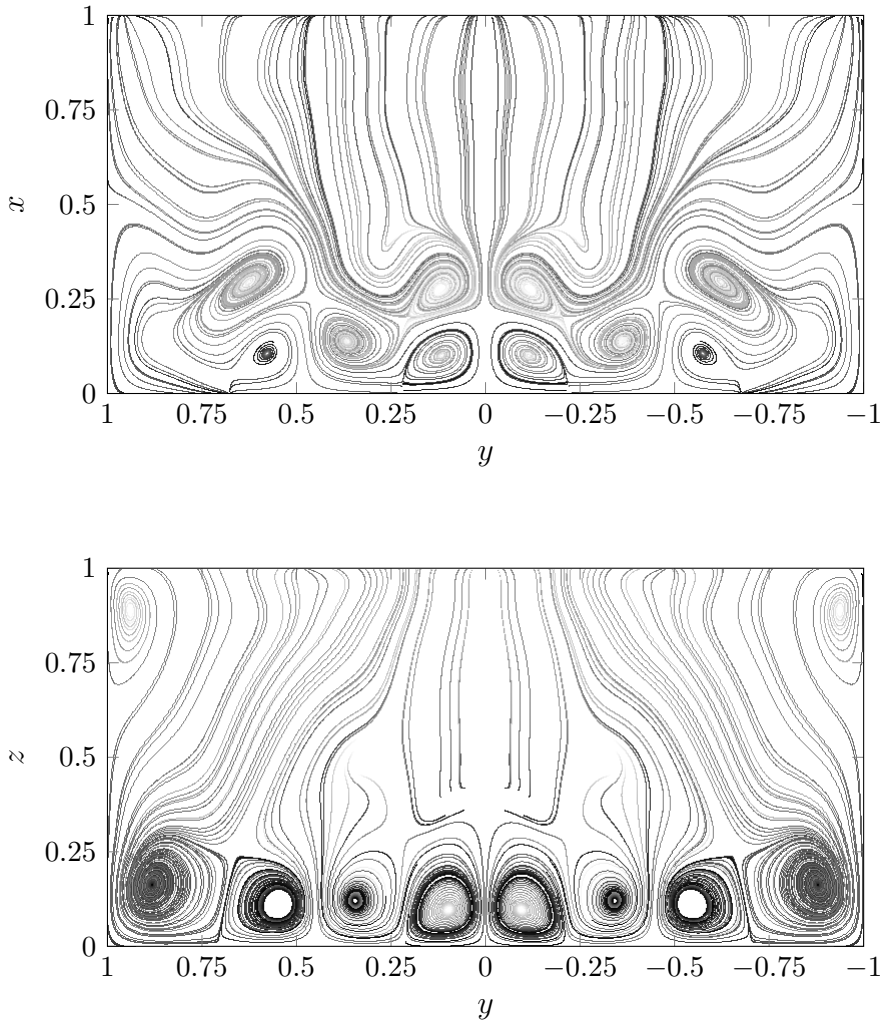

FIGURE 3.10. Representation of the streamlines of the velocity component in the plane at $z = -0.5$ (top) and in the plane at $x = 0.5$ (bottom) for $Re = 5000$.

fact, near each one of the two bottom angles of the cavity, we can observe the presence of a large scale vortex associated with another small scale and counter-rotating vortex. All these structures are visible approximately in the range $0.5 < x < 0.7$, which is the range of the x coordinate where the effects of the upstream and downstream walls are less intense.

The second behaviour observed, i.e. the development of well defined patterns of spanwise rows of longitudinal vortices, is, instead, characteristic of Reynolds numbers in the range $3200 <= Re <= 6500$. These vortices are

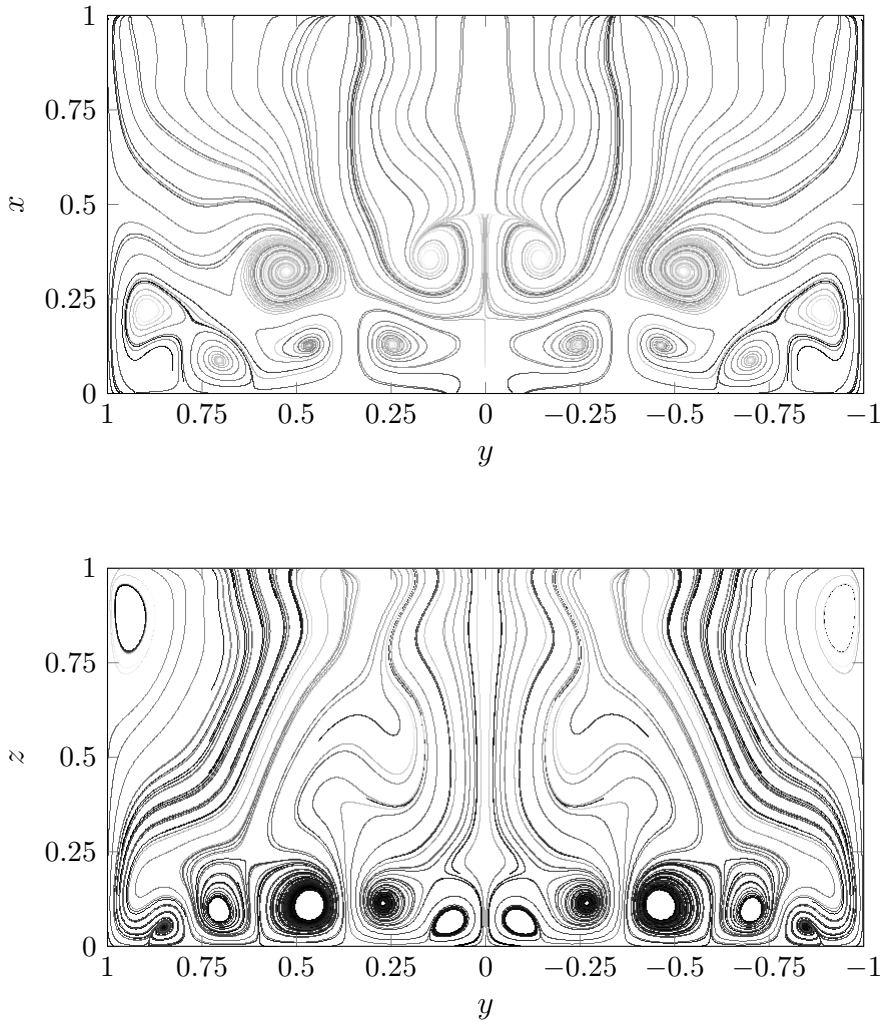

FIGURE 3.11. Representation of the streamlines of the velocity component in the plane at $z = -0.5$ (top) and in the plane at $x = 0.5$ (bottom) for $Re = 6500$.

probably originated by the centrifugal effect in the shear layer produced by the main vortex, which is more intense as the Reynolds number is increased. To appreciate this phenomenon the streamlines associated with the velocity component in the plane $z = -0.5$ are shown in figure 3.10 and 3.11 for Reynolds numbers equal to 5000 and 6500, respectively. The first aspect to be noticed from these figures is that the dimension of the longitudinal vortices is not constant in y direction. In fact, starting from the centre of the cavity and approaching the cavity walls, where the three-dimensional effects are

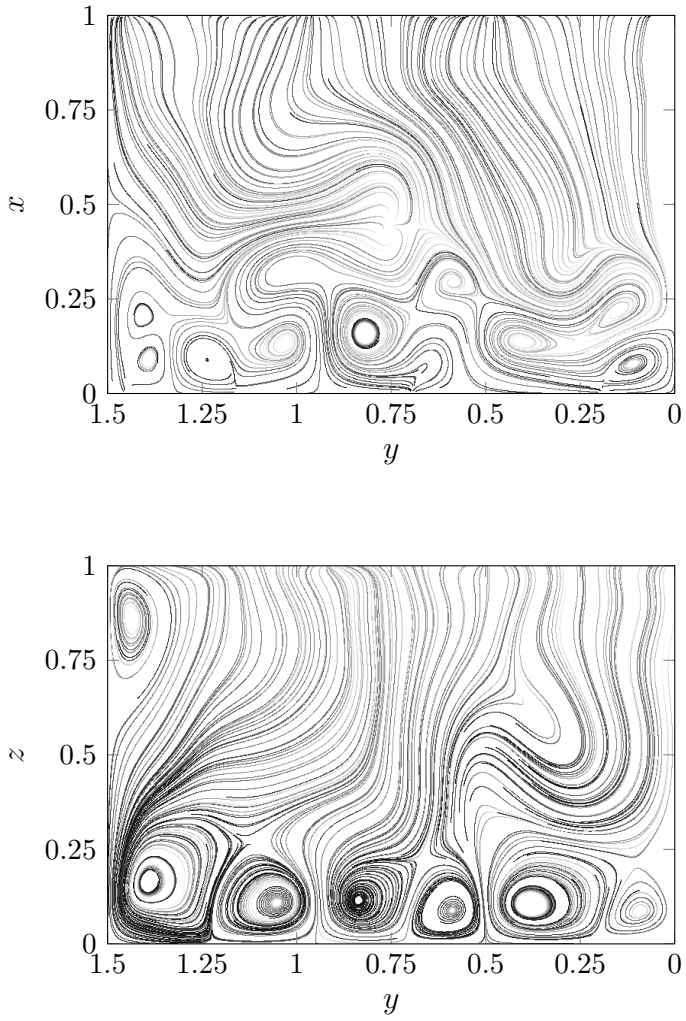

FIGURE 3.12. Representation of the xy plane at $z = -0.5$ and the yz plane at $x = 0.5$ of the open cavity with $AR = 3$ for Reynolds number 6250. Since the solution is symmetrical, only the planes for $y > 0$ are shown.

more intense because of the no-slip condition, the size of the counter-rotating vortices decreases.

As the Reynolds number is increased the number of longitudinal vortices increases due to the more intense effects of the centrifugal force. This behaviour can be appreciated comparing figure 3.10 and 3.11. For both Reynolds numbers, two rows of counter-rotating vortices are visible in the plane $z = -0.5$: for $Re = 5000$ (figure 3.10) the first one is characterized by

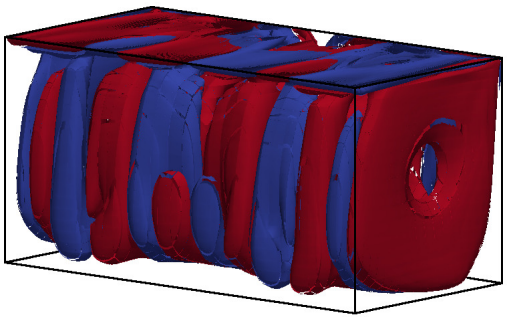

FIGURE 3.13. Helicity field for $Re = 6500$ in the cavity with $AR = 2$.

three vortex pairs and the second one, which develops for larger values of the x coordinate, by only one pair, while for $Re = 6500$ (figure 3.11) the first one is characterized by four vortex pairs and the second one by two vortex pairs.

From a further comparison of the flow at $Re = 6500$ with the flow at $Re = 6000$ (not shown in this thesis), it is evident that if the Reynolds number increases the vortical structures tend to compress in x direction and, at the same time, to elongate in spanwise direction. This changing of morphology was observed by Faure *et al.* [15] in their experimental paper on the cavity with aspect ratio 6 where they underlined the deformation of the vortical structures as the Reynolds number is increased.

The streamlines of the velocity component in the plane $x = 0.5$ are reported for $Re = 5000$ and $Re = 6500$ in 3.10 and 3.11, respectively. The vortex structures that can be observed in this plane are in accordance with the structures present in the xy plane. In particular, the flow at $Re = 5000$ is characterised by one row with three counter-rotating vortex pairs, while the flow at $Re = 6500$ is characterised by one row with four counter-rotating pairs of vortices. In figure 3.12, the velocity streamlines in the planes at $z = -0.5$ and $x = 0.5$ of the cavity with $AR = 3$ are shown for Reynolds number 6250. Also in this case, the longitudinal vortices are clearly visible in both planes and, by a comparison with the cavity with $AR = 2$, it is evident that an increase of the spanwise dimension of the cavity leads to an increased number of counter-rotating vortices. In particular, looking at the $x = 0.5$ plane, it is possible to recognise twelve longitudinal vortex, two more than in the cavity with $AR = 2$ for $Re = 6500$. The annular shape of these vortical structures is highlighted by figure 3.13 where the positive and negative contour surfaces of the helicity field $h = \mathbf{u} \cdot (\nabla \times \mathbf{u}) = \pm 0.1$ for the flow at $Re = 6500$ in the cavity with aspect ratio 2 are plotted.

The vortices previously described can be classified as Görtler vortices. These vortical structures are typical of flows characterized by a Taylor-Görtler

instability, which is a centrifugal and steady boundary-layer instability that develops near walls that are concave in the direction of the free-stream flow, such as in the Taylor–Couette flow, and which leads to the formation of counter-rotating, streamwise oriented vortices. In an inviscid flow, a useful tool to investigate if the flow is prone to a centrifugal instability is the Rayleigh discriminant, that is strongly dependent on the velocity gradient in wall-normal direction. In particular, the region of potential instability for the flow is where the velocity decreases as the wall is approached. Considering the open cavity problem, the curvature is no longer imposed by the boundary geometry, but is caused by the presence of the primary vortex VP and of the secondary vortices. Looking at the velocity profiles, reported in figure 3.6, the core of this vortex behaves like a rotating solid and the velocity increases linearly with the distance from the centre of rotation. At the same time, the presence of the walls, where a no-slip condition is imposed, causes a rapid decrease of the flow velocity near the boundary and, since the speed decreases as the distance from the centre of curvature is increased, the velocity profile may cause a centrifugal instability.

Sipp and Jacquin [31] have proposed in their work a sufficient condition for centrifugal instability in the inviscid limit.

Theorem 1 (Rayleigh discriminant) *The flow is unstable if, for each point r_0 along a generic streamline ψ_0, the Rayleigh discriminant defined as*

$$\Delta(r_0) = \frac{2\Omega}{\mathcal{R}(r_0)} \tag{3.12}$$

is negative.

■

In the previous formula $|\mathbf{u}|$ is the velocity magnitude, Ω is the y component of the vorticity field and $\mathcal{R}$ is the local radius of curvature defined as

$$\mathcal{R} = \frac{\mathbf{u}^3}{(\nabla\psi)\cdot[\mathbf{u}\cdot\nabla\mathbf{u}]}. \tag{3.13}$$

Thanks to the Rayleigh discriminant, Bres and Colonius [5] have concluded that the presence of longitudinal vortices in their studies about the three-dimensional instability of a two-dimensional mean flow is due to a centrifugal instability. In particular, they have underlined the important effects of the cavity upstream and downstream walls in the appearance of the vortex pairs obtaining a good agreement with the results of Faure et al [15]. However, in the geometry studied by Bres and Colonius [5], which has not lateral

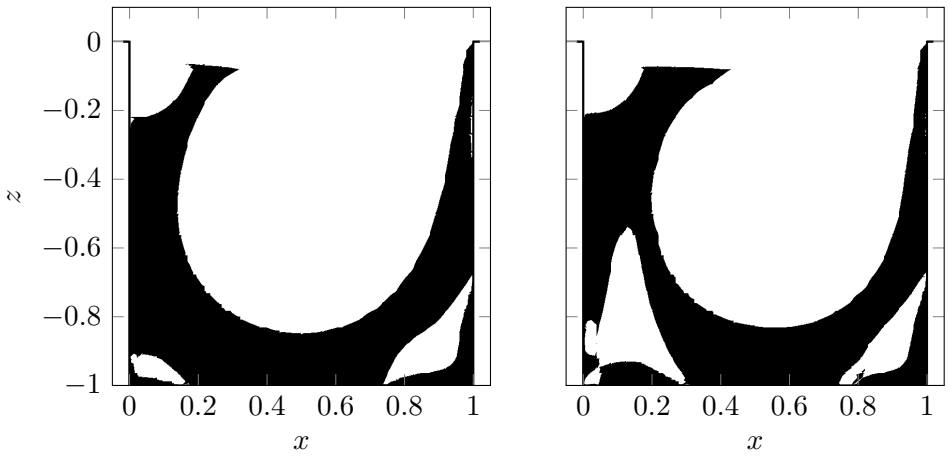

FIGURE 3.14. Rayleigh discriminant calculated in the xz symmetry plane for $Re = 3000$ (left) and $Re = 4000$ (right). The white region correspond to positive values and the black region correspond to negative values of the discriminant.

walls and, therefore, is characterized by translational spanwise symmetry, the presence of a centrifugal instability that causes a clear variation of the flow behaviour thorough a pitchfork bifurcation has sense, as in the perfect tip loaded beam.

Also in the the problem studied in this thesis, the cavity upstream and downstream walls play a fundamental role in the appearance of the centrifugal forces and, consequently, of the longitudinal vortices. In particular, applying the Rayleigh criterion on the cavity symmetry plane for $Re = 3000$ and $Re = 4000$, it is evident that for higher Reynolds numbers the region of potential instability is larger than for lower Reynolds numbers, where the viscous effects are predominant in respect to the centrifugal forces. Also if this behaviour is comparable to the one described by Bres and Colonius it is important to consider that in the current geometry the presence of the lateral walls breaks the translational spanwise symmetry. Hence, the behaviour of the system is analogous to an imperfect, rather than a perfect, tip loaded beam and, therefore, the system is no longer characterized by a pitchfork bifurcation, but by a progressive change of the solution as the Reynolds number is increased. This behaviour can be deduced by the figure 3.15, that shows the velocity streamlines in the $z = 0.51$ plane at five different Reynolds numbers closed to the appearance of the longitudinal vortices. If the flow was characterized by a centrifugal instability a sharp variation of the flow behaviour was expected, but, as is evident from the figure, the variation of the flow behaviour is gradual from a no vortex condition to a status characterized

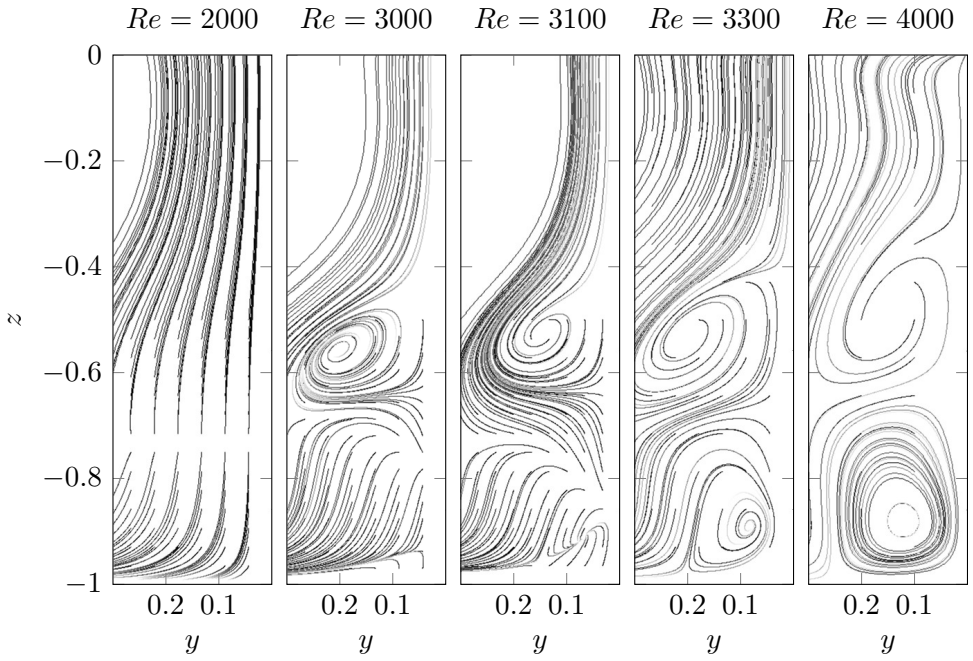

FIGURE 3.15. Velocity streamlines at $x = 0.51$ for five different Reynolds numbers.

by increasingly dimension longitudinal vortex.

In the previous paragraph, looking at the figure 3.8, the change of morphological configurations varying the y coordinate was highlighted. It is interesting to link this modification of the secondary structures to the flow morphology in the xy and yz planes, where for $Re = 5000$ and $Re = 6500$ span-wise rows of vortices are observed. Specifically, it is possible to notice that approaching the y coordinates that separate two consecutive counter-rotating vortices in spanwise direction, there is a variation of the flow morphology in the xz plane. So, the modification of the configuration of vortical structures in the xz plane can be ultimately connected to the formation of the counter-rotating spanwise vortices in the xy and yz planes and to the centrifugal forces.

3.3 Unsteady flow

In general, an increase of the Reynolds number causes the progressive destabilization of the flow that leads to transition and turbulence. In the previous section the three-dimensional centrifugal instability was investigated, while in the following the principal aspects of the unsteady instability of the flow over an open cavity with $AR = 2$ will be discussed.

It turns out that the flow over the open cavity with aspect ratio equal to

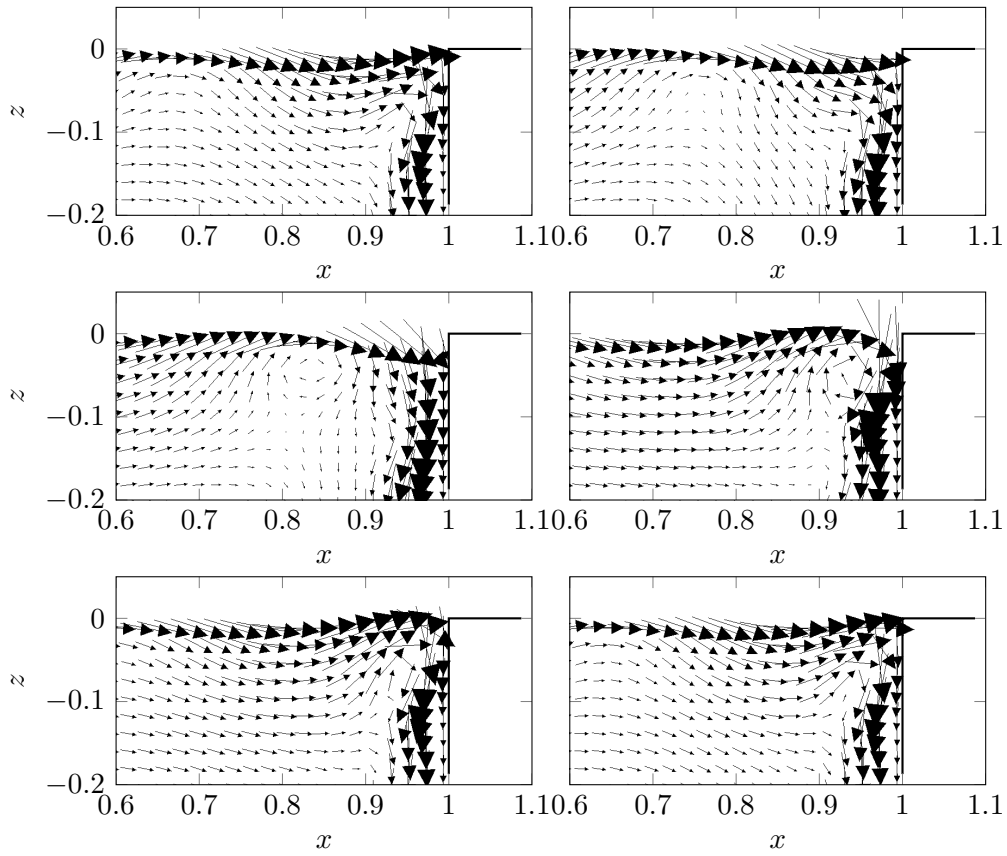

FIGURE 3.16. Velocity vector field in the $y = 0.25$ plane plotted in six different times of the fluctuation period.

2 shows an unsteady behaviour for Reynolds number greater than 6750. The reason of the unsteadiness can be linked to the instability of the shear layer between the slower flow inside the cavity and the faster flow outside of it, through a Kelvin-Helmholtz mechanism. The Kelvin-Helmholtz instability is related to the appearance of a vortex which, for Reynolds numbers not very high, detaches periodically from the upstream corner of the cavity and interacts with the downstream edge (figure 3.16).

To investigate the properties of the unsteady instability, the time history of the vertical component of the velocity field sampled in four points situated at $z = 0$ and $x_1 = 0.25$, $x_2 = 0.5$, $x_3 = 0.75$ and $x_4 = 0.9$ in the symmetry plane is shown in figure 3.17. Starting from the first station situated just downstream of the upstream corner, the vertical component w of the velocity shows a time-periodic behaviour. This means that, in these conditions, the flow starts to oscillate regularly. The frequency of the oscillation can be

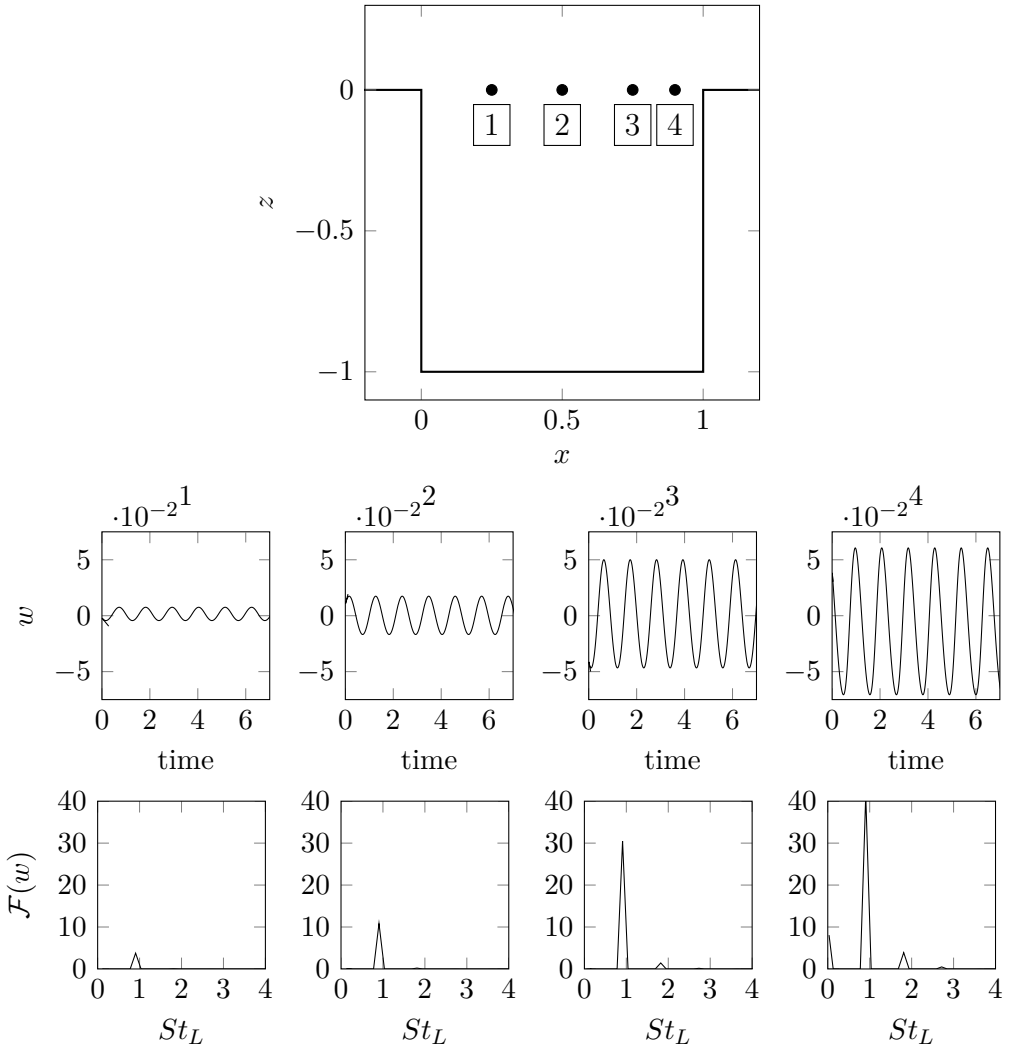

FIGURE 3.17. Time variation and power spectra of the vertical component of the velocity field measured in the four stations indicated in the cavity sketch for the flow over an open cavity with $AR = 2$ and $Re = 7000$.

computed by a Fourier transform of the velocity signal $w(t)$ obtaining a frequency corresponding to a Strouhal number based on the cavity length of $St = fL/U = 0.905$. In the three successive stations the oscillation amplitude progressively increases with an amplification factor between the first and the

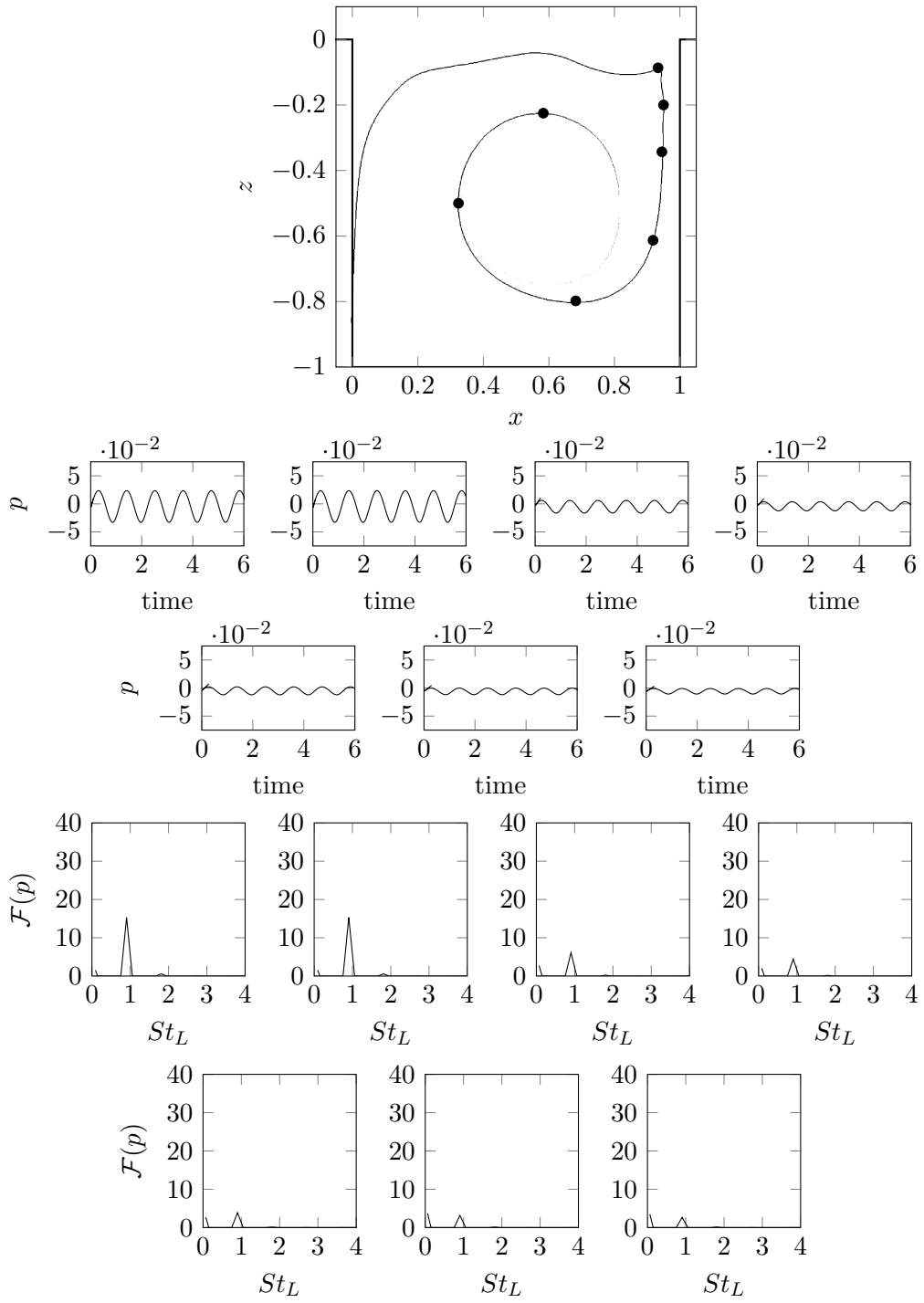

FIGURE 3.18. Time variation and power spectra of the pressure field measured in seven stations along the streamline passing at $x = 0.95$, $y = 0$ and $z = -0.2$ for the flow at $Re = 7000$.

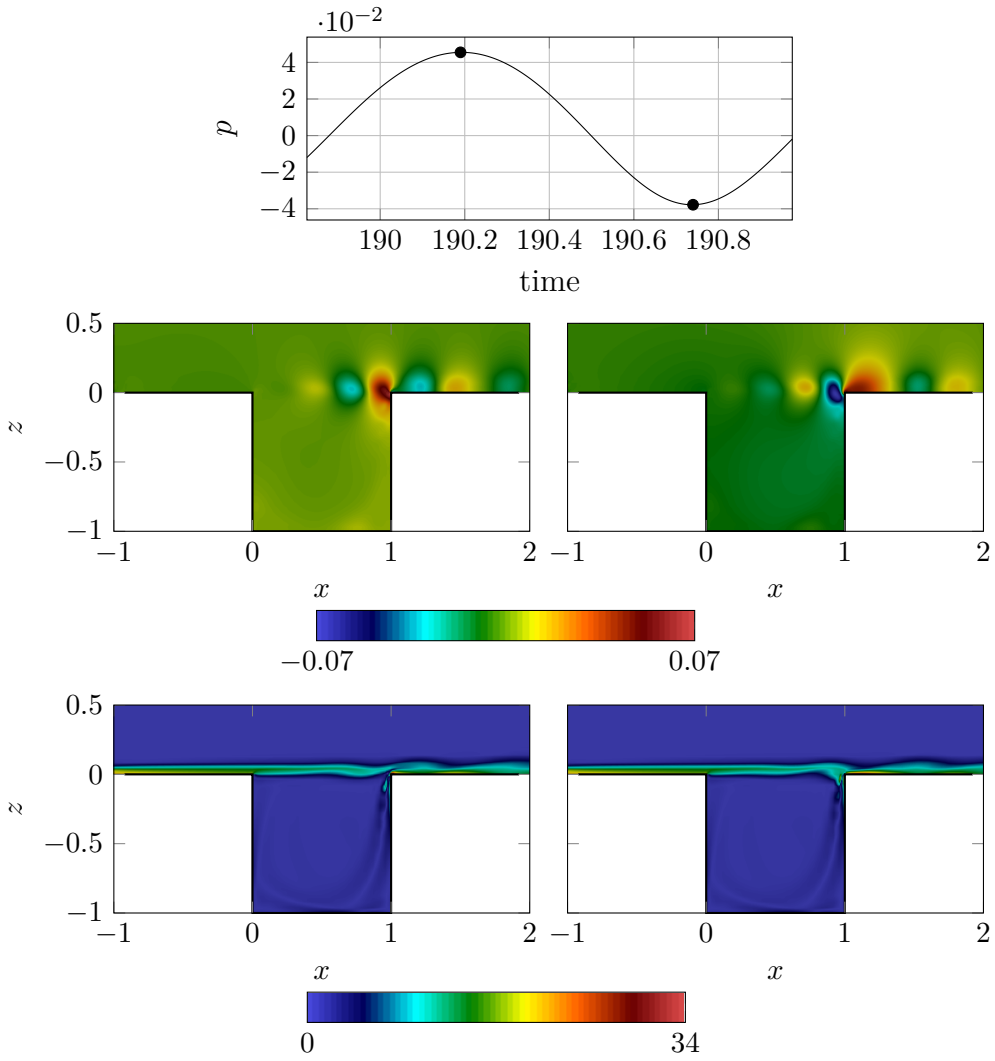

FIGURE 3.19. Pressure time history at the cavity downstream edge (top), pressure field (middle) and out of plane vorticity (bottom) measured at $y = 0.25$ plane for the flow at $Re = 7000$. The left column is relative to the maximum of pressure while the right column is relative to the minimum of pressure.

last station approximately equal to 8. This trend is also observable from the spectra of $w(t)$ which is characterized by a progressively increase of the energy associated to the main oscillation frequency. Starting from the station 3, but more visible in the last station, a secondary less energetic contribution due to the non-linearity is observable for a dimensionless frequency of $St = 1.81$.

The unsteady behaviour of the flow in these conditions is also examined

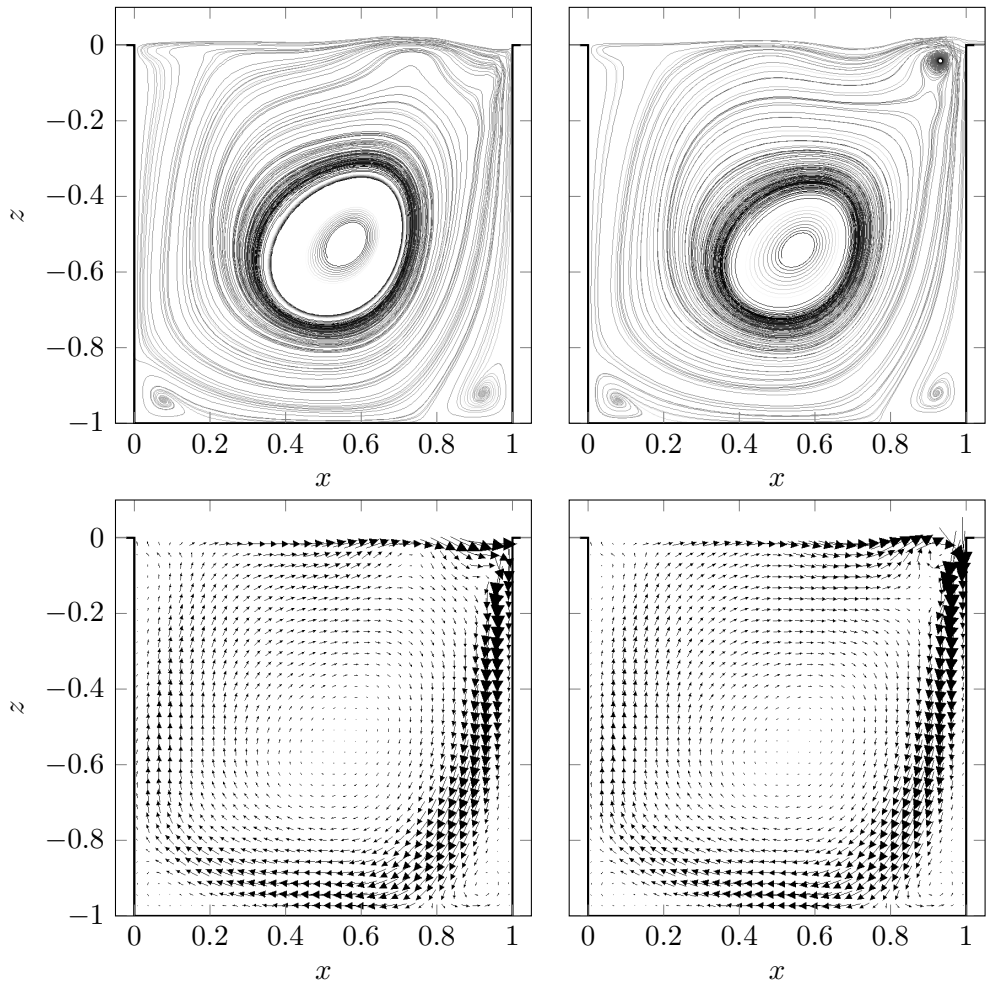

FIGURE 3.20. As in the previous figure but velocity streamlines (top) and velocity vector (bottom).

along one of the most external streamline, which passes at $x = 0.95$ and $z = -0.2$ of the cavity symmetry plane. Also in this case, as is shown in figure 3.18, the main frequency of the oscillation corresponds to a Strouhal number of $St = 0.905$ and, starting from the most external point of the streamline and approaching the rotation centre of the primary vortex, the amplitude of the pressure oscillations decreases. However, it is interesting to note that along the streamline the phase shift measured in the various station in essentially null.

For a more detailed analysis of the flow characteristics in unsteady conditions, in figure 3.19 the pressure field and the vorticity magnitude field and in figure 3.20 the streamlines and the vector field in the $y = 0.25$ plane are

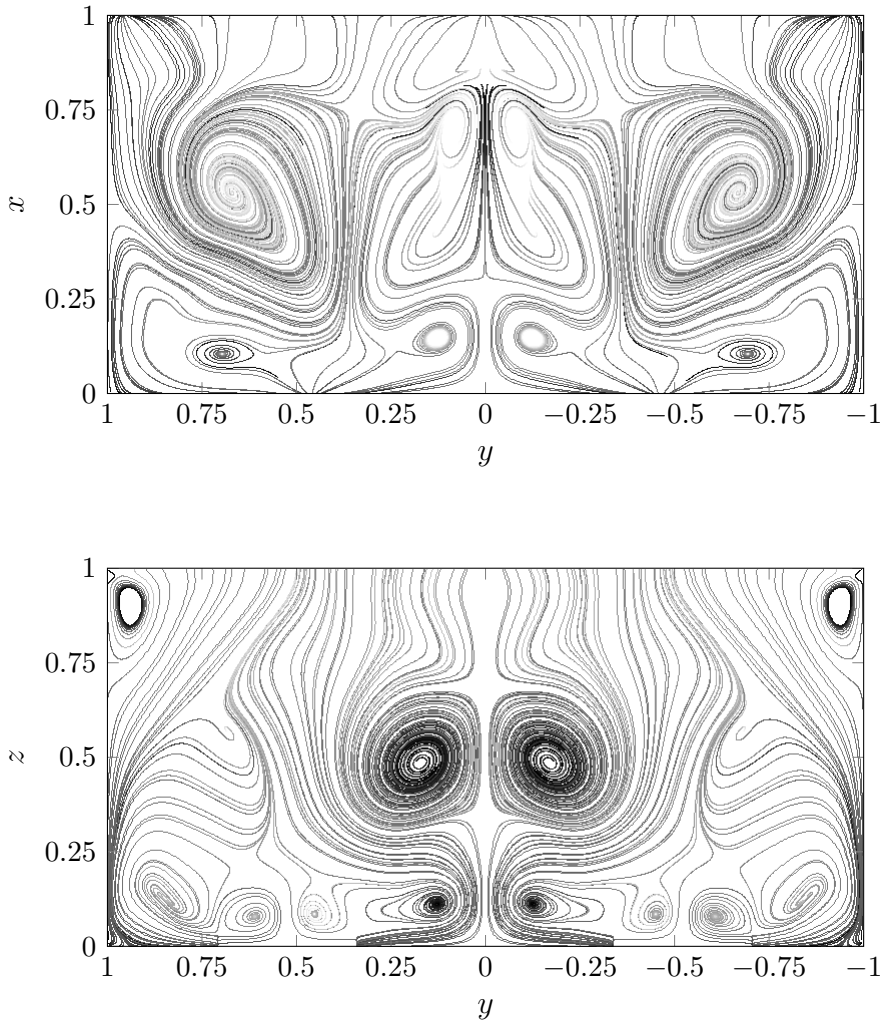

FIGURE 3.21. Representation of the xy plane at $z = -0.5$ and the yz plane at $x = 0.5$ of the open cavity for Reynolds number 7000.

plotted for the solution phases corresponding to a minimum and a maximum in the pressure value measured at the downstream edge of the cavity. The spectral analysis of the pressure time history plotted in this figure has a period and a fundamental frequency well comparable with the ones of the vertical velocity signal measured in the above-mentioned four stations.

First of all, differently from what happens in a steady flow where a stagnation point at the downstream cavity corner was observed, if the flow is unsteady the pressure field is characterised by large-scale pressure fluctuations created by the interaction between the oscillating shear layer and the

downstream edge, which propagate past the cavity. Since the flow remains laminar also in these unsteady conditions, the interaction previously introduced is fairly regular and, in particular, the minimum value for the pressure is measured when the Kelvin-Helmholtz vortex, inside of which the pressure is low, hits the cavity downstream edge. This behaviour is well observable from the velocity streamlines plotted at the minimum of the pressure. An important influence on the behaviour of the flow is given by the cavity downstream corner, whose effects were studied for the first time by Rockwell and Knisely [22] whose observations are quite relevant for the present work. In particular, when the Kelvin-Helmholtz vortex impacts on the cavity trailing edge it is divided in two parts: the first one is transported inside the cavity while the second one is convected in the channel.

The maximum of pressure is, instead, reached about half period later when the Kelvin-Helmholtz vortex is not already created, as one can see from the velocity streamlines associated to the pressure maximum. In fact, looking at the flow evolution during a pressure cycle (figure 3.16), the instability vortex is not always present past the cavity leading edge, but it develops approximately at $x = 0.75$ shortly after the maximum peak for the pressure at the downstream edge. Furthermore, since the cavity is not very long, two successive vortices at the interface between the cavity and the channel are never observed.

Finally, it is important to observe the morphology of the flow in the xy and yz planes. Differently from the flows at $Re = 5000$ and $Re = 6500$, where well organised spanwise rows of vortices are present, for these Reynolds numbers the morphology is characterized by one symmetrical large-scale pair of counter-rotating vortices departing from the upstream cavity wall, which are produced by the centrifugal forces, but that evolves in coherent large-scale and not stable structures (figure 3.21). Hence, it is possible to conclude that in these conditions the effects of the centrifugal force are definitely reduced.

4 | Cavity with $AR = 1$

This chapter focuses on the stability analysis which, in this thesis, is performed only for the three-dimensional cuboid open cavity for $Re = 7000$. The justifications to this only one analysis can be found in the appendix where the principal computational aspects about a stability study are briefly introduced.

4.1 Comparison with lid-driven cavity flow

The behaviour of the flow inside a lid-driven cavity is a problem largely studied and a lot of experimental and numerical results can be found in the literature. Among these results, a few concerns the stability analysis of the three-dimensional flow. Considering the case with $AR = 1$, it is possible to compare the results about the open cavity with those obtained by Giannetti, Luchini and Marino [20] for the lid-driven cavity.

The parameter used for this comparison is the friction Reynolds number Re_τ, since the Reynolds number that characterize the the two flows are defined in a different manner. In particular, in the case of lid-driven cavity, the reference velocity entering the Reynolds number usually is the moving lid velocity, which is set to 1, while, in the case of the open cavity, it is the external velocity, which is also set to 1 for convenience. The reference length is, in both cases, the dimension of the cavity in the stream-wise direction that is also set to 1. Unfortunately, it is impossible to directly compare the results obtained in two cases for the same Reynolds number because the reference velocities are not the same. As previously said, the most appropriate parameter to compare these two problems seems to be Re_τ, which is a quantity linked with the shear stress and so with the derivative of the stream-wise component of the velocity vector in the direction normal to the wall.

Starting from the friction velocity u_τ, the friction Reynolds number can be written in this way:

$$Re_\tau = \sqrt{Re}\sqrt{\frac{\partial u^*}{\partial z^*}} \tag{4.1}$$

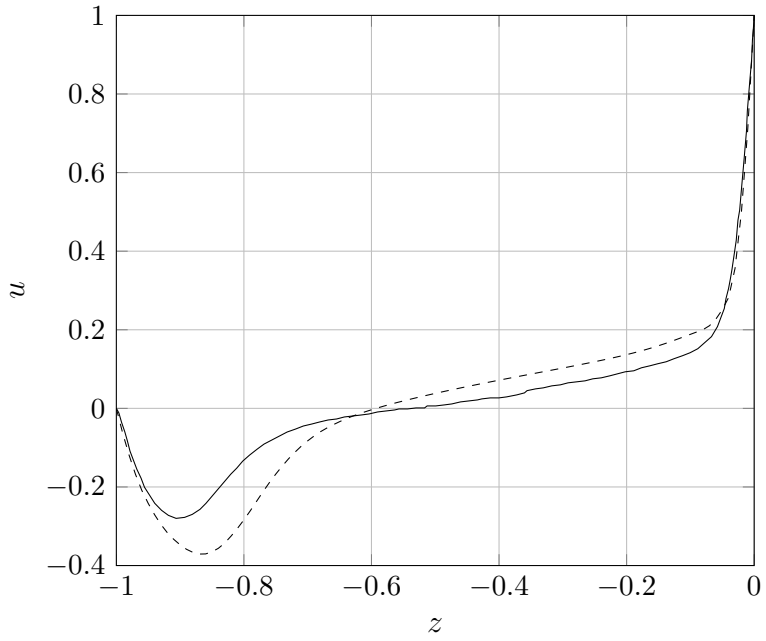

FIGURE 4.1. Compariosn between the streamwise velocity profile in the lid-driven cavity (——) for $Re = 2000$ and in the open open cavity (- - -) for $Re = 6500$.

where u^* and z^* are the dimensionless quantities obtained with the reference velocity U and the reference length L. In both the cases the derivative is calculated along the centreline of the cavity $x = 0.5$, $y = 0$ and for $-1 < z < 0$, and it is evaluated at $z = 0$. For the lid- driven cavity this point represent the centre of the wall in motion and τ_w is the effective wall shear stress, while in the case of open cavity, this quantity is related to the stress that drives the motion within the cavity.

In figure 4.1 the velocity profiles of the streamwise component of the velocity in the z direction are shown. In particular, for the lid-driven cavity, the case for $Re = 2000$, which is available in the work of Giannetti, Luchini and Marino [20] is reported, while for the open cavity the streamwise velocity profile conveniently scaled since u assumes unitary value at the interface between the cavity and the external channel is shown and, as the reader can notice, they have qualitatively the same trend. Starting from these profiles, it is first possible to calculate the derivative of the velocity in correspondence of $z = 0$, which is 19.08 for the lid-driven cavity and 5.95 for the open cavity. From these two values and from the Reynolds numbers of the two simulations, the Re_τ that characterise the two flows are 195.35 for the lid-driven cavity and 196.66 for the open cavity, which match quite well. Also the derivative

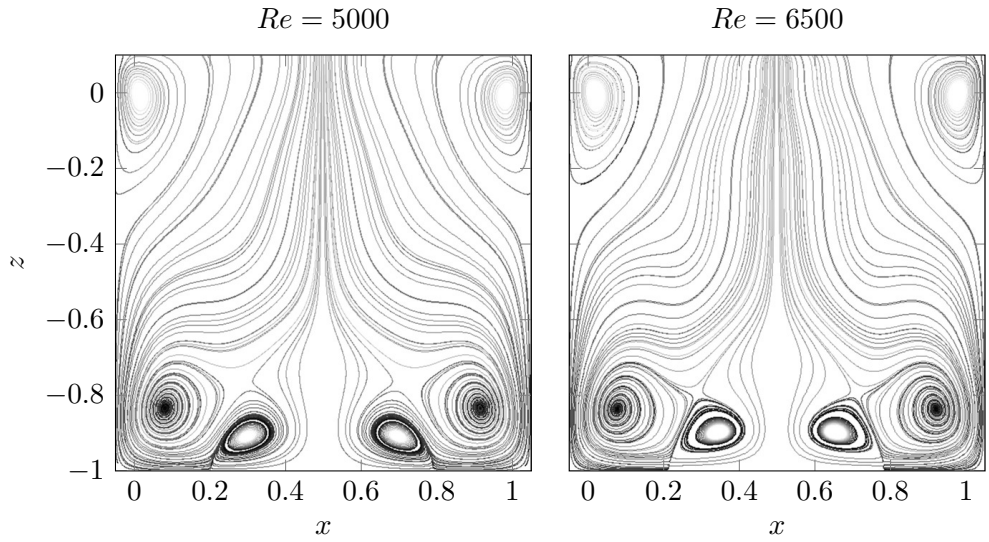

FIGURE 4.2. Three-dimensional open cavity flow with $AR = 1$: velocity streamlines in the $x = 0.5$ plane for $Re = 5000$ (left) and $Re = 6500$ (right).

of the velocity profiles at these two Reynolds numbers (do not shown) are qualitatively and quantitatively very similar with the main differences in correspondence of the lower wall of the cavity.

Since the work of Giannetti, Luchini and Marino [20] is concerned to a cuboid lid-driven cavity and in literature eigensolution computations about the three-dimensional cuboid open cavity are not present, the author will utilized these results for a validation of those obtained in this thesis.

4.2 Flow morphology

The simulations for the cavity with unitary aspect ratio are performed in a range of Reynolds number between 5000 and 7125. For this aspect ratio the counter-rotating vortices which develops in spanwise direction are observed again, but one great difference with respect to the results introduced in the previous chapter can be underlined. In fact, if for the cavity with $AR = 2$ the number of vortex pairs increase as the Reynolds number is increased, in this geometry only one pair spanwise vortices is observed for all the Reynolds numbers analysed. The justification to this behaviour can be found considering that the presence of two lateral vortices, which arise close to the cavity corners and which are caused by the no-slip and no-penetration condition imposed to the cavity walls, limits the available space for development and the expansion of the Görtler vortices. For example, the figure 4.2 shows the velocity

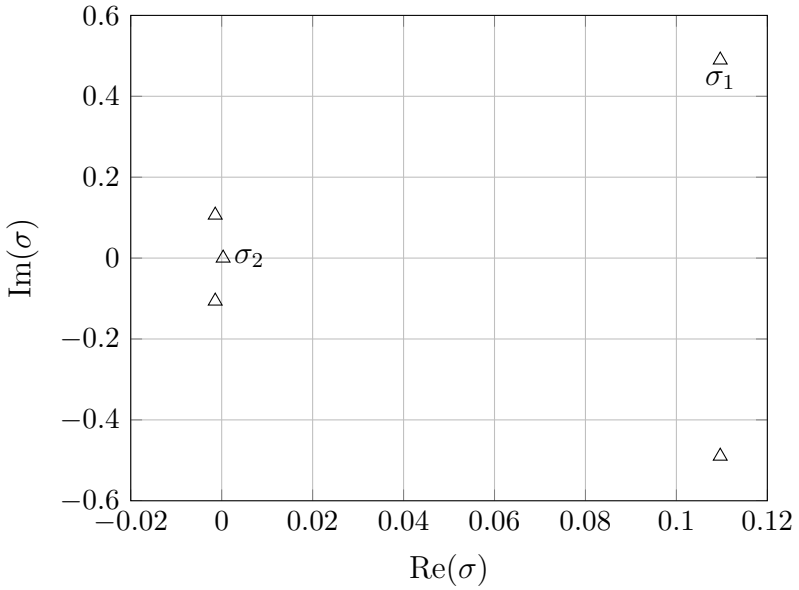

FIGURE 4.3. Three-dimensional open cavity flow with $AR = 1$: direct eigenvalues for $Re = 7000$.

streamlines in the $x = 0.5$ plane for Reynolds numbers equal to 5000 and 6500. Here it is evident that only one pair of Görtler vortices is present, while in figures 3.10 and 3.11, where the streamlines in the same plane and for the same Reynolds numbers but for $AR = 2$ were showed, the increased number of pairs of counter rotating vortices was clear.

This morphology is comparable with the results presented by Alizard, Loiseau and Robinet [1], which show the presence of Görtler vortices inside an open cavity with an infinite extension. Since the absence of lateral walls in their computation, Alizard, Loiseau and Robinet [1] have found three pairs of counter-rotating vortices. This highlights once again the importance of the later walls and of the no-slip condition imposed on these boundaries.

4.3 Stability analysis

Once the base flow has been computed, the stability simulation is started imposing a homogeneous Dirichlet condition on all the boundaries and superimposing to the steady flow a random fluctuation as initial condition. The computation of the five eigenvalues nearest to the origin of the complex plane gives the spectrum reported in figure 4.3. In particular, this spectrum is characterised by a pair of complex-conjugate and one real eigenvalue with

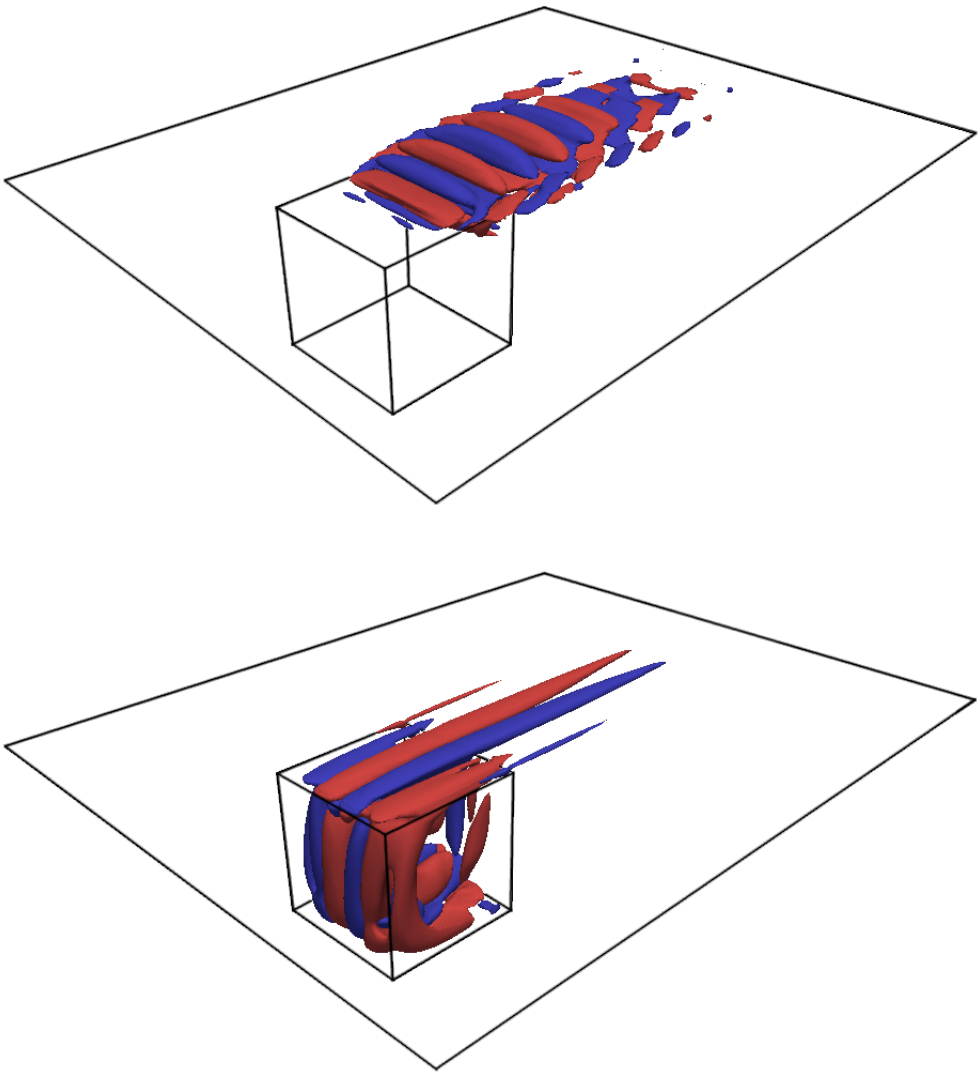

FIGURE 4.4. Three-dimensional open cavity flow with $AR = 1$: real part of direct global mode corresponding to the eigenvalue σ_1, visualised by the contour of the streamwise velocity component for $u = \pm 0.0005$ (top) and direct global mode corresponding to the real eigenvalue σ_2 visualised by the contour of the streamwise velocity component for $u = \pm 0.0003$ (down).

positive real part and by a pair of complex-conjugate eigenvalues with negative real part. This allows to conclude that in these conditions the flow is unstable and that both oscillating and steady unstable modes could be present.

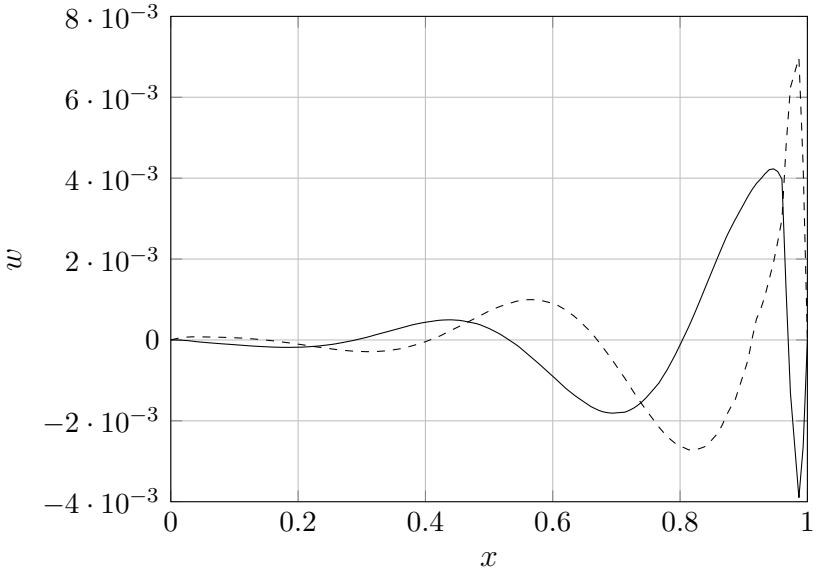

FIGURE 4.5. Three-dimensional open cavity flow with $AR = 1$: real (——) and imaginary (- - -) parts of the transverse velocity w measure at $0 <= x <= 1$, $y = 0.25$ and $z = 0$.

Now, it is useful to look at the spatial structures of the unstable modes that are visualised in figures 4.4 through the isosurfaces of their streamwise velocity component.

In the first case, the unstable mode with a non-zero imaginary part (figure 4.4) has a shape quite similar to the one obtained by Sipp and Lebedev [32] for the two-dimensional cavity. In particular, the direct eigenfunction is main localized in the shear layer at the interface between the cavity and the external flow and in the boundary layer past the cavity. It consists of vortices that move in downstream direction and, at the same time, are dumped. In figure 4.5, it is interesting to note the phase shift between the real and the imaginary parts of the vertical velocity w which is probably responsible of the activation of the downstream convection of the vortical structures. The important difference between the spectrum computed by Sipp and Lebedev [32] and the one obtained in this thesis is the frequency of the most unstable mode. The recent study by Citro, Giannetti and Brandt [11] has underlined that the intrinsic frequencies of the unsteady three-dimensional modes suffer a drastic decrease. The computed values of such 3D modes for the flow over a 2D open cavity have an order of magnitude comparable with the one of the most unstable mode computed for the three-dimensional cavity. In particular, the differences encountered with the results of Sipp and

Lebedev [32] and Citro, Giannetti and Brandt [11] can be partially justified considering the difference of the displacement thickness, which is an important parameter for the stability properties of this kind of flow. In fact, in the present computation, the boundary layer is characterized by a boundary layer displacement thickness $\delta = 0.03624$, which is about three times greater than the one studied in the aforementioned papers.

In the second case, the steady unstable mode is localised inside the cavity near the upstream and bottom cavity walls, where the effects of the centrifugal forces are most important and it shows a tail in the shear layer above the downstream wall. A useful comparison can be tried with the results reported by Alizard, Loiseau and Robinet [1] for the infinitely extended cavity. Considering a disturbance with wavenumber $\beta = 2$ they computed, for $Re = 4200$, a spectrum characterised by an unstable steady eigenvalue which they have linked to a centrifugal instability. Once again, the effect of the cavity lateral walls must be considered. In fact, the mode reported in the draft of Alizard, Loiseau and Robinet [1] and the one showed in figure 4.4 are well comparable in the centre of the cavity, but near the lateral walls the shapes do not match. Finally, the shape of this mode is comparable to the shape of the steady mode presented in the paper by Marino, Giannetti and Luchini [20] about the lid-driven cavity. As well as the mode shape, also the steady eigenvalue and the two stable complex-conjugate eigenvalues reported here are located in the complex plane in a position similar to the one of the eigenvalues computed for the lid-driven cavity.

The results presented in this thesis can not be validated by comparison with established results, since no eigenvalue computations have been performed for the three-dimensional open cavity to date. It is important to consider that just five eigenvalues nearest to the origin of the complex plane have been computed. Hence, it is possible that the eigenvalues showed in figure 4.3 correspond to modes which do not describe in detail the behaviour of the flow. However, the agreement with the results of Sipp and Lebedev [32] for the two-dimensional open cavity and of Marino, Giannetti and Luchini [20] allows the author to conclude that the computed modes could have physical sense, but further calculations with increasing polynomial order and for different Reynolds numbers will be necessary.

5 | Conclusions

This thesis work has focused on the numerical investigation of a three-dimensional, incompressible flow over an open cavity with different aspect ratios.

NEK5000, an open source CFD solver based on the spectral element method whose principal features are described in chapter 2 and in appendix A, was used to perform the computations. This solver has proved to give reliable results for the two-dimensional problems of the flow around a circular cylinder and the flow over an open cavity. In fact, both the base flow and the eigensolution computed for these two problems match well those presented in the paper of Sipp and Lebedev [32].

The results obtained for the three-dimensional open cavity are in accordance with those described in the works of Faure *et al.* [15] [16]. In particular, the most interesting result with respect to the flow morphology is the observation of longitudinal pairs of counter rotating vortices due to centrifugal forces, which develop in spanwise direction. In the case of the open cavity with $AR = 2$ the presence of these vortical structures is evident for $Re \geq 3200$, while, for $AR = 3$, the minimum Reynolds number for which they are visualized is 4000. A detailed analysis of the flow for Reynolds numbers in the range [3000, 4000] has shown that the appearance of these spanwise pairs of vortices is gradual, rather than a drastic change of the flow behaviour. Therefore, the first conclusion to be drawn is that for low Reynolds numbers, the three-dimensional open cavity flow is not subject to a centrifugal instability as is reported in the paper of Bres and Colonius [5] about an infinitely spanwise extended cavity. This is probably due to the presence of the lateral walls which break the spanwise translation invariance.

For higher Reynolds numbers, the flow shows an unsteady behaviour. In the cavity with $AR = 2$, the solution starts to oscillate for $Re \geq 6750$ and this seems to be due to a Kelvin–Helmholtz instability which develops at the interface between the slower flow inside the cavity and the faster flow outside of it. The unsteady behaviour is characterized by a periodic solution with dimensionless frequency of $St = fL/U = 0.905$, measured at $Re = 7000$.

Furthermore, it is possible to observe the formation of a Kelvin–Helmholtz vortex that develops at $x \simeq 0.75$ and interacts with the cavity trailing edge. Connected to this vortex is the presence of large-scale pressure fluctuations which propagate past the cavity.

Finally, the first results about stability for the open cavity with $AR = 1$ are presented. The five eigenvalues nearest to the origin of the complex plane have been computed for $Re = 7000$ and the resulting spectra is characterized by a pair of complex-conjugate and a real eigenvalues with positive real part. The mode shape relative to the first two unstable complex-conjugate eigenvalues is well comparable with the one presented in the paper of Sipp and Lebedev [32] for the most unstable eigenvalues, while the mode shape of the unstable steady eigenvalue is in accordance with the shape of the steady mode reported in the work of Marino, Giannetti and Luchini [20] about the three-dimensional lid-driven cavity. This permits to conclude that the stability results obtained have a physical sense, but further analyses are necessary for the validation of the results obtained in this thesis.

5.1 Future perspectives

First of all, in order to validate the stability results described in chapter 4, it is necessary to compute the eigenvalues for $Re = 7000$ with an increased order of the polynomial bases.

Second, the stability computation should be performed for different Reynolds numbers. This will allow to map the eigenvalues as a function of the Reynolds number and to estimate the critical Reynolds number. The stability for the cavities with $AR = 2$ and $AR = 3$ has to be investigated in order to interpret the results about the unsteady flow observed for the cavity with $AR = 2$ described in the section 3.3 by virtue of the computed spectra. Furthermore, the hypothesis about the gradual insurgence of pairs of counter-rotating vortices in spanwise direction without an instability will be checked.

Finally, the adjoint problem has to be solved in order to identify the *wavemaker* and to locate the region responsible of the instability, as explained in the chapter 1. In addition, the paper of Giannetti and Luchini [19] explains how the structural stability analysis results can be used to control the flow, with the principal aim of suppressing the oscillation and to prevent instability by an active or passive control. In particular, for the cavity problem, the work of Cattafesta *et al.* [8] describes various active control techniques for the flow over an open cavity

Thanks to the work done for this thesis, now the code to compute the

eigensolution for the three-dimensional flow over an open cavity with NEK5000 is well functioning and the principal aspects of the computation are reported in the appendix A. When further cpu hours will be available, the stability analysis can carried through to completion.

A | Brief NEK5000 tutorial

This appendix focuses on the files and the procedures necessary for a simulation with NEK5000. In particular, the first section is dedicated to the computation of the base flow, while the second section is concerned with the solution of the eigenvalue problem.

A.1 Base flow computation

In order to compute the base flow for the open cavity problem (in the following ocavity) with NEK5000, the files *ocavity.rea*, *ocavity.usr*, *SIZE* and *ocavity.box* are necessary.

First, the file *ocavity.box* has to be generated. This file divides the computational domain of the problem in macro-boxes such that the mesh generation and the boundary condition specification are easier. This file is built in this way:

- 1st line: name of the existing .rea file (in this case *ocavity.rea*);
- 2nd line: number of spatial dimensions;
- 3rd line: number of the simulation fields;
- 4th line: label "Box " indicating that in the next lines the parameters of the first macro-box are described;
- 5th line: number of elements in x, y and z directions.
- 6th line: value of x_{min}, x_{max} and element ratio form left to right; If the ratio is equal to 1.0 all the elements have the same size. If it is greater than 1.0 the elements are more refined near x_{max}, while, if it is less than 1.0, the elements are more refined near x_{min};
- 7th and 8th lines: similar to the 6th line but referred to the y and z directions;

- 9th line: boundary conditions on each one of the 6 faces of the macro-box. In this problem the boundary conditions are:
  - v (velocity): Dirchlet condition with a value imposed by the subroutine *userbc* in the *ocavity.usr* file;
  - W (wall): no-slip condition $\rightarrow \mathbf{u} = \mathbf{0}$;
  - O (outflow): the flow leaves the domain through this boundary $\rightarrow p = 0$;
  - SYM (symmetry);
  - "white space": this face is in common with two boxes.

  In a three-dimensional problem the user has to specify six boundary conditions for each box (one for each face). It is necessary to be careful with the white spaces because *genbox* reads 3 spaces for each condition and then looks for a comma. So, for example "v , , ,W ,SYM,O " is correctly read by the preprocessor, while "v, , ,W,SYM,O" gives an error;
- successive lines: all the other macro-boxes are defined.

The second file is the *ocavity.rea* file, which contains all the information and the simulation parameters which the user has to set for the specific problem. In particular, for the solution of the open cavity flow, the most relevant parameters to control the simulation are the following:

- DENSITY: density of the fluid. The suggested value is 1.0;
- VISCOS: here set to a negative value in order to provide the Reynolds number based on the streamwise length of the cavity (always 1.0) and the external fluid velocity. If it is set to a positive value, this parameter corresponds to the value of the kinematic viscosity of the flow;
- NSTEP: number of time steps of the simulation. To run a simulation with a fixed number of steps, it is necessary to impose the parameter FINTIME = 0.0;
- DT: value of the time step
  - if DT = 0.0: NEK5000 automatically calculates the time step at each iteration according to the stability condition;
  - if DT > 0.0: this value represents the upper limit of the simulation time step and the effective value of DT is calculated at each iteration according to the stability condition;

  - if DT $<$ 0.0: NEK5000 fixes the simulation time step to this specified value. In this case if the stability condition is violated the simulation will be stopped;

- IOTIME: number of time steps between two output files are dumped;
- DIVERGENCE: tolerance for the pressure solver;
- HELMOLTZ: tolerance for the velocity solver;
- COURANT: maximum Courant number;
- TORDER: order of the BDFk-EXTk time integration scheme. It can be alternatively set to 1, 2 or 3.

The *ocavity.usr* file contains some subroutines which allow the user to manipulate the simulation variables. For example, the subroutines *userbc* and *useric* can be used to impose the boundary and initial conditions. In this problem, both these subroutines are built such that the external file *blasius.data*, that contains the velocity Blasius profile, is read. The other important subroutine is *userchk*, which is called before the time loop for every iteration. This subroutine contains all the commands for the initialization of the variables and for their manipulation, like the calculation of the simulation residual for the convergence test.

Finally, the *SIZE* file contains all the information useful for memory allocation. The most important parameters that the user has to set are:

- LDIM: number of spatial dimensions;
- LX1/LY1/LZ1: number of points in the x, y and z direction within each element for the velocity field. This parameter determines the degree of the polynomial used in the simulation;
- LP: maximum number of processors;
- LELG: maximum number of mesh elements;
- LELV: maximum number of local elements for V-mesh.
  LELV = LELG $\geq$ int(NELGT/NP) + 1
  where NELGT $\leq$ LELG and NP $\geq$ LP.

Since these files contain a lot of parameters that can be manipulated, the best approach is to start form one of the examples that can be downloaded from the NEK5000 website and to introduce the required modifications for the problem that the user has to solve.

A.1.1 Simulation run

The first step necessary for any fluid dynamic computation based on finite elements, finite volumes or spectral elements is the generation of the mesh that discretises of the domain. In NEK5000 the mesh generation is provided by the preprocessor NEKTON with the command *genbox* and the file *ocavity.box*. From the command line the user has to enter in the working directory and type

```
$ genbox
  input file name: ocavity.box
```

This first step generates a new file called *box.rea* which contains the same parameters of the *ocavity.rea* file and all the mesh elements with the associated boundary conditions.

In the second step, the command *genmap* produces a proper processor decomposition. Starting from the *box.rea* file previously generated, this command has to be executed in this way:

```
$ genmap
  Input (.rea) file name:
  box.rea
  Input mesh tolerance (default 0.2):
  0.2
```

and gives a new binary file called *box.map* which has to be renamed as *ocavity.map*. After that, it is possible to split the information about the simulation parameters and about the mesh contained in the *box.rea* file in two different files. The first one is again the *ocavity.rea* file with all the simulation parameters, while the second one is the binary file *ocavity.re2* which contains the mesh. This splitting operation can be done with the command *reatore2* in this way:

```
$ reatore2
  Input old (source) file name:
  box
  Input new (output) file name:
  ocavity
```

Now the user is ready to built NEK5000. This step is necessary for every new simulation or when the *ocavity.usr* or the *SIZE* files are changed. To do this, it is necessary to use the script *makenek* which is located in the nek5_svn/trunk/nek directory:

```
$ ./path to makenek directory/makenek ocavity
```

It is important to verify if this script includes the correct *Fortran77* and *C* compilers installed on the working machine, the correct path of NEK5000 source, the object list of additional files to compile and the optional linking flags to some external libraries. The compilation of NEK5000 generates automatically the *ocavity.f* and *makefile* files, the *obj* folder, and the executable *nek5000*.

Finally, to run the open cavity problem with NEK5000 the user has to type the command *nekmpi* for a foreground run or *nekbmpi* for a background run (both files are in the folder nek5_svn/trunk7/tools/script) and to specify the number of processors. For example, to run the test in background with 4 processors the command is:

```
$ ./path to nekbmpi directory/nekbmpi ocavity 4
```

At the end of the simulation a series of binary files *ocavity.fld??* will be generated depending on the NSTEPS and IOSTEP parameters in the *ocavity.rea* file. For the visualization of the results, one can use alternatively two open source software: VisIt or ParaView. In both cases it is necessary to generate a metadata file called *ocavity.nek5000* which can be opened by this software. This last file is obtained by executing the command *visnek* in this way:

```
$ ./path to visnek directory/visnek ocavity
```

A.2 Eigenvalue computation

Once the base flow is computed, the user can perform the stability analysis of the obtained solution. The files and the steps necessary for the computation of the eigensolution with NEK5000 are essentially the same described in the previous two sections. In addition, three other files are needed. The first one is the *arnoldi.f* file, which interfaces NEK5000 with the arpack and parpack libraries which implement Arnoldi's method. The proper libraries for the restart have to be installed and referred to in the executable *makenek*. The second one is the *param_database.f* file, that allows to read the parameters for the eigenvalue computation, which are written in the third file *ocavity.rea.usr*. In particular, in this last file, the user can specify the number of time steps between Arnoldi calls, the maximum number of Arnoldi steps, the number of required eigenvalues, the size of the Krylov space, the arpack tolerance and if the computation has to be started from a restart point.

Looking at the files presented in the first section, the parameters in the *ocavity.rea* file that the user has to change are:

- DT: must be fixed to a value which guarantees the numerical stability of the solution. A good choice is half of the minimum time step used in the base flow computation;
- TORDER: it is better to employ a 2nd order scheme rather than a 3rd order scheme, to have a more stable time integration scheme;
- NPERT: must be set equal to -1;
- OUTPUT FIELD SPECIFICATION - COORDINATE: for the correct dump of the eigenvector files this parameter must be set true (T);
- RESTART: this parameter must set to 1 in order that NEK5000 can read the baseflow field obtained from the procedure described in the previous section. For example:

```
1 PRESOLVE/RESTART OPTIONS  *****
re7000.baseflow
```

  where *re7000.baseflow* is the last output file of the base flow computation.

In the *userchk* subroutine in the *ocavity.usr* file, it is necessary to recall the subroutines written in the *arnoldi.f* file and to change the boundary conditions imposing a homogeneous Dirichlet conditions on all the boundaries and the initial conditions by superimposing a random perturbation field on the base flow.

When the simulation is finished, the output will be the *eigenvalue.txt* file, which contains the real part of the eigenvalues in the fourth column and the imaginary part in the fifth column and the *egvocavity.fld??* files, in a number equal to the number of computed eigenvalues.

Finally, it is important to consider the possibility to use the restart files of the eigenvalues computation for a Reynolds number as the restart files for a new eigenvalues computation for a Reynolds number closed enough to the the first. This can be done changing the Reynolds number parameter and the baseflow file in the *ocavity.rea* file. In this way, the computational time for the eigenvalues calculation for different Reynolds numbers, which can be very high for three-dimensional problems, can be drastically decreased.

B | Estratto in lingua italiana

Il comportamento della corrente all'interno di una cavità è un fenomeno fluidodinamico molto importante perché rappresenta il problema modello di molte geometrie di interesse aerodinamico e fluidodinamico. Alcuni esempi sono i fori per le viti e i rivetti, le cavità tra gli alettoni o i flap e il resto dell'ala, i vani per i carrelli e i fori delle prese di pressione. In particolare, il flusso in questo tipo di dominio può essere causa di rumore, di carichi non stazionari e vibrazioni, che, a loro volta, possono generare transizione e turbolenza con un conseguente aumento di resistenza oppure, in casi peggiori, un danneggiamento e una perdita di efficienza del componente.

Nonostante la maggior parte delle applicazioni aeronautiche coinvolgano flussi a numeri di Mach transonici, l'ipotesi fatta in questa tesi è quella di flusso incomprimibile. Le ragioni principali che hanno portato a questa scelta sono due. Per prima cosa, anche se il flusso indisturbato esterno è caratterizzato da un numero di Mach relativamente alto, la velocità del flusso all'interno e nelle immediate vicinanze della cavità sarà sicuramente molto minore rispetto a quella esterna a causa della condizione di perfetta adesione a parete che rallenta la corrente vicino all'imbocco della cavità. Inoltre, è necessario considerare che diversi fenomeni che possono essere assimilati al flusso all'interno di una cavità possono essere osservati anche a numeri di Mach molto minore, per i quali l'ipotesi di incomprimibilità è valida.

In letteratura il comportamento del flusso all'interno di una cavità è un argomento largamente trattato, ma con risultati riguardanti prevalentemente la cavità bidimensionale o chiusa. A proposito della cavità tridimensionale i risultati sono quasi esclusivamente sperimentali, come quelli proposti da Faure *et al.* [15] e [16], riguardanti la morfologia del flusso in una cavità caratterizzata da diversi allungamenti. Risultati riguardanti la stabilità sono invece presenti nell'articolo di Bres e Colonius [5] nel caso di cavità infinitamente estesa in direzione laterale e nell'articolo di Sipp e Lebedev [32] nel caso di cavità bidimensionale.

Modello matematico

Il comportamento del flusso all'interno della cavità è descritto dalle equazioni di Navier–Stokes incomprimibili

$$\begin{cases} \dfrac{\partial \mathbf{u}}{\partial t} + (\mathbf{u} \cdot \nabla)\mathbf{u} - \dfrac{1}{Re}\nabla^2 \mathbf{u} + \nabla p = \mathbf{0} \\ \nabla \cdot \mathbf{u} = 0, \end{cases} \tag{B.1}$$

in cui il numero di Reynolds, definito come

$$Re = \frac{L\, U_\infty}{\nu}, \tag{B.2}$$

è il parametro adimensionale da cui dipende la risposta del sistema fluidodinamico. Per la soluzione delle equazioni di Navier–Stokes opportune condizioni al contorno e iniziali dovranno essere imposte.

Il sistema non lineare B.1 presenta diverse soluzioni di equilibrio le cui proprietà dovranno essere studiate separatamente. Questo studio può essere affrontato con un approccio globale ottenuto grazie alla linearizzazione delle equazioni nell'intorno del punto di equilibrio e all'applicazione del metodo di Lyapounov indiretto, per il quale è necessario il calcolo degli autovalori del sistema linearizzato nel punto di equilibrio.

Uno strumento necessario per l'analisi di stabilità globale è l'operatore aggiunto, la cui descrizione dettagliata può essere trovata nell'articolo di Luchini e Bottaro [23]. L'applicazione dell'operatore aggiunto alle equazioni di Navier–Stokes permette di eseguire l'analisi di sensitività strutturale e, in particolare, di calcolare il parametro di sensitività strutturale

$$s(x,y,z) = \frac{\|\hat{\mathbf{v}}^*(x,y,z)\|\|\hat{\mathbf{u}}(x,y,z)\|}{\left|\int_\Omega \hat{\mathbf{v}}^* \cdot \hat{\mathbf{u}}\right|}. \tag{B.3}$$

dove $\hat{\mathbf{u}}$ e $\hat{\mathbf{v}}^*$ sono le autofunzioni diretta e aggiunta associate all'autovalore con parte reale maggiore e, quindi, meno stabile. Questo risultato permette di valutare l'effetto di una perturbazione del sistema sulla risposta dinamica del sistema stesso.

Modello numerico

Per le simulazioni numeriche del flusso all'interno della cavità e per il calcolo degli autovalori è stato utilizzato il software open source NEK5000, un solutore fluidodinamico sviluppato da Paul Fisher e dai suoi collaboratori al Mathematics and Computer Science Division of Argonne National Laboratory.

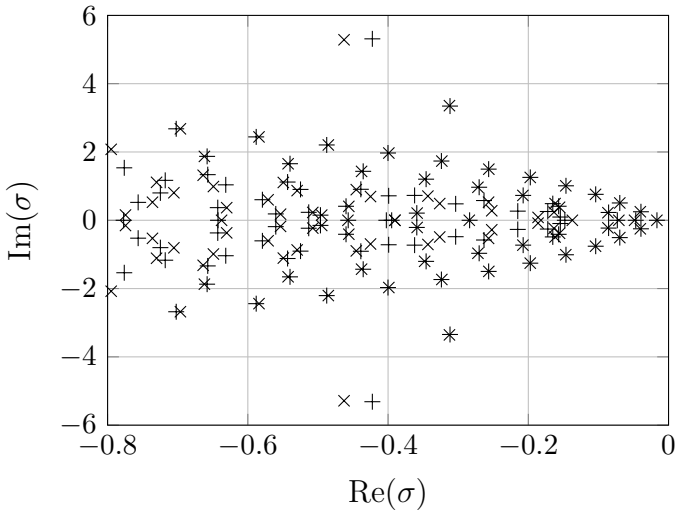

FIGURA B.1. Cavità 2D: autovalori diretti (+) e aggiunti (×) a $Re = 4135$.

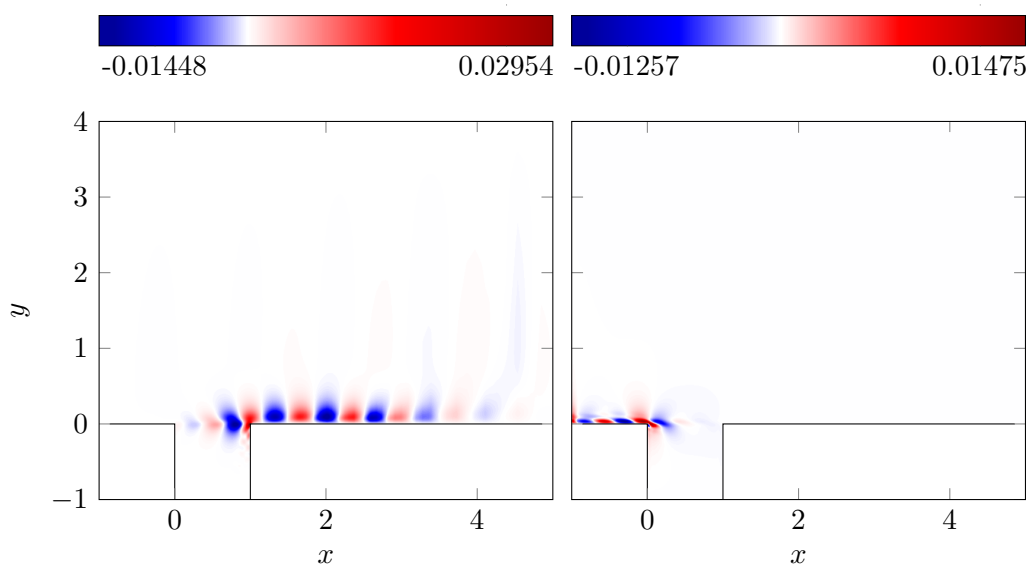

FIGURA B.2. Cavità 2D: parte reale dell'autovettore diretto (sinistra) e aggiunto (destra) rappresentate attraverso la componente longitudinale della velocità relative all'autovalore più instabile per il flusso a $Re = 4135$.

In NEK5000 la discretizzazione spaziale è basata sul metodo ad elementi spettrali. In particolare, per l'approssimazione del campo di velocità vengono usati i punti di integrazione di Gauss-Legendre-Lobatto mentre per il campo di pressione vengono usati i punti di Gauss-Legendre. Questa scelta, associata all'utilizzo di polinomi di grado N per l'approssimazione della velocità e di

AR	dimensione dominio	elementi	celle	punti
1	[-1.0, 5.0] × [-4.0, 4.0] × [-1.0, 4.0]	68320	8540000	14757120
2	[-1.0, 5.0] × [-4.5, 4.5] × [-1.0, 4.0]	99520	12440000	21496320
3	[-1.0, 5.0] × [-5.0, 5.0] × [-1.0, 4.0]	130720	16340000	28235520

TABELLA B.1. Dimensione del dominio e numero di elementi, celle e punti per i diversi apstect ratios analizzati.

grado $N-2$ per l'approssimazione della pressione, consente di rispettare la condizione *inf-sup* e, quindi, di evitare modi spuri di pressione nella soluzione.

La discretizzazione temporale è, invece, basata sullo schema BDFk-EXTk, dove k indica l'ordine di integrazione temporale dello schema numerico. L'estrapolazione di ordine k permette di evitare il calcolo della soluzione di un sistema non lineare ad ogni passo temporale, che, nel caso di utilizzo del solo schema BDF, sarebbe presente a causa del termine non lineare delle equazioni di Navier–Stokes.

Successivamente, l'applicazione della discretizzazione temporale alle equazioni di Navier–Stokes avviene attraverso una tecnica di time splitting spiegata dettagliatamente nell'articolo di Fisher [17].

Il calcolo delle autosoluzioni è stato eseguito grazie all'interfaccia di NEK5000 con le librerie arpack e parpack. I risultati per la cavità bidimensionale sono mostrati nelle figure B.1 e B.2 e sono in accordo con quelli presentati nel paper di Sipp e Lebedev [32].

Morfologia del flusso

Il flusso all'interno della cavità è stato studiato per tre diversi allungamenti

$$AR = \frac{W}{L} = \frac{\text{dimensione laterale}}{\text{dimensione longitudinale}} \tag{B.4}$$

e le caratteristiche della mesh nei tre casi sono riportate in tabella B.1. Al variare del numero di Reynolds sono state osservate diverse morfologie del flusso nel piano di simmetria della cavità. In tutti i casi è possibile notare la presenza di un vortice, detto vortice principale, che occupa la parte centrale della cavità e che è caratterizzato da una velocità maggiore rispetto a quella delle altre strutture vorticose secondarie presenti. In particolare, queste ultime sono due vortici contro-rotanti che si sviluppano negli angoli sul fondo della cavità e un vortice contro-rotante che, per numeri di Reynolds sufficientemente alti, si sviluppa in corrispondenza del bordo d'attacco della cavità.

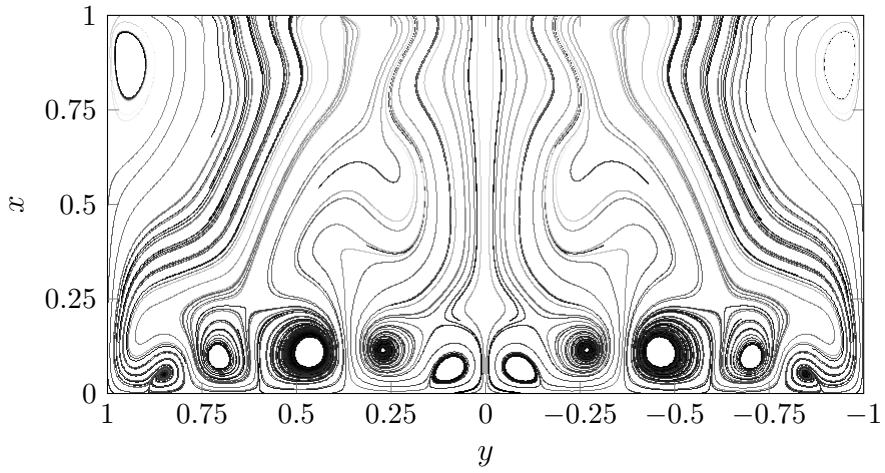

FIGURA B.3. Cavità 3D con $AR = 2$: linee di corrente nel piano $x = 0.5$ per il flusso a $Re = 6500$.

Nel caso di cavità con $AR = 2$, è interessante notare che per $Re \geq 3200$ diverse configurazioni di vortici secondari possono essere osservate sui piani visualizzati al variare della coordinata y. Ciò è collegabile al fatto che per $Re \geq 3200$ il flusso è caratterizzato da una serie di vortici contro-rotanti che si sviluppano in direzione laterale e che occupano tutta la cavità (figure B.3 per il flusso a $Re = 6500$). Questi vortici possono essere classificati come vortici di Görtler e sono causati dall'effetto delle forze centrifughe che si sviluppano vicino alle pareti della cavità a causa della forte diminuzione della velocità dovuta alla condizione di perfetta adesione. Un'analisi dettagliata del flusso nel range di numeri di Reynolds tra 2000 e 4000 mostra che la formazione di questi vortici è graduale, come mostrato in figura B.4. Questo suggerisce che il flusso non soffra di un'instabilità di tipo pitchfork come descritto nell'articolo di Bres e Colonius [5] sulla cavità di apertura infinita, ma, al contrario, che la soluzione presenti una condizione di pitchfork "imperfetta". La spiegazione di questo fenomeno può essere data considerando che le pareti laterali che delimitano la cavità in direzione y rompono la simmetria traslazionale del dominio. Inoltre, all'aumentare del numero di Reynolds, il numero di vortici in direzione laterale aumenta. Infatti, per $Re = 5000$, si osservano quattro coppie di vortici contro-rotanti, mentre per $Re = 6500$ se ne osservano cinque. Un aumento del numero di vortici si ha anche incrementando l'allungamento, in quanto, per $AR = 3$, si ha la presenza di sei coppie di vortici contro-rotanti a $Re = 6250$.

Nel caso di cavità con $AR = 2$ la soluzione diventa instazionaria per $Re \simeq 6750$. In queste condizioni il flusso è caratterizzato da un'instabilità

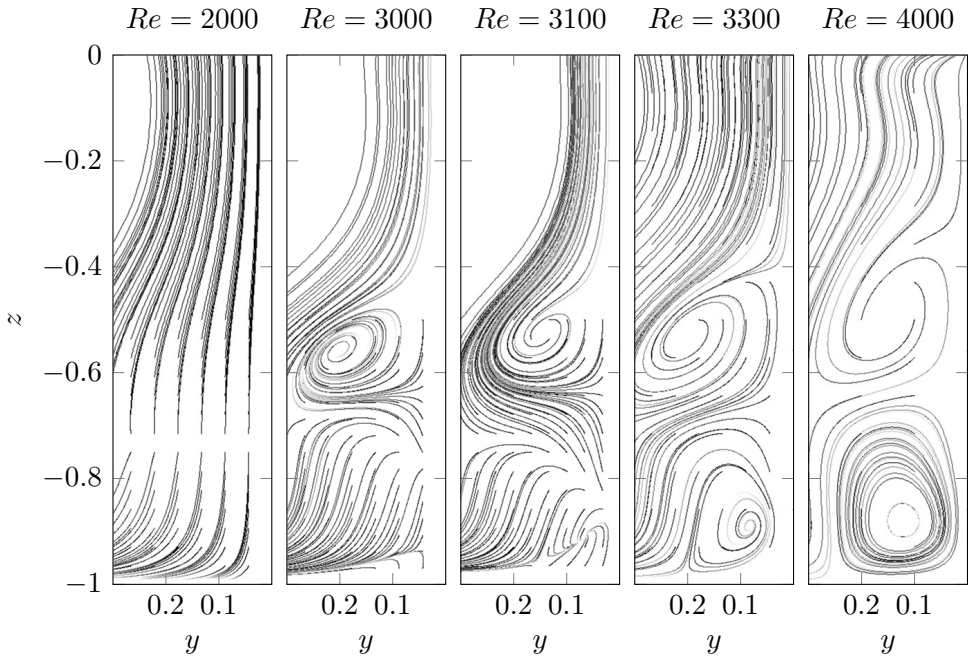

FIGURA B.4. Cavità 3D con $AR = 2$: linee di corrente nel piano $x = 0.51$ per cinque diversi numeri di Reynolds.

instazionaria dovuta a un meccanismo di Kelvin-Helmholtz che interessa lo strato di scorrimento viscoso presente tra il flusso più lento all'interno della cavità e il flusso più veloce all'esterno. A seguito di questa instabilità vi è la formazione di un vortice di Kelvin-Helmholtz che si forma periodicamente intorno a $x = 0.75$ e che interagisce con il bordo di uscita della cavità. La conseguenza principale di questo fenomeno è la formazione di zone di sovrapressione e depressione a valle della cavità.

Analisi di stabilità

Per la cavità con $AR = 1$, sono stati ottenuti dei primi risultati di stabilità grazie al calcolo dello spettro e delle autosoluzioni per il flusso a $Re = 7000$. Questi risultati sono sicuramente da considerare preliminari e da verificare con nuovi calcoli eseguiti incrementando il grado dei polinomi di approssimazione e variando il numero di Reynolds. Quest'ultima analisi permetterà anche di ottenere una mappa degli autovalori nel piano complesso e di poter determinare il numero di Reynolds critico. Inoltre, il calcolo delle autosoluzioni aggiunte consentirà di eseguire l'analisi di stabilità strutturale e di determinare il *wavemaker*, ovvero la regione del flusso responsabile dell'instabilità, come descritto nell'articolo di Giannetti e Luchini [19].

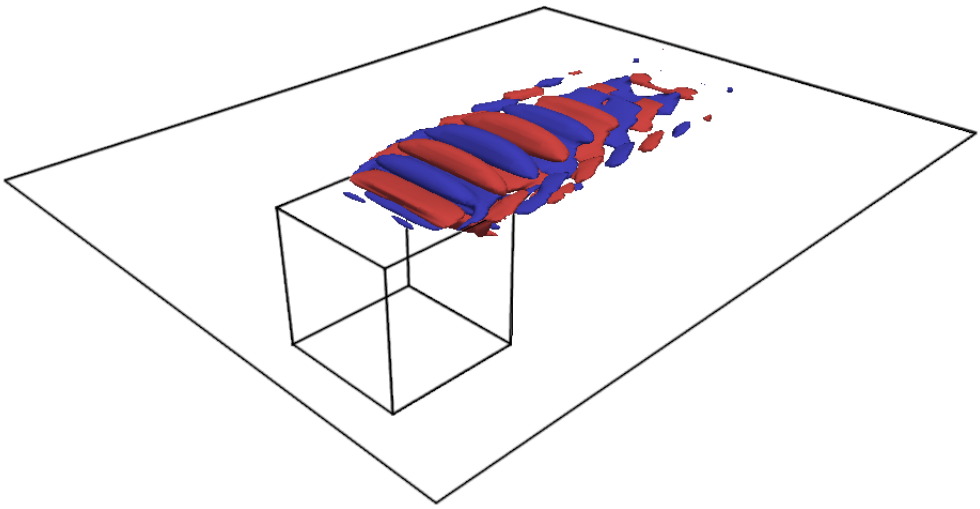

FIGURA B.5. Cavità 3D con $AR = 1$: isosuperfici della parte reale del modo diretto instabile e non stazionario visualizzato attraverso la componente longitudinale della velocità per $u = \pm 0.0005$.

Lo spettro ottenuto calcolando i cinque autovalori più vicini all'origine del piano complesso è caratterizzato da due autovalori complessi e coniugati e da un autovalore reale con parte reale positiva. In queste condizioni il flusso è, quindi, instabile.

La forma del modo relativo all'autovalore instabile (figura B.5) può essere ben confrontata con i risultati presentati nell'articolo di Sipp e Lebedev [32] per la cavità bidimensionale. L'autosoluzione è prevalentemente localizzata in corrispondenza dello strato di scorrimento viscoso all'interfaccia tra il flusso all'interno e all'esterno della cavità e può essere interpretata come vortici che si muovono e, contemporaneamente, si smorzano in direzione downstream.

Come detto prima, i risultati presentati in questa tesi sono preliminari e una verifica è sicuramente necessaria. In ogni caso, il confronto con altri problemi simili presenti in letteratura permette di concludere che le autosoluzioni calcolate sono fisicamente plausibili.

Bibliography

[1] Alizard, F., Loiseau, J. C., and Robinet, J. C. Bifurcations for an incompressible flow passing over and open-cavity. In *XXIII ICTAM, Beijing, China.*

[2] Barbagallo, A., Sipp, D., and Schmid, P. J. Closed-loop control of an open cavity flow using reduced-order models. *Journal of Fluid Mechanics 641* (2009), 1–50.

[3] Basley, J., et al. Experimental investigation of global structures in an incompressible cavity flow using time-resolved piv. *Experiments in Fluids 50* (2011), 905–918.

[4] Blair Perot, J. An analysis of the fractional step method. *Journal of Computational Physics 108* (1995), 51–58.

[5] Bres, G. A., and Colonius, T. Three-dimensional instabilities in compressible flow over open cavities. *Journal of Fluid Mechanics 599* (2008), 309–339.

[6] Cain, A. B., et al. Optimizing control of open bay acustics. *AIAA paper 1928* (2000).

[7] Canuto, C., Hussaini, M. Y., and Quarteroni, A. *Spectral methods: evolution to complex geometries and applications to fluid dynamics.* Springer, 2007.

[8] Cattafesta, L., et al. Rewiev of active control of flow-induced cavity resonance. *AIAA paper 3567* (2003).

[9] Chatellier, L., Laumonier, J., and Gervais, Y. Theoretical and experimental investigations of low mach number turbulent cavity flows. *Experiments in Fluids 36* (2004), 728–740.

[10] Chomaz, J. Global instabilities in spatially developping flows: non-normality and non linearity. *Annu. Rev. Fluid Mech. 37* (2005), 357–392.

[11] Citro, V., Giannetti, F., and Brandt, L. Three-dimensional instability and sensitivity of the flow over an open cavity. *Under consideration for publication in Journal of Fluid Mechanics.*

[12] Colonius, T. An overview of simulation, modeling, and active control of flow/acustic resonance in open cavities. *AIAA J. Paper 2001-0076* (2001).

[13] Couzy, A. *Spectra element discretization of the unsteady Navier-Stokes equations and its iterative solutions on parallel computer.* PhD thesis, Ećole polytechnique fed́eŕale de Lausanne, 1995.

[14] Estep, D. J. A short course on duality, adjoint operators, green's functions, and a posteriori error analysis, 2004.

[15] Faure, T. M., Adrianos, P., Lusseyran, F., and Pastur, L. Visualizations of the flow inside an open cavity at medium range reynolds numbers. *Experiment in Fluids 42* (2007), 169–184.

[16] Faure, T. M., Pastur, L., et al. Three-dimensional centrifugal instabilities development inside a parallelepipedic open cavity of various shape. *Experiment in Fluids 47* (2009), 395–410.

[17] Fischer, P. F. An overlapping schwarz method for spectral element solution of the incompressible navier-stokes equations. *Journal of Computational Physics 113* (1997), 84–101.

[18] Gharib, M., and Roshko, A. The effect of flow oscillations on cavity drag. *Journal of Fluid Mechanics 177* (1987), 501–530.

[19] Giannetti, F., and Luchini, P. Structural sensitivity of the first instability of the cylinder wake. *Journal of Fluid Mechanics 581* (2007), 167–197.

[20] Giannetti, F., Luchini, P., and L., M. Linear stability analysis of three-dimensional lid-driven cavity flow.

[21] Ince, E. L. *Ordinary differential equations.* Dover, 1926.

[22] Knisely, C., and Rockwell, D. Self-sustained low frequency components in an impinging shear layer. *Journal of Fluid Mechanics 116* (1982), 157–186.

[23] Luchini, P., and Bottaro, A. Adjoint equations in stability analysis, 2014.

[24] Marquet, O., Sipp, D., and Jacquin, L. Sensitivity analysis and passive control of cylinder flow. *Journal of Fluid Mechanics 615* (2008), 221–252.

[25] Penza, A. Linear stability of 2d incompressible flows using trilinos. Master's thesis, Politecnico di Milano, 2011.

[26] Quartapelle, L., and Auteri, F. *Fluidodinamica incomprimibile.* CEA, 2013.

[27] Quarteroni, A. *Modellistica numerica per problemi differenziali.* Springer, 2008.

[28] Rossiter, J. E. *Wind-tunnel experiments on the flow over rectangular cavities at subsonic and transonic speeds.* HM Stationery Office, 1964.

[29] Rowley, C. W., Colonius, T., and Basu, A. On self-sustained oscillations in two-dimensional compressible flow over rectangular cavities. *Journal of Fluid Mechanics 455* (2002), 315–346.

[30] Shieh, C. M., and Morris, P. J. Parallel numerical simulation of subsonic cavity noise. *AIAA paper 1981* (1999).

[31] Sipp, D., and Jacquin, L. Three-dimensional centrifugal-type instabilities of two-dimensional flows in rotating systems. *Physics of Fluids 12* (2000), 1740–1748.

[32] Sipp, D., and Lebedev, A. Global stability of base and mean flows: a general approach and its applications to cylinder and open cavity flows. *Journal of Fluid Mechanics 593* (2007), 333–358.

[33] Tannehil, J. C., Anderson, D. A., and Pletcher, R. H. *Computational Fluid Mechanics and Heat Transfer.* Taylor and Francis, 1997.

[34] Yamouni, S., Sipp, D., and Jacquin, L. Interaction between feedback aeroacustic and acustic resonance mechanisms ina a cavity flow: a global stability analysis. *Journal of Fluid Mechanics 717* (2013), 134–165.

[35] Zhang, K., and Naguib, A. M. Effect of finite cavity width on flow oscillation in a low-mach-number cavity flow. *Experiments in Fluids 51* (2011), 1209–1229.